THE INFLUENCE OF CHEMICAL PRE-TREATMENT ON PARTICLE
FRACTURE PATTERN AND MINERAL LIBERATION

A THESIS SUBMITTED TO
THE GRADUATE SCHOOL OF NATURAL AND APPLIED SCIENCES
OF
MIDDLE EAST TECHNICAL UNIVERSITY

BY
MAHMUT CAMALAN

IN PARTIAL FULFILLMENT OF THE REQUIREMENTS
FOR
THE DEGREE OF DOCTOR OF PHILOSOPHY
IN
MINING ENGINEERING

MAY 2018

THE INFLUENCE OF CHEMICAL PRE-TREATMENT ON PARTICLE FRACTURE PATTERN AND MINERAL LIBERATION

submitted by **MAHMUT CAMALAN** in partial fulfillment of the requirements for the degree of **Doctor of Philosophy in Mining Engineering Department, Middle East Technical University** by,

Prof.Dr. Halil Kalıpçılar
Dean, Graduate School of **Natural and Applied Sciences**   _____

Prof.Dr. Celal Karpuz
Head of Department, **Mining Engineering**   _____

Prof.Dr. Çetin Hoşten
Supervisor, **Mining Engineering Dept., METU**   _____

Examining Committee Members:

Prof.Dr. Ümit Atalay
Mining Engineering Dept., METU   _____

Prof.Dr. Çetin Hoşten
Mining Engineering Dept., METU   _____

Prof.Dr. N. Emre Altun
Mining Engineering Dept., METU   _____

Assoc.Prof.Dr. İlkay B. Çelik
Mining Engineering Dept., Hacettepe University   _____

Asst.Prof.Dr. N. Metin Can
Mining Engineering Dept., Hacettepe University   _____

              Date: **24.05.2018**

I hereby declare that all information in this document has been obtained and presented in accordance with academic rules and ethical conduct. I also declare that, as required by these rules and conduct, I have fully cited and referenced all material and results that are not original to this work.

Name, Last name: Mahmut Camalan

Signature:

ABSTRACT

**THE INFLUENCE OF CHEMICAL PRE-TREATMENT ON PARTICLE
FRACTURE PATTERN AND MINERAL LIBERATION**

Camalan, Mahmut

Ph.D., Department of Mining Engineering

Supervisor: Prof.Dr. Çetin Hoşten

May 2018, 137 pages

The conventional approach in mineral beneficiation is to increase ore fineness for achieving sufficient degrees of mineral liberation. However, achieving finer products requires higher grinding energies, and finer products generate problem in slurry flow at further processing steps. Then, the emphasis should be given to foster breakage along grain-boundaries between minerals, so that sufficient liberation can be achieved without excess breakage. The purpose of this study is to assess if the aqueous species can make surface complexes at the grain boundaries to promote grain-boundary fracturing, and consequently chromite liberation. For this purpose, chromite ore samples were treated under water, dilute surfactant and electrolyte solutions at varying pH and temperature. The treated samples were broken in drop-weight tester, and then the liberation spectra and mass distribution of the resultant progenies were evaluated with the ones of untreated feed. Besides, some microscopic and spectroscopic tools were used to find evidence for structural changes at the grain boundaries in the case of improved liberation. Results show that hydrolysis of silicates tends to improve grain-boundary fracturing since it preferentially dissolves Si-layers which are located near to or at the grain-boundary regions. However, protonation tends to remove Mg-layers in silicates and hinder grain-boundary fracturing since Mg-layers are accumulated at

the bulk texture. Aqueous salt and surfactant species enhance grain-boundary fracturing, and consequently chromite liberation if they form surface complexes and dissolve Al-layers at the grain boundaries. Grain-boundary fracturing yields exposed chromite surfaces and enriched chromite content in coarser progeny classes.

Keywords: Mineral Liberation Spectrum, Grain-Boundary Weakening, Protonation, Hydrolysis, Surface Complexes

ÖZ

KİMYASAL ÖN İŞLEMİN TANELERİN KIRILMA ŞEKLİ VE MİNERAL SERBESTLEŞMESİNE ETKİSİ

Camalan, Mahmut

Doktora, Maden Mühendisliği Bölümü

Tez Yöneticisi : Prof.Dr. Çetin Hoşten

Mayıs 2018, 137 sayfa

Cevher hazırlamadaki konvansiyonel yöntem cevherin öğütme inceliğini arttırarak mineral serbestleşme derecesini yeterli derecelere ulaştırmaktır. Ancak, cevheri ince boyutlara ufalama işlemi hem yüksek enerji maliyetine, hem de zenginleştirme devrelerindeki şlam akışkanlığında problemlere sebep olmaktadır. Dolayısıyla, minerallerin granül sınırlarından kolaylıkla kırılabileceği, bu sayede serbestleşmenin fazla öğütme yapmadan sağlanabileceği yöntemler geliştirilmesi önem kazanmaktadır. Bu çalışmanın amacı, sulu kimyasal türlerin granül sınırlarında mineral yüzeyleri ile oluşturduğu yapıların granül sınırlarının çatlamasına yardımcı olup olmadığını, bunun kromit serbestleşmesini arttırıp arttırmadığını tespit etmektir. Bu kapsamda kromit cevheri su, seyreltik yüzey-aktif kimyasal ve elektrolit çözeltilerinde farklı pH ve sıcaklıkta işlenmiştir. İşleme tabi tutulmuş numuneler tek tane kırma yöntemiyle kırılmış, oluşan ürünlerin kütlece dağılımı ve serbestleşme spektrumu, işleme tabi tutulmamış numunenin kırılma tane boyu dağılımı ve serbestleşme spektrumu ile birlikte değerlendirilmiştir. Ayrıca bazı mikroskobik ve spektroskopi yöntemleri kullanılarak serbestleşmeyi arttıran işleme koşullarının granül sınırlarını zayıflatıp zayıflatmadığı tespit edilmiştir. Sonuçlar, silikatların hidrolize olmasının granül sınırlarına yakın Si katmanlarını çözeceğini ve bunun da granül sınırları arasındaki

çatlamayı kolaylaştıracağını göstermektedir. Silikat minerallerinin H^+ iyonları ile yaptığı yapılar mineralin toplu dokusundaki Mg katmanlarını çözeceği için granül sınırlarındaki çatlamayı engellenmektedir. Sudaki tuz ve yüzey-etkin türleri ise granül sınırlarına bağlanmaları ve oradaki Al tabakalarını çözmeleri halinde granül sınırlarındaki çatlamayı ve buna bağlı olarak kromit serbestleşmesini arttırmaktadır. Granül sınırlarındaki çatlamalar, kırılmış iri tanelerde kromit granüllerinin açığa çıkmasına ve kromit miktarının artmasına yol açmaktadır.

Anahtar Kelimeler: Mineral Serbestleşme Spektrumu, Granül-Sınırı Zayıflaması, Protonasyon, Hidroliz, Yüzey Kompleksleri

To Ece,

ACKNOWLEDGMENTS

TABLE OF CONTENTS

LIST OF TABLES

LIST OF FIGURES

FIGURES

xix

CHAPTER 1

INTRODUCTION

1.1. General

The increasing metal demand in the world requires increasing metal ore production. This is to be achieved by physical and physicochemical separation methods as long as metallic minerals can be liberated from waste (gangue) minerals physically by means of comminution. However, finer products require higher grinding energies because of the particulate nature and mechanical inefficiency of the ball mill (Veasey and Wills, 1991). Besides, since water is used for the subsequent handling and enrichment process of ground particles, finer products will generate hydrodynamic problems in pulp flow. Thus, research was directed to alter physical structure or chemical composition of minerals such that the minerals can be broken or fractured from their grain boundaries, i.e., intergranular (D. W. Fuerstenau, 1995) or phase-boundary breakage (Mariano et al., 2016). This would eventually cause minerals to be liberated at coarser progenies (Andres et al., 2001; Kingman et al., 2004; Parker et al., 2015; Scott et al., 2008; Shi et al., 2014; Wang et al., 2012), avoiding the requirement for excess breakage. Some novel techniques to serve for this purpose would be the utilization of radiative energy forms such as microwave (Ali and Bradshaw, 2011; Kingman et al., 2004; Scott et al., 2008) and high-voltage electric pulses (Andres et al., 1999) to stress and fracture grain-boundaries. However, their industrial applications are rather scarce, and their energy requirement might be large, making them infeasible for industrial applications (Andres, 2010; Kingman et al., 2000).

One alternative promising way to achieve intergranular breakage would be to alter chemical composition of ore samples with grinding aids (or additives) in the size-reduction equipment. Although no emphasis has been given to delineate the effect of

grinding aids on mineral liberation, it was well proven that chemical species inside dilute salt or surfactant solutions might affect the chemistry of silicate minerals by forming surface complexes (Stumm, 1995), changing their mechanical properties (i.e. strength) and breakage patterns under stress (El-Shall, 1980; Haecker, 1984; Lin and Mitzmager, 1968; Peck, 1982; Westwood and Goldheim, 1969). There are some complementary studies showing that certain chemical additives (either in liquid or gas phase) in mills may induce fine grinding by improving flow behavior of the mass (Choi et al., 2010, 2009; Hasegawa et al., 2001; Katzer et al., 1981; Klimpel and Austin, 1982; R.R. Klimpel and Manfroy, 1978; Locher and Von Seebach, 1972; Sacks and Tseng, 1983; Somasundaran, 1978; Von Seebach, 1969; Y. Wang et al., 2000; Zheng, 1997). However, the effect of chemical aids on breakage pattern has been ignored assuming that chemical species could only affect particle fracture as long as it could be adsorbed at the ongoing crack tip (Fuerstenau, 1995; Klimpel and Manfroy, 1978; Locher and Von Seebach, 1972). This is a weak assumption considering that chemical species only adsorb to the particle surface in a way similar to stress-corrosion cracking (El-Shall and Somasundaran, 1984a). It is, in fact, possible that chemical species could be adsorbed to the solid surface from inherent defects as pores and cracks. Besides, even if stress-corrosion cracking is evident for ore fracture, the chemical additives may still be absorbed too fast in gas phase due to the high vapor pressure at propagating cracks which are capillary in nature (Somasundaran and Lin, 1972).

1.2. Objective and Scope of the Thesis

The objective of this thesis is to search for the possibility for certain pre-treatment conditions with dilute solutions of certain chemical aids that could alter and weaken the grain boundaries in chromite ore so that the liberation of chromite mineral could be increased at relatively coarser particle sizes.

For the scope of this study, chromite ore in the size fraction of -9.53+6.35 mm was treated in some solutions with different pH and at different temperatures. The treatment liquids were (i) distilled water, (ii) dilute solutions of certain chloride, sulfate, nitrate and phosphate salts, and also (iii) dilute solutions of certain surfactants. After treatment, all samples were broken in a drop-weight tester one by one at a constant-specific energy, and their progeny classes were analyzed under microscope to estimate their area-based liberation spectra. The obtained spectra were then evaluated to assess impact of chemical aids on mineral liberation. Some of the treatment conditions which induced better liberation spectra were replicated, and the resultant progeny fractions were analyzed under XRF to find a correlation between chromite liberation and Cr_2O_3 (or equivalently chromite) content (%) in the coarser progeny classes.

Certain treatments which induced better liberation spectra were repeated and the samples after these treatments were analyzed under Scanning Electron Microscopy (SEM), whereas the treatment liquids were analyzed under Inductively Coupled Plasma Mass Spectrometry (ICP-MS). These experiments were mainly performed to (i) validate textural or compositional changes at the grain-boundaries in the case of improved liberation, and (ii) to estimate the possible reaction mechanisms during treatment which induced better liberation.

CHAPTER 2

LITERATURE REVIEW

2.1. Effect of Chemical Environment on the Physical and Mechanical Properties of Minerals and Materials

The basis for the use of chemical additives on minerals came from a series of studies in order to promote drilling in ore bodies by changing the chemical environment (Rehbinder, 1931, 1928; Rehbinder and Kalinkovaskaya, 1932). It had been claimed that work required to form new crack surfaces in a brittle material can be reduced if the chemical species are adsorbed to the surface and reduce the surface free energy of the material. On the other hand, such embrittlement was also attributed to the adsorption-induced changes on the dislocation mobility of solid surfaces, i.e. their crystal structure (Westwood and Goldheim, 1969). There are supporting evidences to show that brittle failure can be promoted with chemical species due to adsorption-induced decrease in surface energy (Hammond and Ravitz, 1963; Parks, 1984) or change in the crystal structure of solid materials (Alley, 1999). Furthermore, Peck (1982) directly measured fracture energies of quartzite rock under stressing in water or various aqueous solutions and concluded that hydrolysis of quartzite reduced the fracture energies of rock samples.

Later, it was shown that certain chemical environments could change the mechanical properties and grinding behavior of minerals (El-Shall, 1980; El-Shall and Somasundaran, 1984a; Haecker, 1984; Hammond and Ravitz, 1963; Orowan, 1949; Peck, 1982). These studies were prepared to simulate stress-corrosion cracking (El-Shall and Somasundaran, 1984b) where the samples were mechanically stressed under chemical conditions so that chemical aids were expected to adsorb to and affect the ongoing crack tip during loading. Regarding this, El-Shall (1980) made a

comprehensive research on the effect of various chemical environment- involving dilute solutions of salts, dispersants and surfactants - on grindability, fluidity, flocculation of quartz in ball mill, and solely product fineness (termed as primary breakage behavior) in drop-weight tester. His findings on the primary breakage behavior which are significant to this thesis can be reviewed below:

-Using dilute amine solution at alkaline conditions improved primary breakage under drop weight (Figure 2.1a) and reduced its compressive strength (Figure 2.1b) instead of using same solution at acidic and slightly-acidic conditions. The reason why alkaline amine solution improved breakage pattern was attributed to the formation of iono-molecular complexes; however, no spectroscopic analyses were provided to validate the presence of such complexes.

- Using $AlCl_3$ and $CaCl_2$ solutions improved primary breakage at highly acidic and alkaline conditions (Figure 2.2), respectively, rather than using the same solutions at different pH values. The reasons for improved breakage were attributed to the preferential adsorption of Al and Ca hydroxides rather than positively-charged ferric hydroxide in acidic and alkaline pH, respectively. Nonetheless, given the aqueous speciation diagram of Al^{3+} (Figure 2.3) by El-Shall (1980), adsorption of Al hydroxides is more likely in slightly-acidic or alkaline water which makes the above mentioned assumption partially suspicious.

- No experiment was provided regarding the breakage pattern of quartz particles which were not treated in any of the solutions. Absence of such data does not allow for the comparison of the breakage patterns of treated and untreated quartz particles. Therefore, no conclusion can be made on whether any used salt or surfactant solution had a profound effect on breakage pattern of quartz.

Haecker (1984) studied the effect of chemical environment - NaCl, $MgCl_2$, Na_2CO_3, and amine- on drilling rate, tensile strength, and ball-mill grindability (relative to wet grinding) of quartz. His results showed that all of the reagents changed drilling rate

6

and tensile strength of the samples indicating that adsorption might have changed the mechanical properties of the ore samples. For sandstone, all the reagents produced a beneficial effect on the drilling rate as compared to drilling rates in air (Table 2.1). However, for limestone, all the reagents used had a negative effect on rock strength. Ball milling experiments also showed that all chemicals improved breakage of larger particles at acidic pH (Figure 2.4a), whereas the breakage of finer particles was enhanced only within alkaline amine solutions (Figure 2.4b). However, no explanation or experimental evidence was provided on how adsorption of dissolved salt/surfactant species would foster the rock breakage. The added species to wet grinding might also change the flow behavior of slurry which could affect breakage behavior; therefore, no conclusion can be made whether the findings of Haecker (1984) directly reflect adsorption-induced effects on mineral breakage pattern.
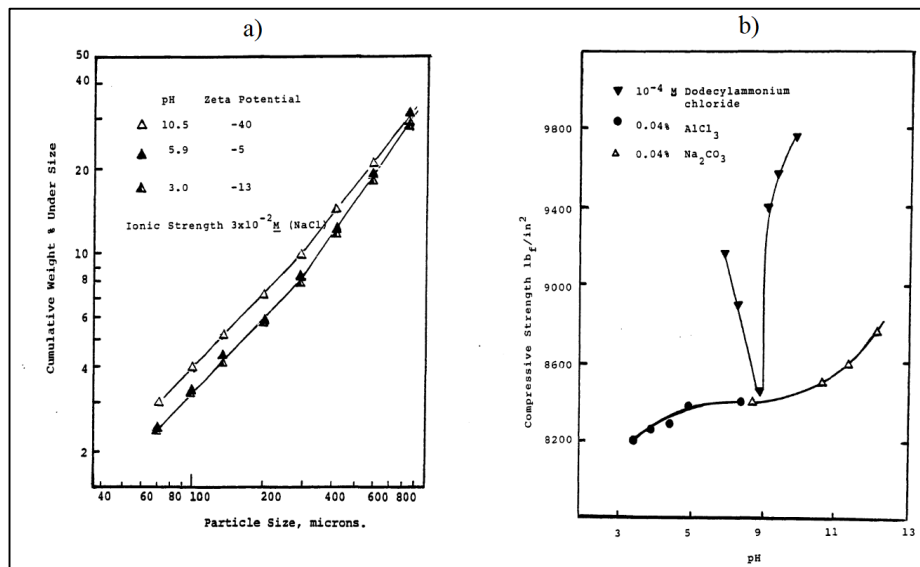
Figure 2.1 (a) Particle size distribution of quartz crushed in 10^{-3} M dodecylammonium chloride (DDACl) plus 10^{-4} M FeCl$_3$ solution at different pH values, by a single impact in a drop-weight mill (b) The effect of the chemical additives and pH on the compressive strength of sandstone (El-Shall, 1980)
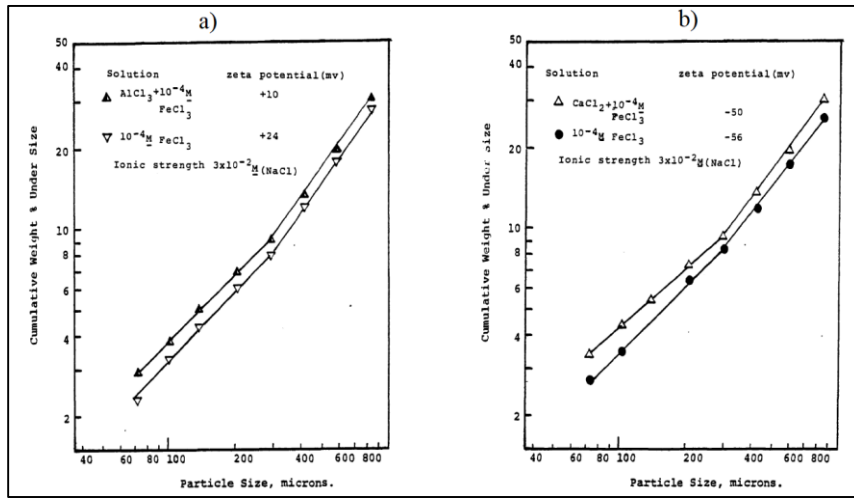
Figure 2.2 Particle size distributions of quartz crushed in (a) 10^{-5} M $AlCl_3$ solution and 10^{-4} M $FeCl_3$ solution at pH 3.0 (b) 10^{-5} M $CaCl_2$ solution and 10^{-4} M $FeCl_3$ solution at pH 10.5 by a single impact in a drop-weight mill (El-Shall, 1980)
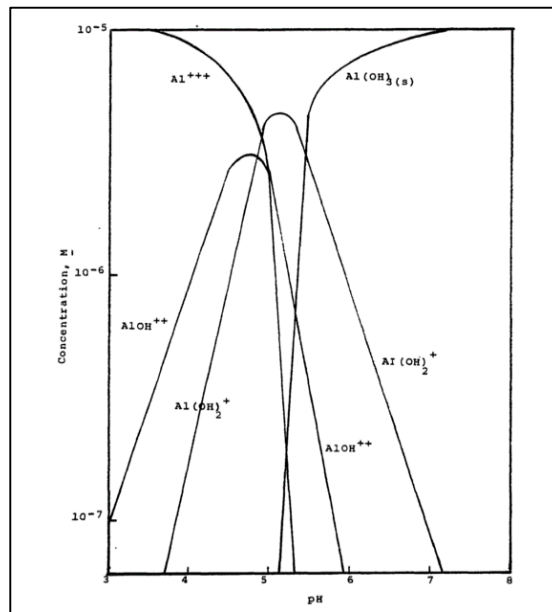
Figure 2.3 Aqueous speciation diagram of Al^{3+} in 10^{-5} M $AlCl_3$ solution (El-Shall, 1980)

Table 2.1 Effect of chemical environment and pH on drilling rate and tensile strength of sandstone (Haecker, 1984)

Environment	% Change					
	pH 3.0		pH 6.0		pH 10.5	
	Drilling	Strength	Drilling	Strength	Drilling	Strength
Air	0.0	0.0	0.0	0.0	0.0	0.0
Water	+25.7 +25.1*	-50.0	+20.7	-32.0	+29.4	-53.0
10^{-2} M NaCl	+20.1	-44.0	+33.6	-42.0	+18.0	-42.0
0.01% AlCl3**	+1.6 +2.0*	-35.0 -33.0*	+31.7 +27.6*	-41.0	+22.3 +16.2*	-39.0 -39.0*
0.05% MgCl2**	+24.1 +15.6*	-40.0	0.0 +1.2*	-28.0	+33.9 +26.6*	-54.0 -48.8*
0.2% Na2CO2**	+14.0 +11.8*	-41.0	+22.9 +18.0*	-30.0	+26.7	-49.0
10^{-5} M Amine**	16.5 +10.9*	-37.0 +40.0*	+6.9	-29.0	+28.2 +25.2*	-46.0

* Duplicate tests.

**Constant ionic strength (10^{-2} M NaCl).
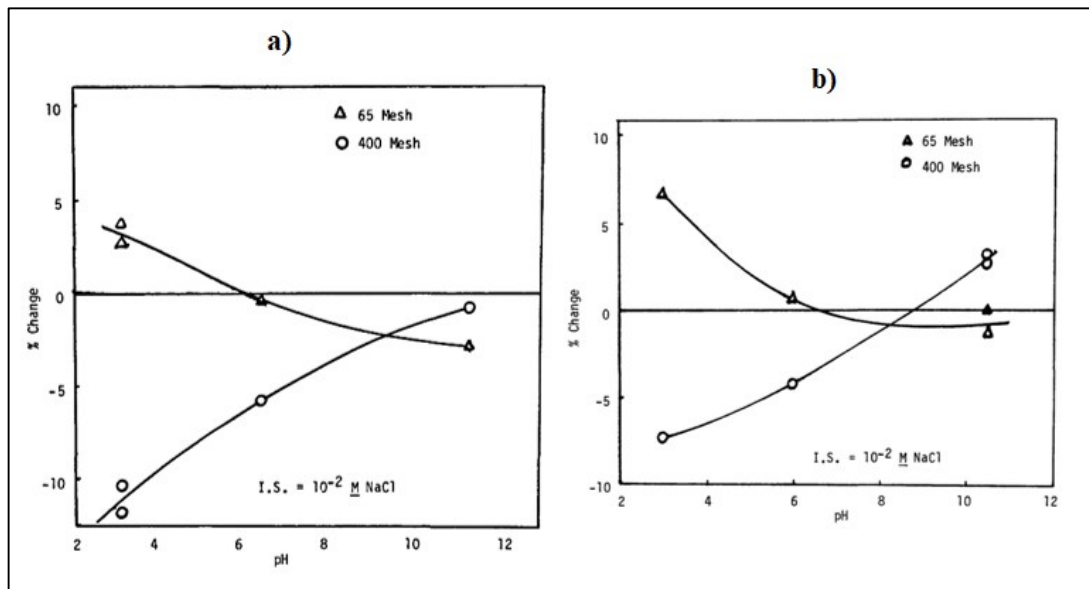
Figure 2.4 Effect of (a) AlCl3 (b) amine solution on ball mill product fineness of quartz as a function of pH (Haecker, 1984). Percent change was calculated with respect to wet grinding without AlCl3.

Hammond and Ravitz (1963) interestingly showed that treatment of alcohols made glass stronger than treatment with water when both environments resulted in lower strength than the one obtained in vacuum (Table 2.2). Regarding this, Moorthy and Tooley (1951) proposed that one of the possibilities was the non-wetting ability of alcohol preventing water to adsorb on glass surface, which lessened the contribution of water to weaken the material.

Table 2.2. Surface energy lowering of quartz and fracture strength of silica glass rods in various saturated organic vapors (Hammond and Ravitz, 1963)

Saturated vapor	Ex-posure time (min.)	Surface free energy lowering (ergs/ cm²)	Average fracture strength (psi)	Num-ber of tests	Standard deviation of the mean (psi)
Vacuum	10	0	13,200	19	700
Benzene (dried)	10	52	13,600	8	1000
Ethyl alcohol	10		12,600	8	1350
Acetone	10	85	11,900	8	600
Butyl alcohol	10		11,600	8	1050
Benzene ("with less than 0.02% water")	10		10,200	8	1000
Ethyl acetate	10		9,900	8	390
Propyl alcohol	10	110	9,600	8	1000
Water	10	244	8,000	7	570
Water	100	244	6,600	6	700

The above mentioned studies brought out the possibility for the use of grinding aids within the size-reduction equipment in order to increase fines with less energy. However, most of the researchers looked for such aids that would improve the rheology of the mill pulp (H. Choi et al., 2010; Choi et al., 2009; Hasegawa et al., 2001; Katzer et al., 1981; Klimpel and Austin, 1982; Klimpel and Manfroy, 1978; Locher and Von Seebach, 1972; Sacks and Tseng, 1983; Somasundaran, 1978; Von Seebach, 1969; Wang and Forssberg, 1995; Zheng, 1997), ignoring the possibility that grinding aids might change the breakage pattern. It was assumed that a grinding aid may adsorb slowly in the propagating crack (Fuerstenau, 1995; Klimpel and Manfroy, 1978; Locher and Von Seebach, 1972), making stress-corrosion cracking unlikely. It

10

might be quite tedious to detect this phenomenon inside wet mills which requires assessment of the speeds of crack propagation and adsorption of the grinding aid. Nevertheless, the experimental design and findings (Figure 2.1 and Figure 2.2) of El-Shall (1980), which incorporate drop-weight stressing of quartz in dilute salt/surfactant solutions, resemble stressing action under wet ball milling conditions; therefore, they provide supportive evidence for stress-corrosion cracking in ball mills. The grinding aids might also be adsorbed to the mineral surfaces through natural fractures or pores within rocks, altering crystal structure or surface free energy of particles. Even the grinding aid might be adsorbed in gas phase, considering high vapor pressure of liquids in cracks (Somasundaran and Lin, 1972).

In metallurgical applications, material weakening was attributed to segregation of some chemical species or basically to impurities at the crystal boundaries of metals or ceramics which may foster brittle failure in the form of intergranular or transgranular fracture (Babinsky et al., 2014; Hondros et al., 1996; Jones et al., 2001; Jones, 2007; Lynch and Moutsos, 2006; Lynch, 2007; Maiti and Sil, 2010; McMahon Jr., 2001; Nagao et al., 2012; Orowan, 1949; Rice, 1997; Takigawa et al., 1999; Wang et al., 2011; West et al., 2007; Yin et al., 2009). Orowan (1949) pointed out that polycrystalline metals could undergo at least two essentially different types of brittle fracture, transcrystalline and intergranular; which of these would occur depend on the cleavage strength within crystal or the intercrystalline cohesion. Some of the key findings for grain-boundary decohesion and intergranular cracking in materials were summarized below:

- Lynch (2007) discussed that the possible mechanisms for intergranular fracture were either due to segregation of impurity elements to grain boundaries or much higher concentrations of hydrogen ahead of intergranular cracks or at the grain-boundaries.

- Seah (1975) made a comprehensive review on the grain boundary adsorption and the associated changes in mechanical properties. The author stated that segregation to free surfaces and grain boundaries of metals lower the surface and grain boundary energies

in accordance with Gibbs' adsorption isotherm, causing embrittlement. The reduction in brittle stress was also shown to be in proportion to the quantity adsorbed and the size excess of the adsorbate and the matrix atoms. Thus, he concluded that large, segregating atoms such as Cr, Mn, Si, P in steel caused embrittlement whereas small ones which were mainly C, B, Be enhanced ductility.

- Hondros et al. (1996) made quite a detailed review of the effect of chemical segregants interfacial and surface microchemistry of metals. Their work involved the discussion of thermodynamics – through Gibbs' adsorption theorem and Langmuir adsorption isotherm – and kinetics of grain boundary segregation, grain boundary analyses, types of grain boundary segregation (equilibrium vs. non-equilibrium) and metallurgical phenomena affected by segregation. An interesting point within this study was the discussion for the effect of individual segregants on boundary cohesion from the viewpoint of atomic bonds at an interface. The author stated that segregation of an element at a grain boundary led to a redistribution of electron charge density. When the segregating atom was an electro-negative sulphur or phosphorus, the charge was drawn from the surrounding metal atoms to the impurity atom and consequently, the adjacent metal-metal bonds were weakened. Therefore, the bond parallel to the boundary was stronger than that perpendicular to the interface, leading to decohesion of the boundary and grain-boundary embrittlement. On the other hand, when the segregating atom was the less electro-negative one such as boron and carbon, grain boundary cohesion increased since covalent-like bonds perpendicular to the boundary were much stronger than the bonding occurred in parallel direction.

- Lynch and Moutsos (2006) presented a detailed history of fractography in metals. They showed the images of simple fracture patterns (intergranular, dimpled and fatigue) under scanning electron microscope (SEM) and transmission electron microscope (TEM). In the case of intergranular fractures resulting from segregations, the texture was shown to be mainly smooth and featureless (Figure 2.5a), and in some cases blocky (Figure 2.5b) or dimpled (Figure 2.6).

12
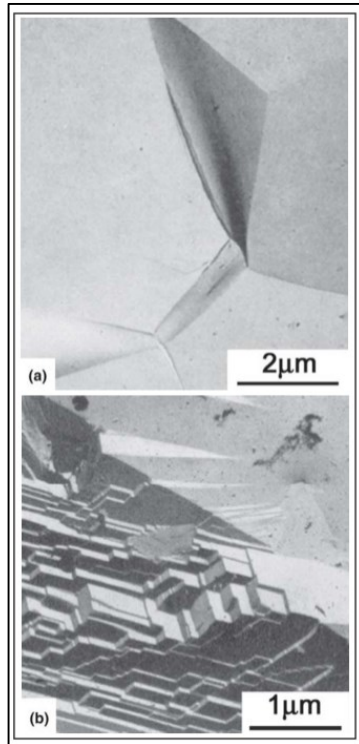
Figure 2.5. TEM of replicas of brittle intergranular fractures at –196 °C in (a) Fe 0.018% O, and (b) commercial-purity Ni with S segregation at boundaries (Lynch and Moutsos, 2006)
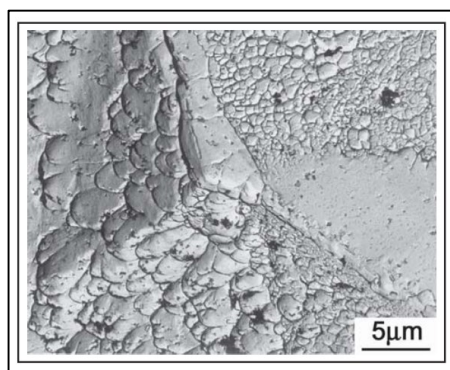
Figure 2.6. TEM of replica of dimpled intergranular fracture in a band-aged Al-Zn-Mg alloy (Lynch and Moutsos, 2006)

- McMahon Jr. (2001) and Nagao et al. (2012) investigated the embrittlement of steels under hydrogen environment. Their results inferred that segregation of hydrogen into steel could mainly promote intergranular fracture under stress.

- Maiti and Sil (2010) explained the relationship between fracture toughness and morphology of sintered Al_2O_3 ceramics. Their paper included clear examples of SEM imaging which revealed grain-boundary structures and fracture modes (Figure 2.7 and Figure 2.8). Their results inferred that the main fracture mode was a mixed mode of intergranular and transgranular fracture where intergranular mode corresponded to higher fracture toughness (i.e. more ductility) due to crack deflection.

- Takigawa et al. (1999) studied the relation between grain boundary bonding state and fracture energy in small amounts of oxide-doped, fine-grained Al_2O_3. Their results suggested that the change in chemical bonding state seemed to affect the grain boundary fracture energy.
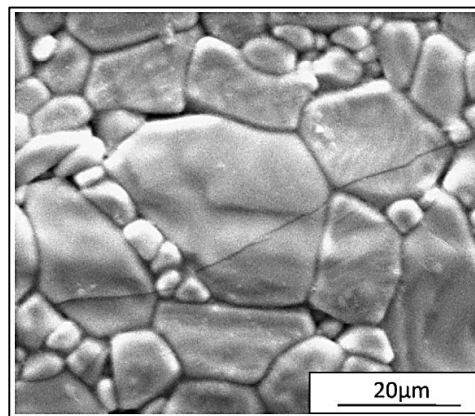
Figure 2.7. SEM image showing transgranular fracture within Al_2O_3 samples sintered at 1700 °C for 3 h (Maiti and Sil, 2010).

14
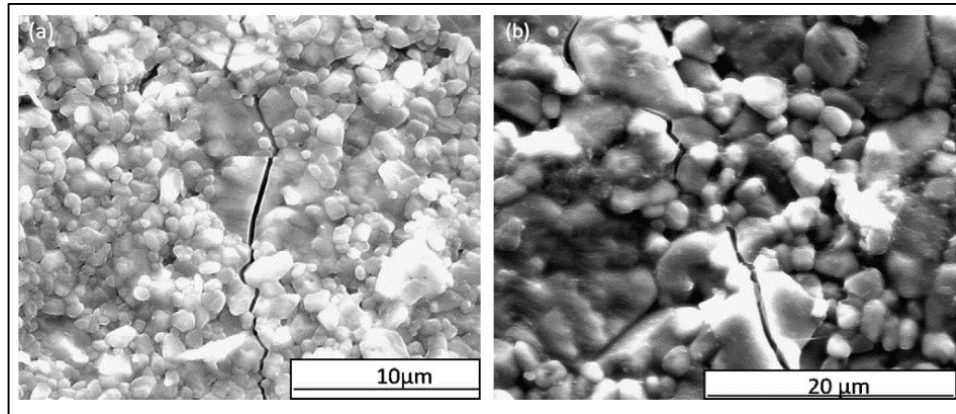
Figure 2.8. SEM images showing intergranular fractures within Al_2O_3 samples sintered at (a) 1500 °C for 3 h, (b) 1600 °C for 3 h (Maiti and Sil, 2010).

- Wang et al. (2000) studied structure of Y and Zr-segregated grain boundaries in alumina showing visible grain boundaries of alumina, also some precipitation at the boundaries, through SEM (Figure 2.9).

- West et al. (2007) also showed the effect of rare earth (RE) dopants on grain boundary cohesion in alumina. Their results showed that a substantially higher proportion of intergranular fracture was observed in RE-doped material relative to the analogous (i.e. same grain size and residual pore content) non-doped material. This was linked to the RE dopant, which segregated strongly to grain boundaries (Figure 2.10), reducing grain boundary cohesion.
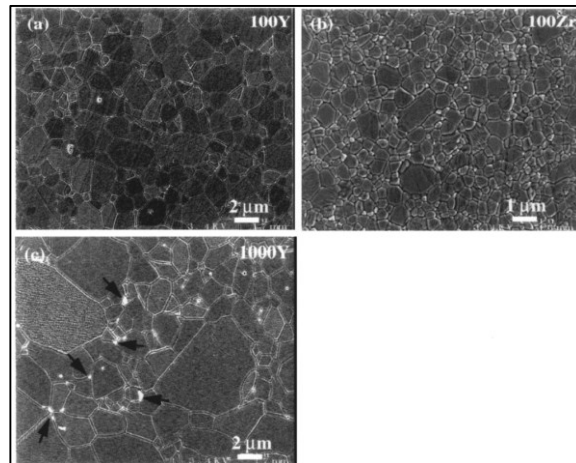
Figure 2.9. SEM images of Y-doped and Zr-doped Al_2O_3 samples: (a) 100 ppm Y_2O_3 doped Al_2O_3; (b) 100 ppm ZrO_2 doped Al_2O_3; and (c) 1000 ppm Y_2O_3 doped Al_2O_3 (Wang et al., 2000). Grain boundaries are visible because of thermal grooving. In (c) some of the YAG, $(Y_3Al_5O_{12})$ precipitates, phase transformation products, at the grain boundaries are indicated by arrows.
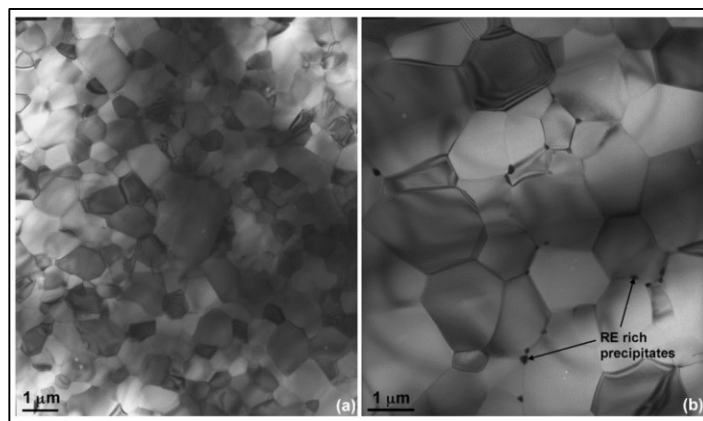
Figure 2.10. TEM micrographs of (a) an La-doped (500 ppm) alumina hot pressed at 1450 °C, and (b) a Gd-doped (500 ppm) alumina hot pressed at 1500 °C (West et al., 2007)

16

2.2. Theoretical Aspects of Mineral Liberation and Grain-Boundary Breakage

Liberation is the main concern in size reduction process if subsequent concentration of valuable mineral(s) from the gangue is the ultimate objective. In this case, liberation phenomenon should be physically identified and explained to design better comminution circuits. Thus, many attempts have been made to model mineral liberation (Austin and Luckie, 1988; Gaudin, 1939; Gay, 2004; Hsih et al., 1995; King, 1979; Klimpel and Austin, 1983; Meloy and Gotoh, 1985; Metha et al., 1989; Stamboliadis, 2008; Wei and Gay, 1999) within two extreme cases: liberation by random fracture and detachment of minerals through their grain-boundaries (Leißner et al., 2016; Mariano et al., 2016). The occurrence of random or intergranular fracturing depends on the relative strength of the mineral phases and their grain boundaries. Intergranular fracturing occurs when the grain boundaries are weaker than the individual mineral phases (Andres and Bialecki, 1986; Bradt et al., 1995; Mariano et al., 2016).

In conventional comminution operations, mechanical size reduction processes are utilized to reduce particle sizes to such a degree that the sufficient degree of liberation (or exposure) of valuable mineral is achieved for the downstream concentration step. However, even decreasing the particle size down to the grain sizes of valuable minerals may not promote the liberation significantly. Gaudin (1939) illustrated that the size reduction may not necessarily rupture bonds between adjacent dissimilar minerals, it may just prevent the occurrence of locking them into small portion of the original lump. Meloy and Gotoh (1985) derived a physical model of mineral liberation when intergranular breakage is restricted, and estimated that overgrinding does not promote liberation to a great extent. On the other hand, if grain boundaries are weaker than the grains themselves, size reduction event results in true liberation. This type of intergranular breakage can be traced through the discrete size distribution curve such that if there is preferential breakage through grain boundaries, there will be an excessive amount of crushed product approximating the size distribution of the individual grains. This is supported by Wen et al. (1998) such that grain-boundary breakage should lead to an abnormal jump in the product fineness if the target mineral

17

is abundant and finely disseminated within the host gangue. In fact, experimental data are available in the relevant literature showing a positive correlation (Figure 2.11) between grain-boundary breakage and increased product fineness (Ali and Bradshaw, 2011; Ozcan and Benzer, 2013; Singh et al., 2015; Zhong et al., 2017).
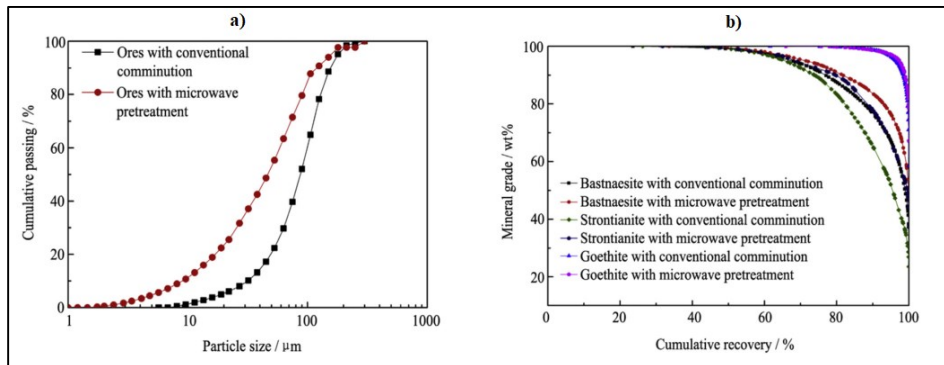
Figure 2.11 Effect of microwave pre-treatment on (a) the progeny size distribution of a rare-earth ore in wet ball mill and (b) the liberation spectra of minerals within the ground product (Zhong et al., 2017).

Traces for grain boundary breakage in minerals could be identified by evaluating the surface textures and liberation behavior of progeny products after breakage. There are some novel techniques such as microwave heating prior to breakage (Ali and Bradshaw, 2011; Kingman et al., 2004; Scott et al., 2008) or high-voltage electrical fragmentation (Andres et al., 1999) where grain-boundary fractures and exposed mineral surfaces (Figure 2.12) can be observed by microscopic analyses (Chanturiya et al., 2011; Charikinya et al., 2015; Guo et al., 2011; Sahoo et al., 2011; Zhong et al., 2017). Such processes have a tendency to enhance liberation of metallic minerals at coarser progeny products (Andres et al., 2001; Kingman et al., 2004; Parker et al., 2015; Scott et al., 2008; Shi et al., 2014; Wang et al., 2012); yet, this improvement seems to be compensated or cancelled out as the progeny size becomes smaller (Figure 2.13).
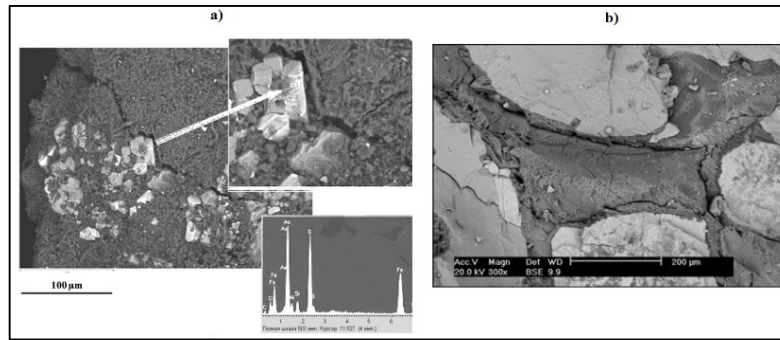
Figure 2.12 Grain-boundary fracture between (a) arsenopyrite (bright) and pyrite after high-voltage breakage (Chanturiya et al., 2011) b)magnetite (bright) and ilmenite after microwave pre-treatment and subsequent grinding (Guo et al., 2011)
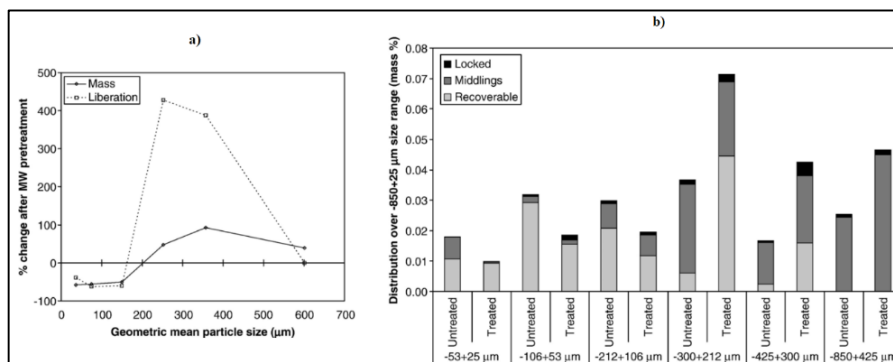
Figure 2.13 (a) Percent change in liberation degree of Cu-sulfides at differently-sized rod milling products of a copper carbonatite ore after microwave treatment (b) liberation spectra for Cu-sulfides in progeny products after rod milling of untreated and microwave-treated copper carbonatite ore (Scott et al., 2008)

2.3. Assessment of Mineral Liberation

The simplest approach to estimate mineral liberation in a population of particles is to calculate degree of liberation which expresses the fractional value (length, area, mass or volume-basis) of a given mineral occurred as apparently free or liberated. The degree of liberation, however, represents a single point on the liberation spectrum

19

(Leißner et al., 2013) and does not give any information regarding mineral grades, mineral associations and surface morphology of the particles. Mineral liberation spectrum is the grade distribution of a mineral phase (King, 2001; Leigh et al., 1996; Lyman, 1995; Petruk, 2000; Schneider, 1995; Wightman and Evans, 2014) whose calculation requires construction of the mineralogical maps of particles. These maps are mainly used in process mineralogy (Celik et al., 2010; Hunt et al., 2011; Lane et al., 2008; Lotter et al., 2011; Pascoe et al., 2007; Tungpalan et al., 2015b; Whiteman et al., 2016) and geometallurgy (Delbem et al., 2015; Lund et al., 2015; Philander and Rozendaal, 2013; Tungpalan et al., 2015a; Zhou and Gu, 2016). They can be constructed by either point/linear (1D) or area (2D) or volumetric (3D) analyses (Al-Wakeel et al., 2009; Leigh et al., 1996). 3D analysis can be performed with sophisticated tools such as x-ray computerized tomography (Lin and Miller, 1996; Mariano, 2016; Medina, 2012; Schena et al., 2007), yielding volumetric or mass-based mineral maps and their associated spectra. 1D and 2D analyses can be done with light and electron microscopes, yielding length-based (Leigh et al., 1996; Minnis, 1984; Petruk, 2000) and area-based (Wightman and Evans, 2014) spectra, respectively. These two analyses require mineralogical mapping of particles mounted in polished or thin or polished-thin sections. Due to their simplicity, 1D and 2D analyses are more preferable than the 3D analysis. Nevertheless, it is still not clear whether they are unbiased (Lätti and Adair, 2001; Parian et al., 2015) or biased estimates of 3D spectrum (Al-Wakeel et al., 2009; Gräbner and Lester, 2016; Medina, 2012; Parian et al., 2015).

1D and 2D mapping can be done with scanning electron microscope (SEM) tools (Fandrich et al., 2007; Zhou and Gu, 2016) or optical microscopes (Craig and Vaughan, 1994). Mineral liberation analyzer (MLA) or QEMSCAN is basically SEM adapted with backscattered electron imaging (BSE) and energy-dispersive x-ray spectrometer (EDX), which can make particle detection and mineral mapping automatically (Fandrich et al., 2007; Gu, 2003; Petruk, 2000; Sylvester, 2012; Vizcarra et al., 2010). Meanwhile, optical microscopes make visuals of particle surfaces by collecting reflected or transmitted light. These visuals are stored by light-sensitive

camera onto digital pictures and further evaluated with certain image processing tools to segment surfaces into color channels, each channel belonging to a different mineral. Such tools include multispectral imaging (Hunt et al., 2011, 2010; Lane et al., 2008; Pirard et al., 2007), color thresholding (Celik et al., 2010; Delbem et al., 2015; Donskoi et al., 2007; Lane et al., 2008) and image classification algorithms (Camalan et al., 2017; Hunt et al., 2010; Köse et al., 2012).

Estimation of the area-basis liberation spectrum requires calculation of the mineral grade of particles. The grade of a mineral (g_i %) in any particle i is given as:

$$g_i = 100 * [A_{chr,i} / (A_{chr,i} + A_{gang,i})] \qquad (1)$$

where $A_{chr,i}$ and $A_{gang,i}$ are the areas of chromite and gangue, respectively, in particle i. The liberation spectrum can be constructed either by plotting number-based distribution of discrete grade classes (Figure 2.14) or by grade-recovery plots, i.e. area-based recovery (%) of overall mineral content to each one-sided grade class (Figure 2.15).
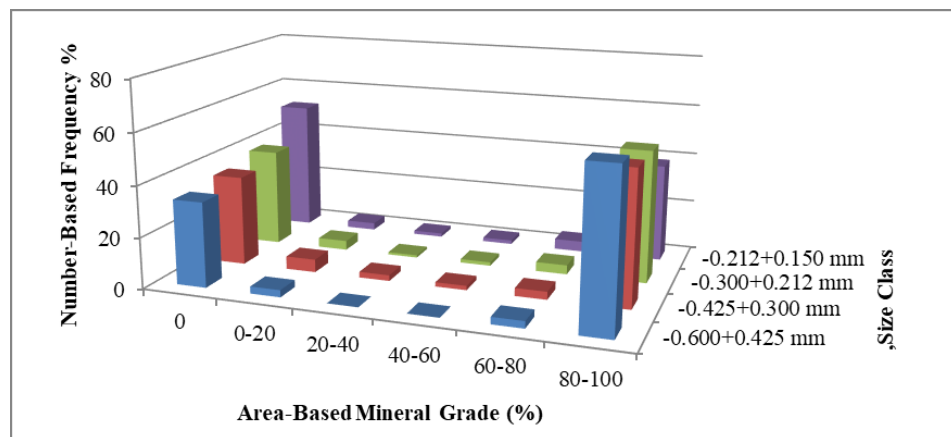
Figure 2.14 An illustration for number-based mineral-grade distribution
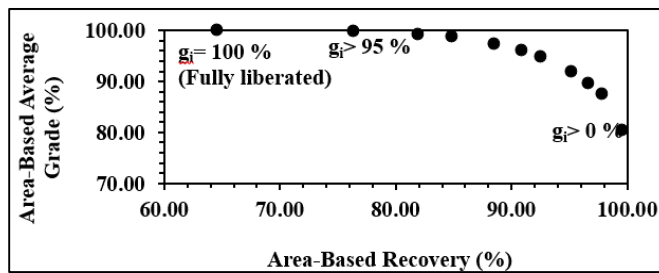
Figure 2.15 An illustration for area-based grade-recovery plot

2.4. Aqueous Chemistry of Oxide Minerals

Aqueous chemistry of the oxide minerals is governed by the development of surface complexes and surface charge at the mineral-water interface (Oelkers et al., 2009; Smith, 1999; Stumm, 1995; Tamura et al., 2001). The surface layers have fewer neighboring molecules than bulk; therefore, they are more reactive than the bulk. When the silicate surface is in contact with water, H_2O molecules tends to coordinate with the surface sites and dissociate into positively (H_3O^+) or negatively (OH^-) charged groups on the surface, depending on the pH of the water. That is, excess hydronium ions in acidic water are retained on the surface yielding positive charge; whereas excess hydroxyl ions in alkaline water give negative surface charge. The pH where the overall surface charge is zero is termed as point of zero charge (pH_{pzc}). Then, when $pH < pH_{pzc}$, the average surface charge is positive and anionic species in water are readily attracted to surface. Meanwhile, when $pH > pH_{pzc}$, the surface charge is negative and cationic species in water are readily attracted to the surface.

Accumulation of H^+ or OH^- species on the surface yields two different dissolution mechanisms for Mg-silicates: (i) metal-proton exchange or proton-exchange or protonation at acidic pH (Blum and Lasaga, 1988; Brady and Walther, 1989; Crundwell, 2014; Liu et al., 2006; Oelkers, 2001; Pokrovsky and Schott, 2000a; Rosso and Rimstidt, 2000; Stumm, 1992) preferentially releasing Mg, and (ii) hydrolysis or deprotonation at alkaline pH preferentially releasing Si (Blum and Lasaga, 1988; Brady and Walther, 1989; Crundwell, 2014; Oelkers, 2001; Pokrovsky and Schott,

22

2000a; Stumm, 1992). Silicate minerals are susceptible to protonation/hydrolysis even at ambient conditions (Chou and Wollast, 1984; Lin and Clemency, 1981; Pokrovsky and Schott, 2000a; Teir et al., 2007). The protonation is due to the exchange of H^+ with Mg^{2+} ions yielding a polymerized, rich Si-layer on the surface whereas the hydrolysis is due to the adsorption of OH^- on Mg-O-Mg bonds, releasing Si^{4+} and giving a Mg-rich surface layer (Figure 2.16). Kinetic studies on the silicate dissolution reveal that both of these two reactions tend to slow down in the neutral range (Blum and Lasaga, 1988; Pokrovsky and Schott, 2000a; Wogelius and Walther, 1991). Experimental data are available in the literature supporting the prevalence of proton-exchange and hydrolysis by means of spectroscopic analyses (Agrawal and Mehra, 2016; Daval et al., 2013; Pokrovsky and Schott, 2000b; Rosso and Rimstidt, 2000). Chromite mineral, on the other hand, has a durable spinel structure in water (Lumpkin, 2001) and can be dissolved only under concentrated acidic solutions at elevated temperatures (Geveci et al., 2002; Vardar et al., 1994; Zhao et al., 2014) or concentrated alkaline solutions at elevated temperatures and pressures (Amer and Ibrahim, 1996; Parirenyatwa et al., 2016; Zhang et al., 2014).
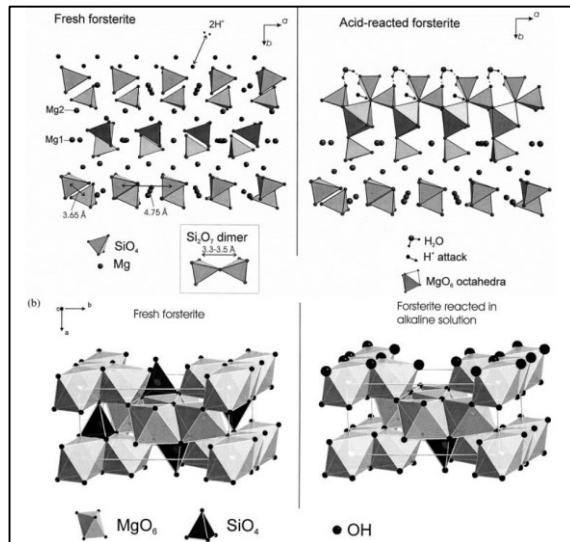
Figure 2.16 A schematic illustration for the surface structure of forsterite in acidic or alkaline conditions (Pokrovsky and Schott, 2000a)

The effect of salts and surfactants on the aqueous chemistry of oxide minerals can be predicted using theoretical concepts of surface complexation in water-oxide surfaces defined by Stumm (1995), through formation of bonds with H^+, OH^-, metal ions and anionic ligands (Table 2.3). The metal ions and ligands could make (i) inner-sphere complexes with chemical bonding or outer-sphere complexes with electrostatic attraction or (ii) accumulate in the double-layer (Mogollón et al., 2000; Olsen, 2007; Stumm, 1995).

Table 2.3 Common surface complexation reactions of metal oxide surfaces with H+, metal cations and ligands (Stumm, 1995)

Acid-base equilibria

$$S\text{–}OH + H^+ \rightleftharpoons S\text{–}OH_2^+$$
$$S\text{–}OH (+ OH^-) \rightleftharpoons S\text{–}O^- (+ H_2O)$$

Metal binding

$$S\text{–}OH + M^{z+} \rightleftharpoons S\text{–}OM^{(z-1)+} + H^+$$
$$2\,S\text{–}OH + M^{z+} \rightleftharpoons (S\text{–}O)_2 M^{(z-2)+} + 2\,H^+$$
$$S\text{–}OH + M^{z+} + H_2O \rightleftharpoons S\text{–}OMOH^{(z-2)+} + 2\,H^-$$

Ligand exchange (L^- = ligand)

$$S\text{–}OH + L^- \rightleftharpoons S\text{–}L + OH^-$$
$$2\,S\text{–}OH + L^- \rightleftharpoons S_2\text{–}L^+ + 2\,OH^-$$

Ternary surface complex formation

$$S\text{–}OH + L^- + M^{z+} \rightleftharpoons S\text{–}L\text{–}M^{z+} + OH^-$$
$$S\text{–}OH + L^- + M^{z+} \rightleftharpoons S\text{–}OM\text{–}L^{(z-2)+} + H^+$$
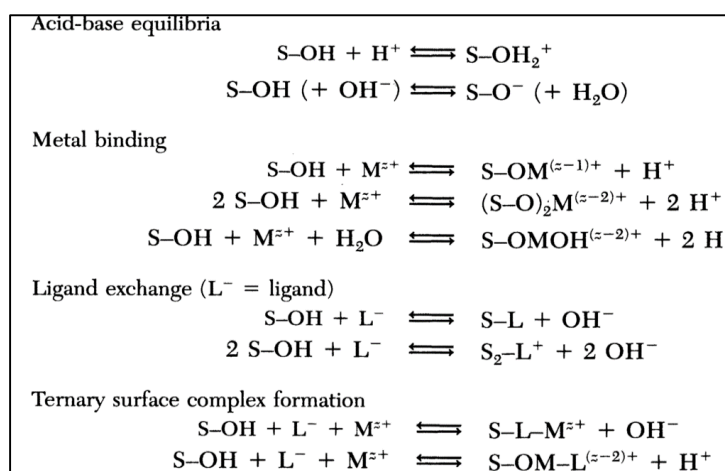
The experimental data in literature regarding the effect of surfactants and inorganic salts (or electrolytes) on aqueous chemistry of chromite and Mg-silicate minerals is quite rare. However, various examples could be given to support the idea that dissolved salt and surfactant species can make surface complexes with oxide minerals:

- The cationic components of salts can accumulate on the negatively-charged quartz surfaces above pH_{pzc} due to electrostatic attraction, bringing H_2O molecules to Si-O bonds and fostering hydrolysis (Agrawal and Mehra, 2016; Icenhower and Dove,

2000; Wang and Giammar, 2013). For Mg-silicates, such cationic components are likely to form surface complexes with Si-O layer, allowing H^+ ions to dissolve Mg-sites (Agrawal and Mehra, 2016; Wang and Giammar, 2013). Meanwhile, surface complexes with negatively-charged Al-hydroxys may inhibit hydrolysis of quartz in alkaline conditions (Bickmore et al., 2006).

- Adsorption of oxyanions (sulphate, phosphate, nitrate) may form surface-complexes on Al-oxide and Mg-silicate minerals fostering proton-exchange in acidic water (Flaathen et al., 2010; Mogollón et al., 2000; Ridley et al., 1997; Rozalen and Huertas, 2013); yet, they have little or no effect on hydrolysis in the alkaline range (Flaathen et al., 2010). Carbonate species are expected to form surface-complexes on Mg-silicates at neutral to alkaline pH, inhibiting hydrolysis (Pokrovsky and Schott, 2000a; Tsuji et al., 2003; van Geen et al., 1994; Wogelius and Walther, 1991).

- Organic ligands may form surface complexes fostering protonation at acidic to slightly-acidic pH. Examples for this case can be given for complexation of phthalate and oxalate with Mg-O sites in forsterite (Liu et al., 2006; Morris and Wogelius, 2008; Olsen and Donald Rimstidt, 2008; Wogelius and Walther, 1992, 1991) and complexation of anionic surfactants (sodium dodecyl sulfate (SDS) and rhamnolipid) with goethite surfaces (Carrasco et al., 2008).

- Anionic and cationic flotation collectors, which are basically organic ligands, may chemisorb to the metal hydroxys, even if the dissolved surfactant species and surfaces possess the same charge (Feng and Aldrich, 2004; M. C. Fuerstenau, 1995; Gallios et al., 2007). High flotation recoveries of chromite mineral with anionic surfactants at either acidic or alkaline environment may give supporting evidence for chemisorption (Figure 2.17). Besides, flotation recovery of quartz with amine acetate was observed to be maximum at alkaline environment (Figure 2.18a) due to chemisorption of negatively-charged amine precipitates (Figure 2.18b) on the negatively-charged quartz (M. C. Fuerstenau, 1995).
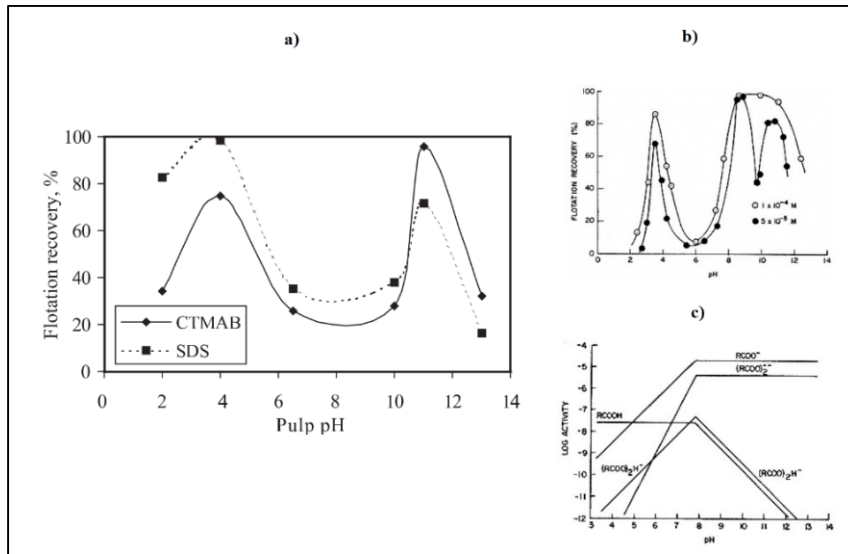
Figure 2.17 Flotation recovery of chromite (a) with 150 mg/L sodium dodecyl sulfate (SDS) and cetyl trimethyl ammonium bromide (CTMAB) as a function of pH (Feng and Aldrich, 2004) (b) with Na-oleate as a function of pH and oleate concentration. (c) logarithmic concentration diagram of 10^{-4} M Na-oleate (M. C. Fuerstenau, 1995).
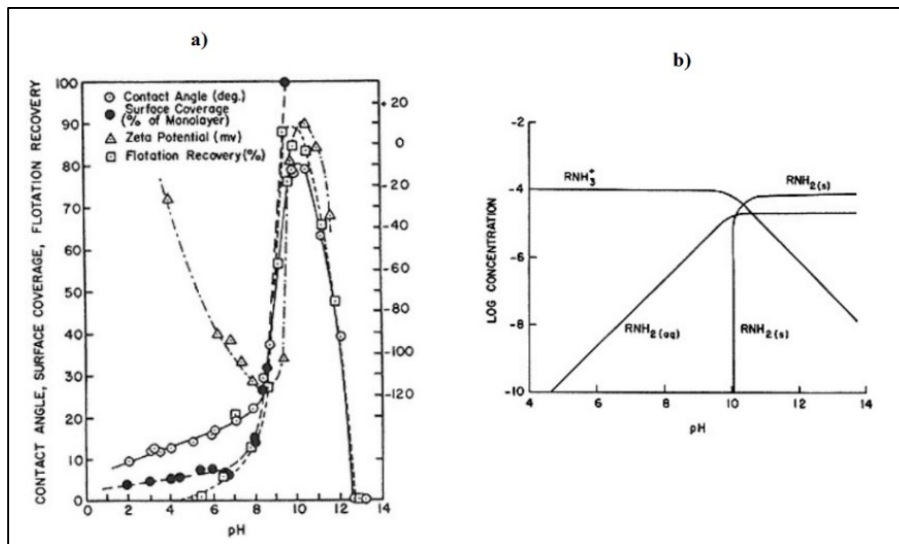
Figure 2.18 (a) Change in the flotation recovery of amine as a function of pH. (b) logarithmic concentration diagram of 10^{-3} M amine (M. C. Fuerstenau, 1995)

2.5. Concluding Remarks

The literature studies regarding the effect of chemical aids on rock breakage focused on monomineralic rocks containing a major amount of silicate or carbonate minerals (El-Shall, 1980; Haecker, 1984). Therefore, they could not provide any information about the effect of aids on mineral liberation. The grinding aids in aqueous environment were found to be effective at certain pH and/or additive concentration in order to achieve finer products (El-Shall, 1980; El-Shall and Somasundaran, 1984a, 1984b; Haecker, 1984; Ryncarz and Laskowski, 1977; Sacks and Tseng, 1983; Wang and Forssberg, 1995). Surfactants were found to be the most effective in alkaline conditions and low concentrations; whereas electrolytes were found to be effective only in acidic conditions.

In the previous studies regarding adsorption-induced effects on particle breakage, the experimental setups were designed to conduct particle breakage under aqueous environment assuming that the chemical species could only diffuse into particle by propagating cracks induced by stressing (stress-corrosion cracking). Meanwhile, most of the researchers ruled out adsorption-induced effects assuming that grinding aids could only diffuse slowly from the propagating crack, and could not cause stress-corrosion at the crack tip (Fuerstenau, 1995; Klimpel and Manfroy, 1978; Locher and Von Seebach, 1972). This assumption was oversimplified, and partially disproved by El-Shall (1980). The aids could diffuse faster inside cracks due to their high vapor pressure (Somasundaran and Lin, 1972) or they could even diffuse into the particle from natural defects as well as propagating cracks. Therefore, it may be of practical concern to search for the suitable chemical aids in which they will diffuse into the particle and foster embrittlement without the need for external stress.

The primary objective for chemical aids is about selecting the suitable ones for ball mills that should (i) improve the flow behavior of the slurry or (ii) adsorb to particles, improving their embrittlement towards grain-boundary breakage between minerals. The latter is of particular interest to this thesis. Although extensive previous research work has shown that aqueous species (water or electrolytes or surfactants) can form

surface complexes on oxide minerals (Section 2.4), the studies regarding adsorption-induced effects on particle breakage were mostly empirical which lacked in proving adsorption of chemical aids by means of any spectroscopic or microscopic evidences.

It should be noted that changing fracture and breakage pattern may be insignificant for energy consumption in mills based on the prediction that 1 % of the energy in ball mill actually goes into fracture (El-Shall and Somasundaran, 1984a). Nevertheless, the generated product might be beneficial in further processing and handling steps if liberation is achieved without excessive size reduction by providing intergranular breakage between minerals (D. W. Fuerstenau, 1995; Veasey and Wills, 1991; Wills and Atkinson, 1993). The novel applications for grain-boundary breakage involves stressing and fracturing of grain-boundaries by means of microwave or high-voltage electric energy (Ali and Bradshaw, 2011; Andres et al., 1999; Kingman et al., 2004; Scott et al., 2008); however, they are currently scarce and expensive for industrial applications (Andres, 2010; Kingman et al., 2000). The use of chemical aids to improve grain-boundary breakage in size-reduction circuits may bring superior advantage over these novel methods, in terms of compatibility and the lower costs in size-reduction operations.

Traces for grain boundary breakage in minerals can be identified by evaluating the liberation behavior and mass distribution of progeny products after breakage. Sufficient data are available in literature implying that grain-boundary fracturing leads to finer progeny generation (Ali and Bradshaw, 2011; Ozcan and Benzer, 2013; Singh et al., 2015; Zhong et al., 2017), whereas mineral liberation is improved particularly at coarser progenies (Andres et al., 2001; Kingman et al., 2004; Parker et al., 2015; Scott et al., 2008; Shi et al., 2014; Wang et al., 2012). Besides, grain-boundary fractures on solid textures can be detected by microscopic methods in engineering materials (Lynch and Moutsos, 2006; Maiti and Sil, 2010; West et al., 2007) as well as mineral assemblages (Chanturiya et al., 2011; Charikinya et al., 2015; Guo et al., 2011; Sahoo et al., 2011; Zhong et al., 2017).

CHAPTER 3

MATERIAL AND METHODS

3.1. Material

The sample used in this study was taken from Kef region in Elazığ, Turkey. XRD diffractogram of the sample (Figure 3.1) shows the presence of magnesium-chromite (a solid solution of pure chromite) and some Mg-silicate minerals that include forsterite (an olivine-group mineral) along with lizardite and clinochrysotile (serpentine-group minerals). The oxide composition of the sample determined by the XRF method is given in

Table 3.1 which shows the constituent elements forming chromite and Mg-silicates. Figure 3.2 also gives Cr_2O_3 grade (%) in the individual size fractions of the ore sample.
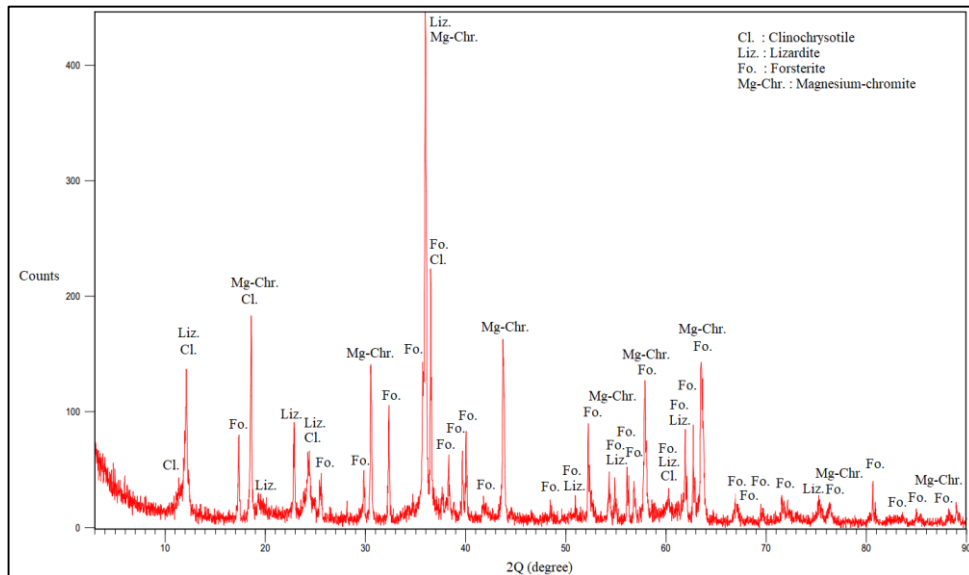
Figure 3.1 XRD analysis of the chromite ore

Table 3.1 XRF analysis of the chromite ore

Species	MgO	Al$_2$O$_3$	SiO$_2$	CaO	Cr$_2$O$_3$	Fe$_2$O$_3$	Sum (%)
Weight	36.70	4.66	27.57	0.45	18.89	11.21	99.48
(%)	35.20	4.92	27.97	0.21	19.56	11.57	99.47
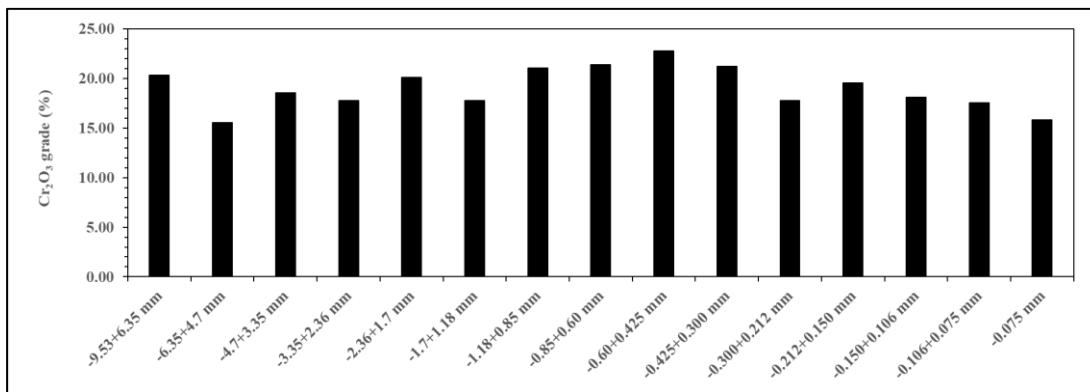
Figure 3.2 Cr$_2$O$_3$ grade (%) in the individual size fractions of the ore sample

The elemental composition of the minerals found in XRD analysis (Figure 3.1) can also be studied through their surface features by using Electron Probe Micro Analyzer (EPMA) tool. The areal (Figure 3.3) and linear (Figure 3.4) elemental maps of some random regions on the sample surface show three distinct features: (i) surfaces rich in Si and Mg, (ii) rich in Cr and Fe, and (iii) grain boundaries where there is a sharp change in concentrations of Si/Mg and Fe/Cr pairs. These EPMA results also support the idea that chromite [(Fe,Mg,Al)Cr$_2$O$_4$], forsterite [(Mg,Fe)$_2$S$_i$O$_4$], and serpentine-group minerals [(Mg,Fe)$_3$((Si,Al)$_2$O$_5$)(OH)$_4$] may appear as solid solutions rather than pure compounds.

30
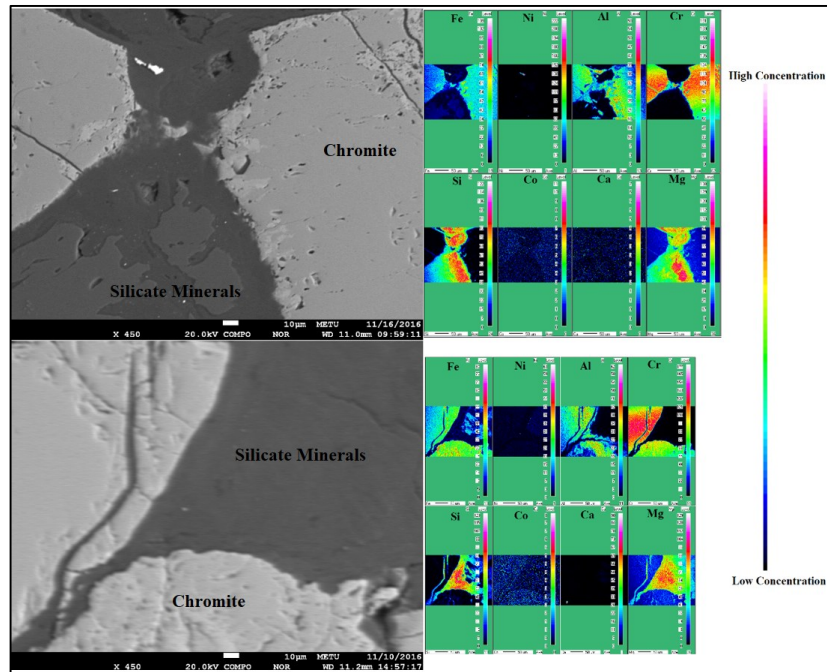
Figure 3.3 Left: Back scattering images containing chromite and serpentine/olivine. Right: Corresponding maps of relative elemental concentrations
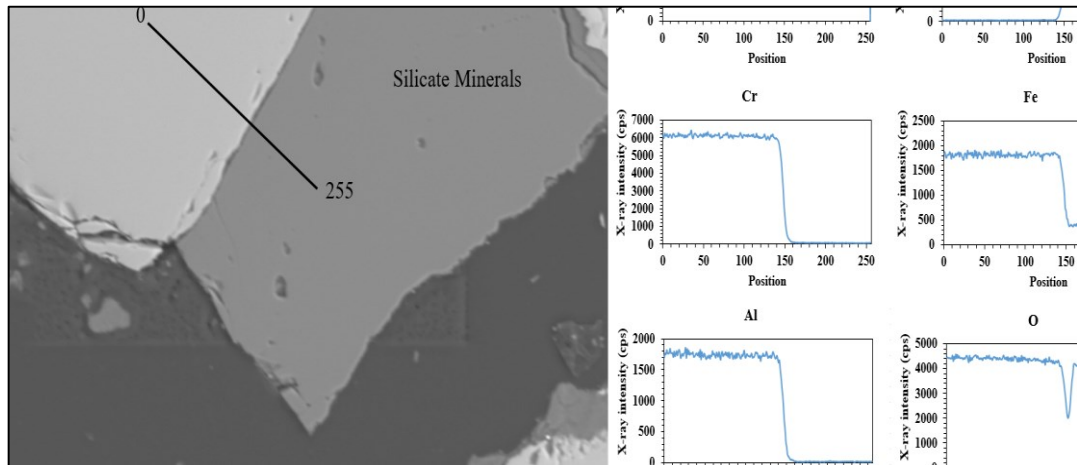
Figure 3.4 (a) A randomly-selected region from untreated sample containing chromite and Mg-silicates. (b) The elemental analysis of the line segment in (a) starting from position 0 and ending at 255.

Figure 3.5 shows the transmitted IR spectra of the ore sample along with chromite- and serpentine-rich fractions. The most significant indicator for serpentine-group minerals is the asymmetrical band at 3690 cm^{-1} which belongs to stretching vibrations of Mg-OH bonds (Fuchs et al., 1998; Heller-Kallai et al., 1975; Khisina et al., 2001; Mellini et al., 2002; Miller et al., 1987; Sanna et al., 2013). The band located at 3646 cm^{-1} is attributed to vibrations of hydroxyls bonding with other cations in serpentine (Mellini et al., 2002; Sanna et al., 2013). These two bands tend to diminish or vanish in the chromite-rich fraction agreeing with the above mentioned findings. The bands at 1083 and 955 cm^{-1} arises from the stretching vibrations of Si-O bonds within the serpentine minerals (Mellini et al., 2002; Sanna et al., 2013). The bands at 1000 and 840 cm^{-1} show the presence of olivine because the vibration of Si-O bonds in olivine structure is mostly seen at the fingerprint region of 1000-450 cm^{-1} (Makreski et al., 2005; Tarte, 1962). The bands about 1640, 1414, 728, 589 cm^{-1} probably belong to chromite mineral, which have been commonly observed on chromite samples (Gyollai et al., 2014). In fact, these bands tend to resolve better in the chromite-rich fraction, which supports the fact that they should belong to chromite. The twin bands at 1640 and 1414 cm^{-1} may arise from H-O-H bending vibration, indicating adsorbed molecular water on chromite (Marincea, 2001; Reddy and Frost, 2005; Roberts et al., 2003). Meanwhile, the bands at 728 and 589 cm^{-1} can be assigned to bonds between the II-III transition metal cations in spinel oxides and oxygen anion (Povnnennykh, 1978; Reddy and Frost, 2005; Ucbas et al., 2014). The twin bands at 2850 and 2925 cm^{-1} indicate the presence of carbon (Kaplan Can and Şahin, 2015; Sivakumar et al., 2013), possibly due to C-H adsorption (Sivakumar et al., 2013) on the ore structure during geological formation. Table 3.2 summarizes sample characterization on FTIR bands.
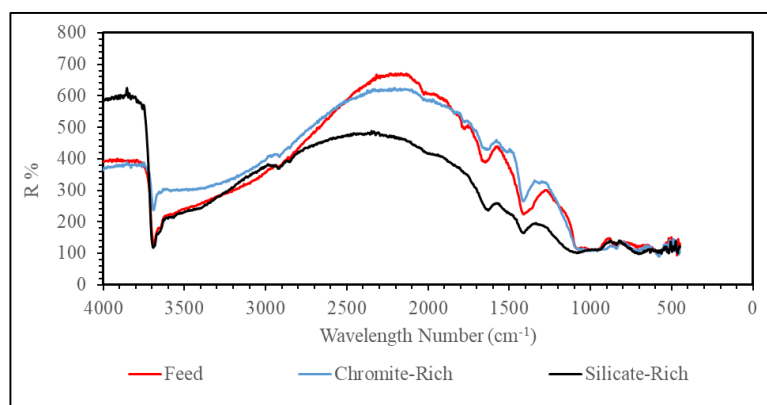
Figure 3.5 Transmitted IR spectra of ore samples along with chromite- and silicate-rich fractions

Table 3.2 Characterization of IR bands

Wave Number (cm^{-1})	Occurrence
3690	Stretching of Mg-OH bonds in serpentines (Fuchs et al., 1998; Heller-Kallai et al., 1975; Khisina et al., 2001; Mellini et al., 2002; Miller et al., 1987; Sanna et al., 2013)
3646	Stretching of other cation-hydroxyl bonds in serpentines (Mellini et al., 2002; Sanna et al., 2013)
2925	C-H-bonding (Sivakumar et al., 2013)
1083,955	Si-O-Si vibrations in tetrahedral sheets of lizardite (Mellini et al., 2002; Sanna et al., 2013)
840	Si-O vibrations in tetrahedral sheets of forsterite (Makreski et al., 2005; Tarte, 1962)
1640,1414, 728, 589	IR bands measured on chromite samples (Gyollai et al., 2014). The twin bands at 1640 and 1414 cm^{-1} for adsorbed molecular water on chromite (Marincea, 2001; Reddy and Frost, 2005; Roberts et al., 2003). The bands at 728 and 589 cm^{-1} show bonds between II-III transition metal cations and oxygen anion in spinels (Povnnennykh, 1978; Reddy and Frost, 2005; Ucbas et al., 2014)

33

The textural features of chromite and silicate minerals can be identified through their surface images from SEM and optical microscope. The chromite grains have smoother surfaces than the silicates (Figure 3.6), while they are fractured and embedded into silicate matrix (Figure 3.7a). This type of chromite texture is mostly inherent to the geological formation of chromite, which is termed as cataclastic textures (Blenkinsop and Fernandes, 2000; Christiansen, 1986; Taşdemir, 2008). In order to detect chromite grains and measure their individual projected-area diameters, supervised color classification (Camalan et al., 2017) was adopted on several microscopic images (Figure 3.7b) taken from the ore lumps. The discrete grain size distributions of chromite were then plotted based on areal and number frequency (%), and the mean of each distribution, excluding the grains which were not visible completely in each image, is shown in Figure 3.8. The number-basis mean diameters of chromite grains are much smaller than what was reported in the literature for similar-textured chromite grains (Taşdemir, 2008).
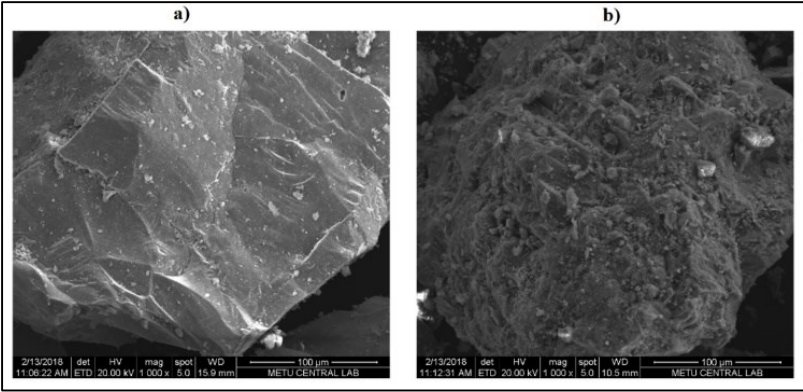
Figure 3.6 Surface textures of a) chromite and b) silicate grains under SEM
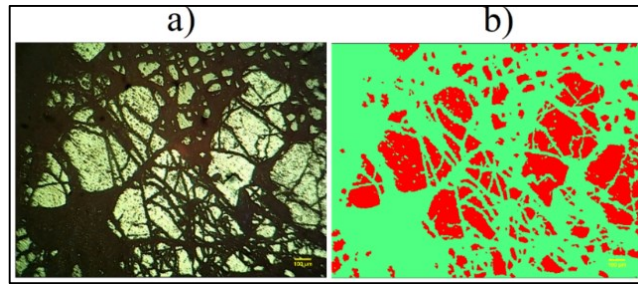
Figure 3.7 (a) Cataclastic chromite texture within the experimental ore material under light microscope, (b) Detection of chromite grains by the supervised color classification
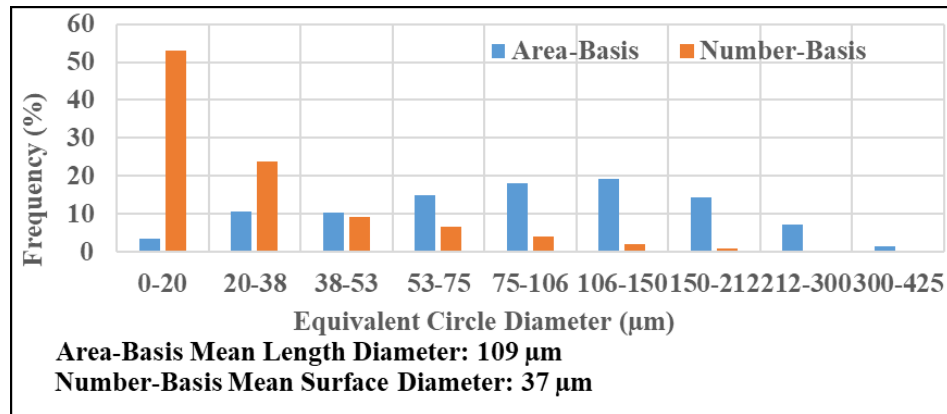
Figure 3.8 The discrete grain size distributions based on areal and number frequency (%) with their corresponding mean diameters

It is of interest to find out if the pore network inside the chromite samples can be convenient for mass transport between treatment liquids and the sample. For that purpose, pore size distribution of -9.53+6.35 mm samples were measured by using Quantachrome Poremaster 60 mercury porosimeter, in a pressure range between 0-1000 psi. The pore size distribution (Figure 3.9) shows that ore has a macro-porous (Zdravkov et al., 2007) or coarsely-fractured network, indicating favorable conditions for the mass transport of chemical species.

35
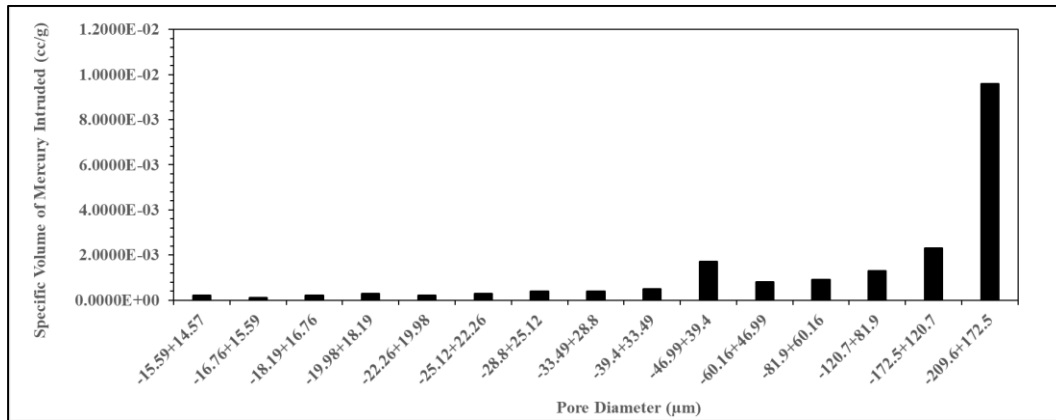
Figure 3.9 Cumulative pore size distribution of ore sample

3.2. Methods

The experimental methods and the flow sheet are summarized in Figure 3.10. They will be described in the following sections.
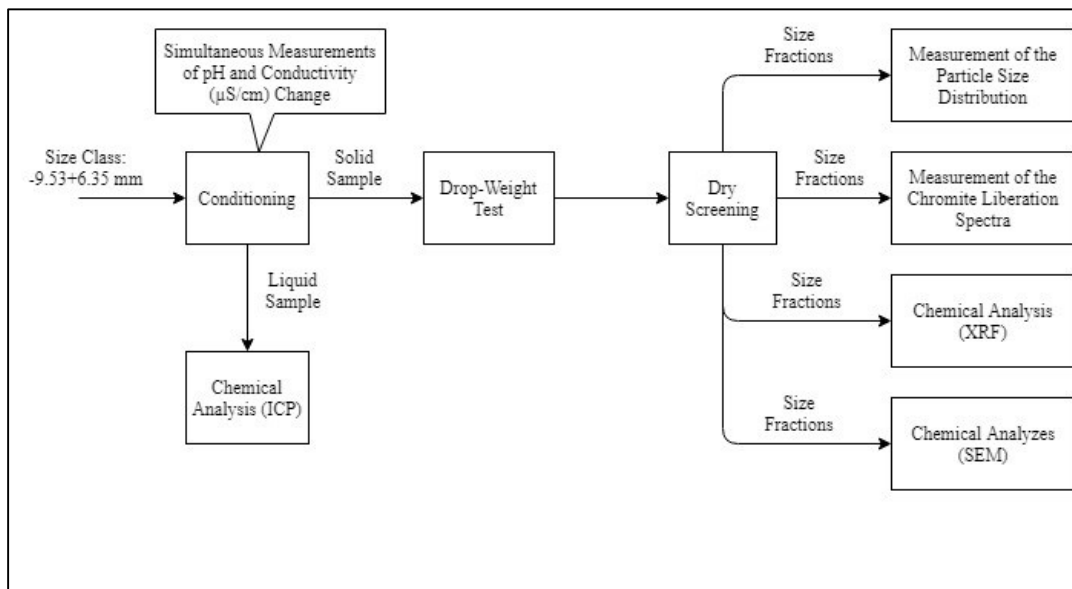
Figure 3.10 Experimental flow sheet

3.3. Chemical Pretreatment Tests

-9.53+6.35 mm chromite samples were treated either in distilled water or various dilute (10^{-4} M) solutions of salts or surfactants (Table 3.3) prior to their breakage in the drop-weight tester. Particles within size range were selected for pretreatment because they can be easily broken one-by-one in the drop-weight tester, and they are mostly present in the feed of tumbling mills. Pretreatment of samples in distilled water was performed at three different pH values and temperatures, whereas the other experiments in salt or surfactant solutions were performed only under three different pH values and a constant temperature of 50°C. The treatment time and the liquid/solid weight ratio for each experiment were kept constant at 15 minutes and 10, respectively. The constant treatment time of 15 minutes was selected as a value comparable to measured residence times in industrial-scale ball mills (Makokha et al., 2011; Schnatz, 2004; Shi, 2016). Meanwhile, the liquid/solid weight ratio of 10 was comparable to the ones used in the dissolution of silicate minerals (Agrawal and Mehra, 2016; Olsen and Donald Rimstidt, 2008; Siegel and Pfannkuch, 1984). The dilute concentration of 10^{-4} M for salt and surfactant solutions was actually a necessity to provide pH variation in liquid without altering liquid/solid weight ratio significantly. This molar concentration is approximately equivalent to 100 g additive per ton of ore, which is comparable to the concentration of grinding aids in ball mills (Cebeci and Bayat, 2004; El-Shall, 1980; El-Shall and Somasundaran, 1984a; D. W. Fuerstenau, 1995; Haecker, 1984; R. R. Klimpel and Manfroy, 1978).

Table 3.3 Pretreatment test conditions used

Aqueous Pre-Treatment Environment		Experimental Conditions
Distilled Water		Mass ratio of liquid to solid = 10 Initial pH: 3, 6, 10 Temperature: 30°C, 50°C, 90°C Treatment Time: 15 min
Dilute (10^{-4} M) Salt Solutions (Based on the common anion)		
Anion	**Salt Species**	
Cl^- salts	NaCl, FeCl, MgCl$_2$, FeCl$_2$	
NO_3^- salts	NaNO$_3$, Mg(NO$_3$)$_2$, Fe(NO$_3$)$_3$, Al(NO$_3$)$_3$	
SO_4^{2-} salts	Na$_2$SO$_4$, FeSO$_4$, MgSO$_4$, Al$_2$(SO$_4$)$_3$	
PO_4^{3-} salts	Na$_4$P$_2$O$_7$	Mass ratio of liquid to solid = 10
CO_3^{2-} salts	Na$_2$CO$_3$	Initial pH: 3, 6, 10
HCO_3^- salts	NaHCO$_3$	Temperature = 50°C
		Treatment Time: 15 min
Dilute (10^{-4} M) Surfactant Solutions		
Dodecylammonium chloride (DAC)		
Sodium Lauryl (Dodecyl) Sulfate (SLS)		
Sodium-Oleate (Na-oleate)		
Potassium Ethyl Xanthate (PEX)		
Sodium Iso Butyl Xanthate (SIBX)		
Sodium Iso Propyl Xanthate (SIPX)		

The initial pH of the liquid was adjusted by using 1 M, and 0.01 M HCl or NaOH solutions. Temperature of the unstirred treatment liquid was adjusted via IKA C-MAG HS7 heater with contact thermometer so that the temperature was maintained within ± 2 % of the required value. The pH and absolute conductivity were measured at 5-min time intervals by using Milwaukee Mi180 Benchtop pH/Conductivity meter to get supportive information on the possible reaction mechanisms. The conductivity change was expressed in relative terms with respect to the initial conductivity at the beginning of the experiment. The measurement resolution was ±0.1 unit for pH measurement,

and ±0.1 µS/cm for conductivity. The measurement data of pH and conductivity change during the treatment experiments are provided in Appendix A.

It is of interest to determine the speciation of the electrolytes and surfactants in water to determine the possible chemical species that may form surface complexes with chromite and silicates. The equilibrium diagrams of electrolyte solutions were estimated with the open-source MEDUSA/HYDRA software, which produces the logarithmic concentration of aqueous species of inorganic components as a function of pH (Appendix B). The software operates under Visual Basic codes, and uses pre-defined algorithms to calculate concentrations of various species through a set of equilibrium reactions with known rate constants (Eriksson, 1979; Ingri et al., 1967). The equilibrium diagrams of surfactants were obtained from the literature (M. C. Fuerstenau, 1995; Somasundaran and Wang, 2007).

3.4. Drop-Weight Tests and Dry Screening

After each treatment, particles were immediately taken out from the liquid and broken in the drop-weight tester at a specific impact energy of 10 J/g. (0.28 kWh/t). Figure 3.11 shows the progeny size distributions of the untreated samples with varying specific energy levels, suggesting that an energy level higher than 10 J/g would not produce a significantly finer product. Therefore, an impact energy of 10 J/g seems to be sufficient to produce a fine product at which chromite liberation could be easily observed.
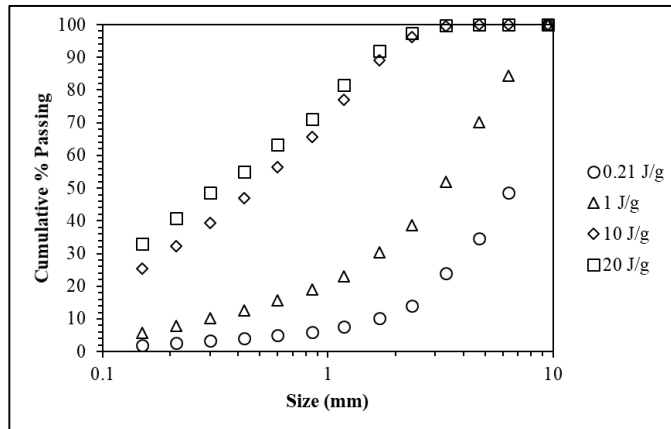
Figure 3.11 Product size distributions of -9.53+6.35 mm untreated feed particles
broken at varying specific energy levels

The progeny particles after each drop-weight test were dried at 60°C in an oven for
15-30 min and then dry screened using a series of sieves to determine the cumulative
size distributions (Appendix C) and to collect individual narrow size fractions. These
size distributions were compared with the ones obtained by the drop-weight breakage
of untreated feeds. The reproducibility of the results was tested with a set of true
replicates of the experiments. Figure 3.12 shows that the drop-weight and subsequent
dry screening yield reproducible data.
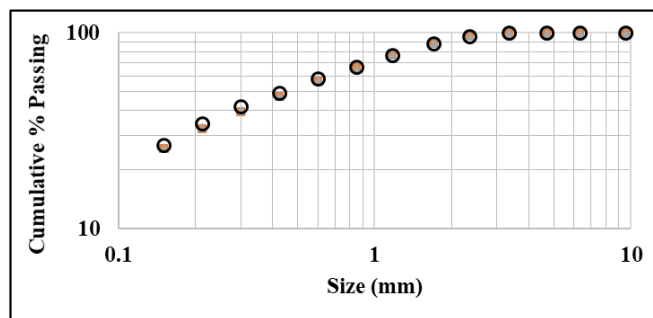
Figure 3.12 Cumulative progeny size distributions obtained after replicated drop-
weight tests on untreated feed material (specific breakage energy = 10 J/g).

40

3.5. Measurement of the Chromite Liberation Spectra

The grade-recovery plots in three progeny fractions (-0.425+0.300 mm, -0.300+0.212 mm and -0.212+0.150 mm) after each treatment experiment were measured by using microscopic analysis described by Camalan et al. (2017). These three size fractions were considered to be suitable for measuring any change in liberation since their dimensions nearly correspond to coarse grain sizes of the chromite mineral in the tested material (Figure 3.8).

For the microscopic analyses, polished sections were prepared in a cold-mounting Epofix kit, then ground and polished on a successive series of diamond and velvet discs using Struers Tegramin 25 or Buehler PowerPro 4000. Images from the polished sections were acquired with Wetzlar 21-D6330 ore microscope attached with Cnscope 5 MP digital CMOS camera. The scale of the image was determined using a micrometer (1 pixel = 2.2947 μm). The resolution of each digital image was 800*600 pixels and the resolution of the microscopic view was about 2 μm.

Additional drop-weight tests on untreated feed particles were performed to produce -0.425+0.150 mm progeny fractions from which chromite-rich and silicate-rich fractions were separated by using the heavy liquid of bromoform (sp.gr. 2.89). Images taken from the polished sections of these chromite- (Figure 3.13a) and silicate-rich fractions (Figure 3.13b) were used for mineral identification.

All the image classification routines were performed in Trainable Weka segmentation Toolbox which was developed by Arganda-Carreras et al. (2017). This toolbox can be found in Fiji, an open-source image processing software (Lind, 2012; Schindelin et al., 2012).

The measurement of liberation spectra by image analysis consists of (i) image pre-processing, (ii) training data extraction, (iii) image classification and post-processing of 2D mineral maps, and (iv) evaluation of 2D mineral maps. The details of these above mentioned processes will be given in the following sections
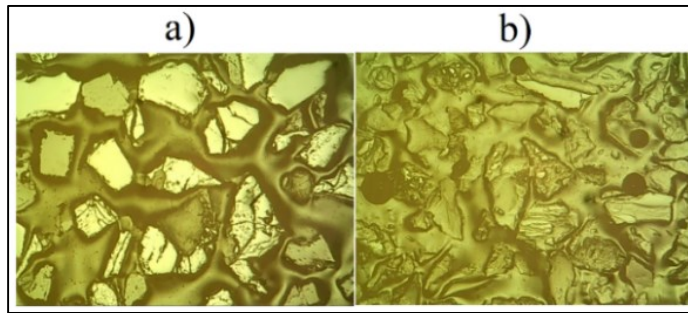
Figure 3.13 Microscope images from chromite-rich (a) and silicate-rich fractions (b).

3.5.1. Image pre-processing

First, the background image (epoxy) surrounding the particles was removed as exemplified as shown Figure 3.14. This was mandatory since the proposed classification method could not differentiate silicate minerals from epoxy because of their similarity in appearance (Lane et al., 2008). Then, the background-free images were further smoothed by the successive application of Median (Khorram et al., 2011) and Kuwahara (Bartyzel, 2016) filters on a 5×5 and 3×3 pixel sub-regions, respectively, in order to eliminate noise on the image (Figure 3.15).
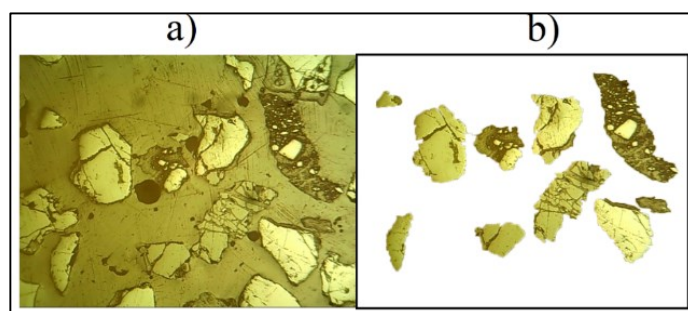
Figure 3.14 A sample of an acquired image (a) and its background-free image (b).
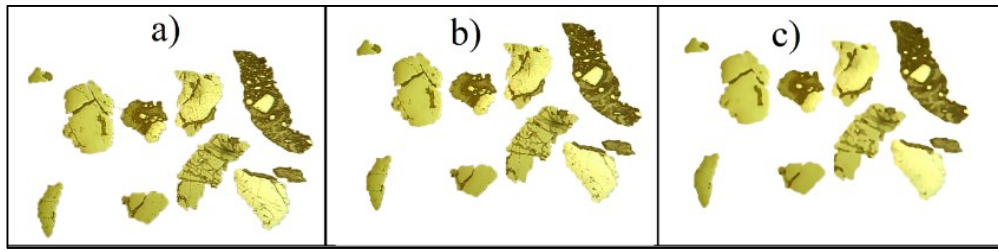
Figure 3.15 An illustrative representation of Kuwahara (b) and Median filter (c),
successively applied to a raw image (a).

3.5.2. Training-data extraction

Various sample textures were assigned into four classes (chromite, serpentine/olivine,
unclassified, and background) from the surface features of chromite-rich and silicate-
fractions (Figure 3.16). The software converts these sample textures into the training
data based on a set of training features in order to predict the class type for unknown
surfaces.
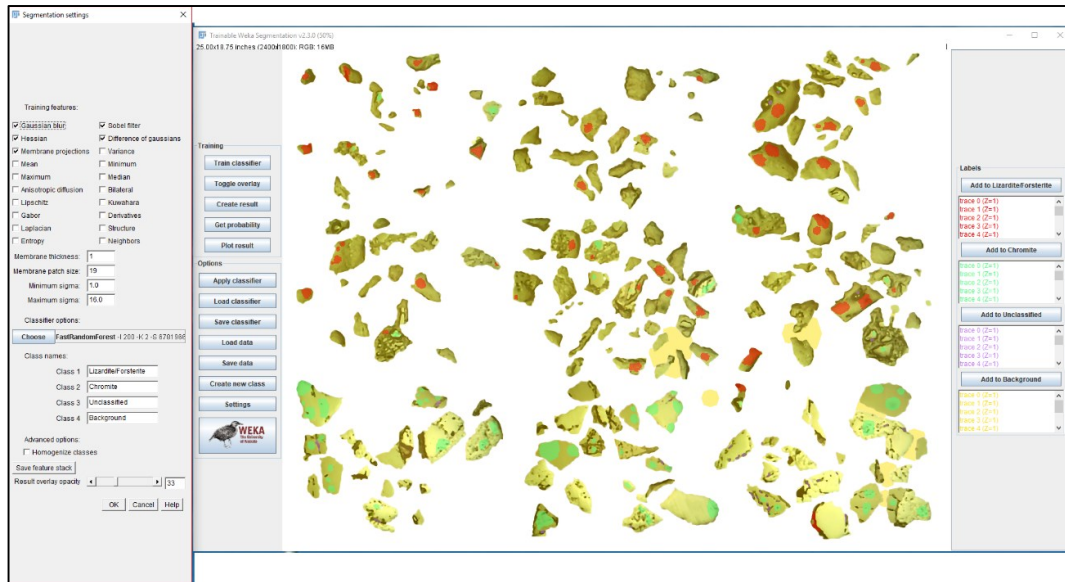
Figure 3.16 The training data extraction for image classification.

3.5.3. Image classification and post-processing of 2D mineral maps

Image classification was performed using the random-forest tree (RFT), a powerful machine-learning algorithm for computer applications (Breiman, 2001; Huang et al., 2015). The method is based upon predicting the class of an unknown pixel based on several input variables, using decision trees constructed from the training features. RFT generates multiple random decision trees that vote on a particular outcome, each vote having an equal weight. For each pixel, the Forest assigns the class that gets most of the votes.

Post-processing stage involved removing the residual noise and artifacts after image classification by using Kuwahara and Median filters to the classified image on a 5 × 5 and 3 × 3 pixel sub-regions, respectively. An illustrative application is given in Figure 3.17.
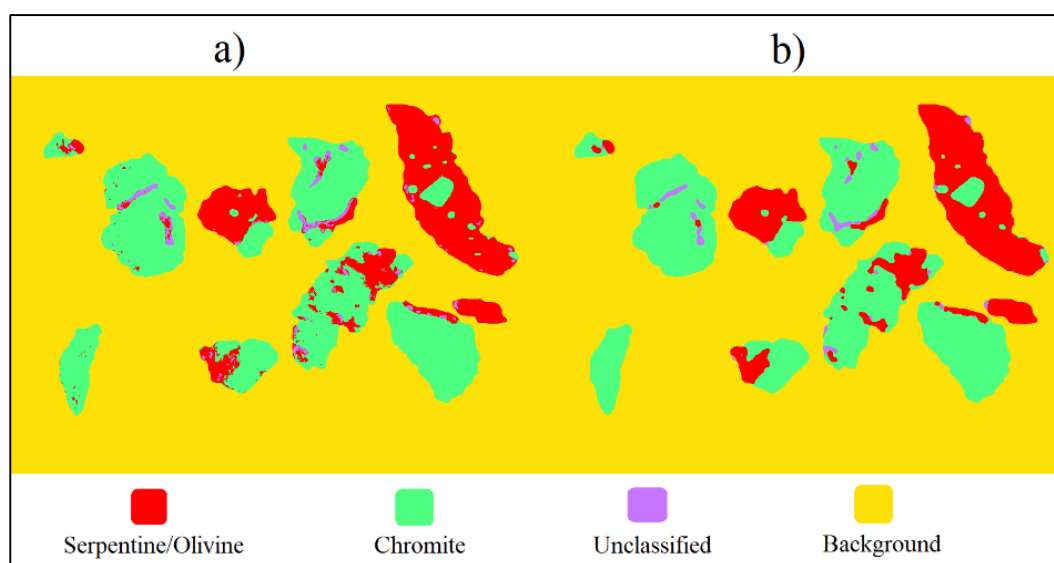
Figure 3.17 An illustrative application for post-processing of 2D raw mineral map (a) by applying Kuwahara and Median filters successively (b).

3.5.4. Evaluation

The data for the liberation spectra were collected by using Clemex Vision software based on a series of procedures including gray thresholds and Boolean operators (Figure 3.18). Particle diameters were measured as equivalent circle diameters. Meanwhile, the areas were measured in μm^2. The liberation spectra was constructed by plotting the grade-recovery plots (Section 2.3). For each measurement, mineral maps of at least 200 particles were constructed to yield accurate and reproducible data for the spectra (Camalan et al., 2017).
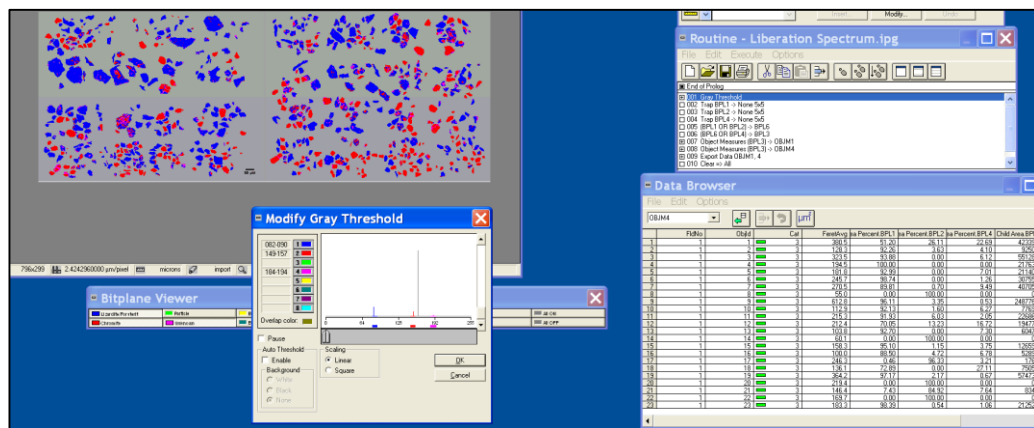
Figure 3.18 Evaluation of 2D mineral maps

3.6. Chemical Analyses

Certain treatment experiments which induced better liberation spectra were replicated and then the treated particles were analyzed under Scanning Electron Microscopy (SEM) - Secondary Electron Imaging (SE), Backscattered Electron Imaging (BSE), Electron Probe Micro-Analyzer (EPMA) - and X-ray Fluorescence (XRF) whereas the liquid samples were analyzed under Inductively Coupled Plasma Mass Spectrometry (ICP-MS). It was aimed to estimate the possible reaction mechanisms that would result in better liberation, simply by looking through evidences for (i) the compositional and

textural changes on the treated particles by EPMA, SE and BSE and (ii) compositional changes in liquid samples by ICP-MS.

Some of the pretreatment experiments which induced better liberation spectra were replicated, then the treated particles were broken and separated into the progeny classes. XRF analyses were then performed to determine Cr_2O_3 grade (%) of these progeny classes and then to find a correlation between chromite liberation and Cr_2O_3 content (%) in the progeny classes.

3.6.1. Inductively coupled plasma mass spectrometry (ICP-MS)

ICP analyses were performed for two reasons: (i) to determine the changes in the concentration of electrolyte or surfactant additives in the liquid phase after the pretreatment of particles, and (ii) to determine the concentration of elemental species dissolved from the solid sample. The analyses were performed with Perkin Elmer DRC II model ICP-MS. Each analysis was conducted with 50 ml sample taken from the liquid after treatment. The liquid samples were acidified with 0.2 ml 5 N HCl prior to ICP analyses in order to prevent the precipitation of ionic species in liquid (Huang and Keller, 1970).

3.6.2. Scanning Electron Microscopy (SEM)

Secondary electron and Backscattered electron imaging were performed on bulk samples of the progeny class -9.53+0.850 mm, to detect exposure of chromite grains due to grain-boundary breakage. The analyses were done with QUANTA 400F Field Emission SEM equipment. The accelerating voltage of the equipment was 20 kV with varying magnification. Prior to analysis, the bulk sample surfaces were coated with Au-Pt.

As an extension of the SEM study, EPMA analyses were performed with JXA-8230 Electron-Probe Micro Analyzer (EPMA) on polished sections of the -0.850/+0.600 mm progeny class. These analyses were conducted to detect any change in chemical composition of the grain-boundary in the case of grain-boundary fracturing. The

46

accelerating voltage of the equipment was 20 kV with a magnification at 400x. Prior to analysis, the polished sections were coated with Au-Pt. Each measurement was taken from a random line section crossing the boundary chromite and silicate minerals.

3.6.3. X-ray Fluorescence (XRF)

XRF analyses were performed to determine Cr_2O_3 grade (%) of the progeny classes and then to find a correlation between chromite liberation and Cr_2O_3 content (%) in the progeny classes. A Spectro IQ model x-ray fluorescence (XRF) spectrometer was used to measure Cr_2O_3 grades (%) of the progeny size classes of the treated samples. Each sample to be analyzed were mixed with HWC, an organic binder, with a solid-to-binder weight ratio of 4.46, and then pressed into a pellet. Additionally, true replicates of Cr_2O_3 grades were measured on the progeny fractions of broken, untreated feed sample in order to measure precision. Results, given in Figure 3.19, show that the above mentioned modal analysis yield reproducible data.
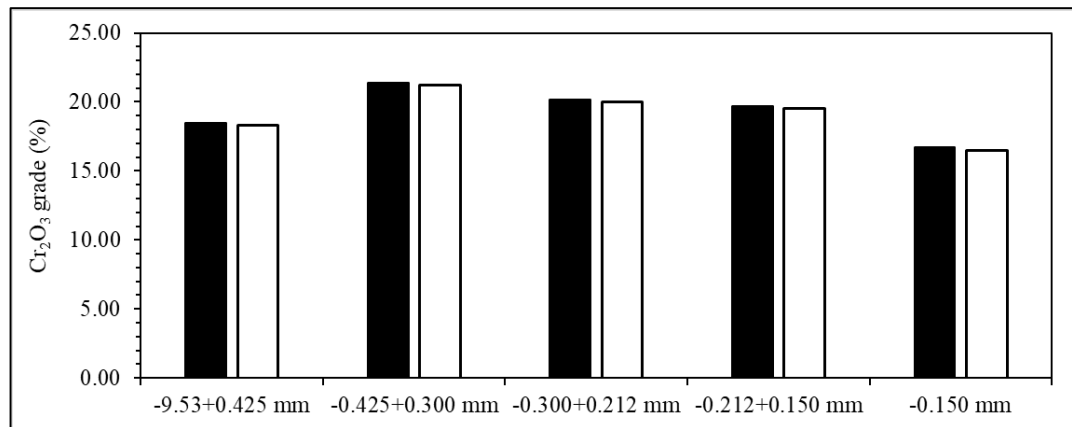
Figure 3.19 Cr_2O_3 grades (%) of progeny size fractions of untreated feed samples obtained after drop-weight breakage

CHAPTER 4

RESULTS AND DISCUSSION

4.1. Pretreatment of Samples in Acidic Water and Acidic Solutions of Salts and Surfactants

Figure 4.1 shows the grade-recovery plots of chromite in progeny particles of the untreated sample and the samples treated in the acidic water at different temperatures. The plots in the progeny sizes of treated samples are lower with respect to those in the progenies of untreated sample. This suggests that pretreatment in acidic water reduces chromite liberation; therefore, it is not expected to improve grain-boundary fracturing.
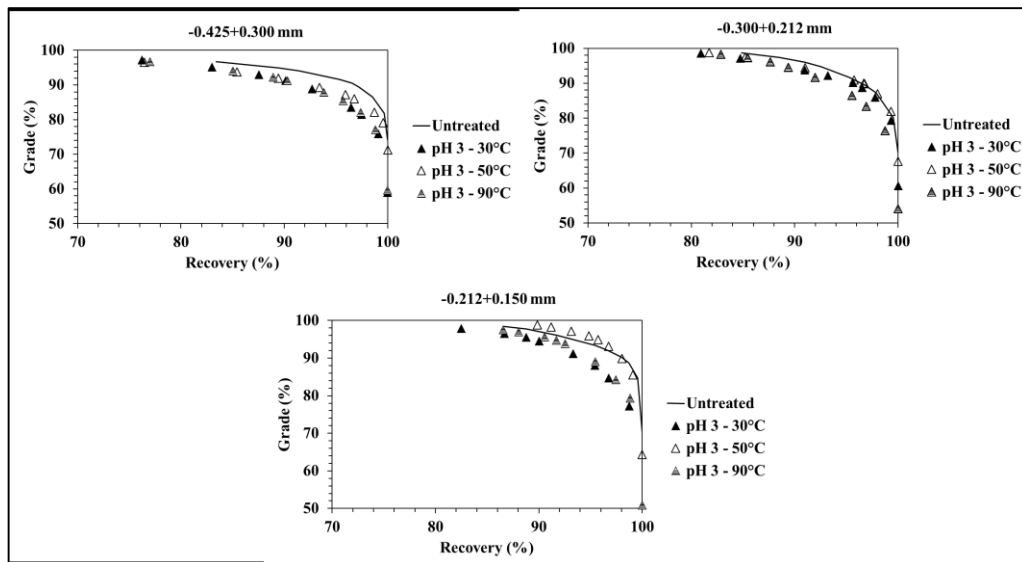
Figure 4.1 Grade-recovery plots of chromite in progeny products of untreated sample and the samples treated in acidic water (pH 3) at different temperatures.

Figure D.1 and Figure D.2 in Appendix D give the relative element compositions on the bulk mineral surfaces and the grain-boundary regions after treatment in acidic water at 50 and 90°C, respectively. Element compositions on the acid-reacted silicate surfaces are uniform on the bulk texture and sharply changing at the grain-boundaries, which is also similar on untreated silicate surfaces (Figure 3.4b). Therefore, no information can be deduced from the surface analyses about how the sample surface have been dissolved by acidic water. However, as shown in Figure 4.2, concentration of dissolved Mg is higher in acidic water, in agreement with the proton-exchange mechanism defined for the acidic dissolution of silicate minerals (Section 2.4). Proton-exchange mechanism is expected to deplete H^+ ions from the water (Huang and Keller, 1970; Lacinska et al., 2016; Lin and Clemency, 1981) which results a decrease in the conductivity of water. The pH and conductivity in acidic water, given in Figure 4.3, decreases during treatment which gives evidence for proton-exchange. Then, it is the proton-exchange mechanism which does not improve grain-boundary fracturing. Since Mg seems to be more abundant in the bulk composition than it is at the grain-boundaries (Figure 3.3), Mg dissolution by proton-exchange is more likely to occur at the bulk silicate texture.
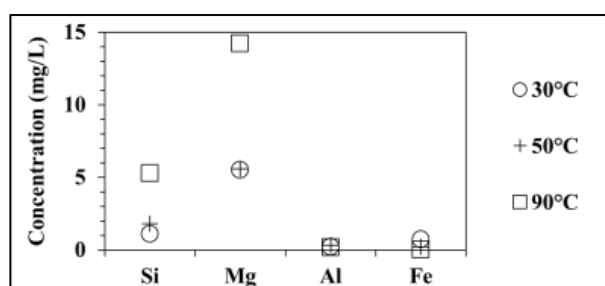
Figure 4.2 Chemical analyses of the acidic water (pH 3) after treatment at different temperatures. Cr concentration is below the detection limit.
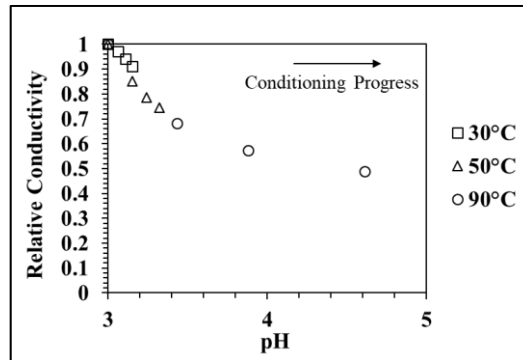
Figure 4.3 pH and relative conductivity change in acidic water (pH 3) during treatment at different temperatures.

Figure 4.4 shows the grade-recovery plots of chromite in progeny particles of the untreated sample and the samples treated in acidic (pH 3) salt solutions and acidic water at 50°C. The grade-recovery plots of chromite in coarser progeny classes rise significantly after pretreatment in most of the acidic solutions of Na, Fe and Ca salts, suggesting that these salt solutions have a tendency to improve chromite liberation. Moreover, as shown in Figure 4.5, the grade-recovery plots of silicate minerals become higher in progeny particles after pretreatment in some of these salt solutions. This suggests that Na, Fe and Ca salts at acidic pH have a tendency to enhance grain-boundary fracturing since their solutions promote both chromite and silicate liberation. Meanwhile, as shown in Figure 4.4, the grade-recovery plots of chromite after pretreatment in the acidic solutions of Mg and Al salts are not significantly higher than those of the untreated sample and the sample treated in acidic water. Therefore, Mg and Al salts at acidic pH are not expected to enhance grain-boundary fracturing.

Figure 4.4 Grade-recovery plots of chromite in progeny products of untreated sample and the samples treated in acidic (pH 3) salt solutions and acidic water at 50°C.

Figure 4.5 Grade-recovery plots of silicate minerals in progeny products of untreated sample (shown by solid and dashed lines) and the samples treated in acidic (pH 3) solutions of Na, Fe and Ca-salts at 50°C (shown by symbols only).

Figure 4.4 shows that any promoting effect of an acidic salt solution on grade-recovery plots of chromite seems uniform in the two coarsest progeny classes; however, it might change at the finest progeny class. Such anomalies bring the question if enhancing grain-boundary fracturing by pretreatment improves chromite liberation in all the progeny classes. Previous experimental studies emphasized in Section 2.2 support that grain-boundary fracturing distributes the liberated mineral grains preferentially to coarser progeny particles. On the contrary, any fracturing mechanism which eventually decreases chromite liberation in coarser progenies is expected to distribute the liberated mineral grains to relatively finer progenies. Therefore, any effect of grain-boundary or other fracturing mechanism on chromite liberation may not be the same in all progeny size classes.

Positive effect of the acidic solutions of Na, Fe and Ca salts on chromite liberation (Figure 4.4) suggests that salt species, as well as H^+ ions, may adsorb on the surface and change the fracture pattern. As shown in Table 4.1, aqueous concentration of some of these salt species decrease during treatment, suggesting that they can form complexes with mineral surfaces. As the proton-exchange mechanism is known to

53

hinder grain-boundary fracturing (Figure 4.1), it should be these salt-surface complexes which should promote grain-boundary fracturing. Equilibrium diagrams in Appendix B show that the cationic species are present within water in their ionic form or as compounds with hydroxyls and other anions. Therefore, cationic salt species might adsorb to the surfaces in different phases. Even the Fe^{3+} ions whose hydroxyls are present in acidic water as a solid precipitate (Figure B.7 and Figure B.9) may be adsorbed by the sample, given the decrease in aqueous Fe^{3+} concentration during pretreatment of samples in acidic $FeCl_3$ and $Fe(NO_3)_3$ solutions (Table 4.1). Anionic species of the dissolved salts are present in their ionic form; therefore, they are expected to adsorb to the surfaces as a single phase.

Table 4.1 Concentration of cationic and anionic salt species before and after treatment in some of the acidic (pH 3) salt solutions

Acidic Salt Solution	Concentration of Cationic Species			Concentration of Anionic Species		
	Before Treatment (mg/L)	After Treatment (mg/L)	Error (±)	Before Treatment (mg/L)	After Treatment (mg/L)	Error (±)
NaCl	2.3	1.9	0.1	* (Cl)	* (Cl)	*
CaCl₂	4.01	3.31	0.1	* (Cl)	* (Cl)	*
FeCl₃	5.58	2.4	0.1	* (Cl)	* (Cl)	*
Fe(NO₃)₃	5.58	2	0.1	* (N)	* (N)	*
FeSO₄	5.58	1.9	0.03	3.21 (S)	3.1 (S)	0.03
Na₂SO₄	4.6	4.4	0.1	3.21 (S)	2.5 (S)	0.1
CaSO₄	4.01	3.9	0.4	3.21 (S)	2.6 (S)	0.4
* Unmeasurable by ICP						

Figure D.3 and Figure D.4 represents the relative composition of certain elements on some randomly-selected surfaces after pretreatment in acidic $FeCl_3$ and $FeSO_4$ solutions. After pretreatment, the relative concentration of Al at the grain-boundaries decrease sharply, showing that acidic solutions of $FeCl_3$ and $FeSO_4$ are able to dissolve the grain-boundary surfaces and promote grain-boundary weakening. Furthermore, decrease in Al concentration at the grain-boundary surfaces is coupled with increases

in the concentrations of elements which constitute $FeCl_3$ and $FeSO_4$ salts. This indicates that salt-surface complexes formed at acidic pH promote grain-boundary weakening by dissolving Al at the grain-boundary surfaces. Meanwhile, Figure D.5 shows a particle surface after pretreatment in $AlCl_3$ solution which does not promote chromite liberation. It is clear that the concentration of elements which constitute chromite and silicate minerals are uniformly changing after treatment, and there is no sign for adsorption of Al and Cl at the grain-boundaries. This suggests that $AlCl_3$ salt at acidic pH does not contribute for the weakening of the grain-boundary structure.

Figure 4.6 presents grade-recovery plots of chromite in progeny classes of untreated sample and sample particles treated in some acidic (pH 3) surfactant solutions and acidic water. The figure shows that grade-recovery plots in coarser progenies rise significantly after pretreatment in the acidic solutions of PEX and SIPX. The grade-recovery plots of silicate minerals, as shown in Figure 4.7, can also be improved by PEX and SIPX solutions, suggesting that they promote grain-boundary fracturing. However, Figure 4.6 shows that pretreatment in acidic solutions of other anionic surfactants and the cationic surfactant DAC do not increase the grade-recovery plots of chromite in progeny particles; therefore, they are not expected to promote grain-boundary fracturing.

Figure 4.6 Grade-recovery plots of chromite in progeny products of untreated sample and the samples treated in acidic (pH 3) surfactant solutions and acidic water at 50°C.

Figure 4.7 Grade-recovery plots of chromite in progeny products of untreated sample (shown by solid and dashed lines) and the samples treated in acidic (pH 3) solutions of PEX and SIPX at 50°C (shown by symbols only).

As PEX and SIPX species in the acidic solution reverse the negative effect of acidity of water on grain-boundary fracturing (Figure 4.1), it is expected that xanthate species should contribute to the grain-boundary weakening by forming surface complexes. As shown in Table 4.2, aqueous S concentration provided to the solution by xanthate species decrease after treatment, suggesting formation of such complexes on particle surfaces. Besides, Figure 4.8 shows that dissolved xanthate (X^-) is expected to gain proton and turn into xanthic acid (HX) at acidic pH; therefore, it should be the xanthic acid that should form surface complexes and promote grain-boundary weakening.

Figure D.6 shows the relative element composition on a particle surface after pretreatment in the acidic PEX solution which promotes chromite liberation. The concentration of C increases at the grain-boundary surfaces which indicate the adsorption of xanthic acid. Besides, adsorption of C to the grain-boundaries is coupled with sharp decreases in Al concentration, suggesting that adsorption of xanthic acid results dissolution of Al at the grain-boundary surface which might promote grain-boundary weakening. On the other hand, Figure D.7 shows a particle surface after pretreatment in acidic DAC solution which does not promote chromite liberation. The concentration of C and N seems to increase at bulk mineral surfaces as well as grain boundaries, giving evidence for the adsorption of aqueous amine species. However, adsorption of amine is coupled with sharp decreases in the concentration of Al at bulk chromite surfaces, and the concentration of Si and Mg in bulk silicate surfaces. This suggests that adsorption of amine enhances the dissolution of bulk mineral surfaces which might hinder grain-boundary fracturing.

Table 4.2 The change in aqueous concentration of S during treatment in the acidic PEX solution

Component	Before Treatment (mg/L)	After Treatment (mg/L)	Error (±)
S	6.4	0	0.02
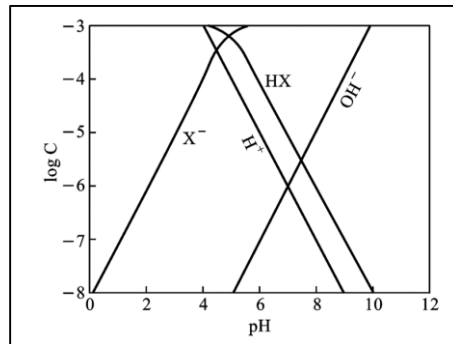
Figure 4.8 Chemical equilibrium of ionic and non-ionic species in 10^{-3} M xanthate solution, X=xanthate (Somasundaran and Wang, 2007).

4.2. Pretreatment of Samples in Slightly-Acidic Water and Slightly-Acidic Solutions of Salts and Surfactants

Figure 4.9 shows the grade-recovery plots of chromite mineral in progeny particles of the untreated sample and the samples treated in the slightly-acidic (pH 6) water at different temperatures. The plots in the progeny sizes of treated samples shift upwards when the pretreatment is conducted at 30°C and 50°C, showing that these conditions yield higher chromite liberation. Figure 4.10 shows that the slightly-acidic water at 30°C and 50°C also improves the grade-recovery plots of silicate minerals in the progeny classes. Therefore, these treatment conditions are expected to enhance grain-boundary fracturing. Meanwhile, Figure 4.9 shows that the sample treated in the slightly-acidic water at 90°C produces grade-recovery plots lower than those of untreated sample. This shows that pretreatment in slightly-acidic water at 90°C does not enhance chromite liberation and grain-boundary fracturing.
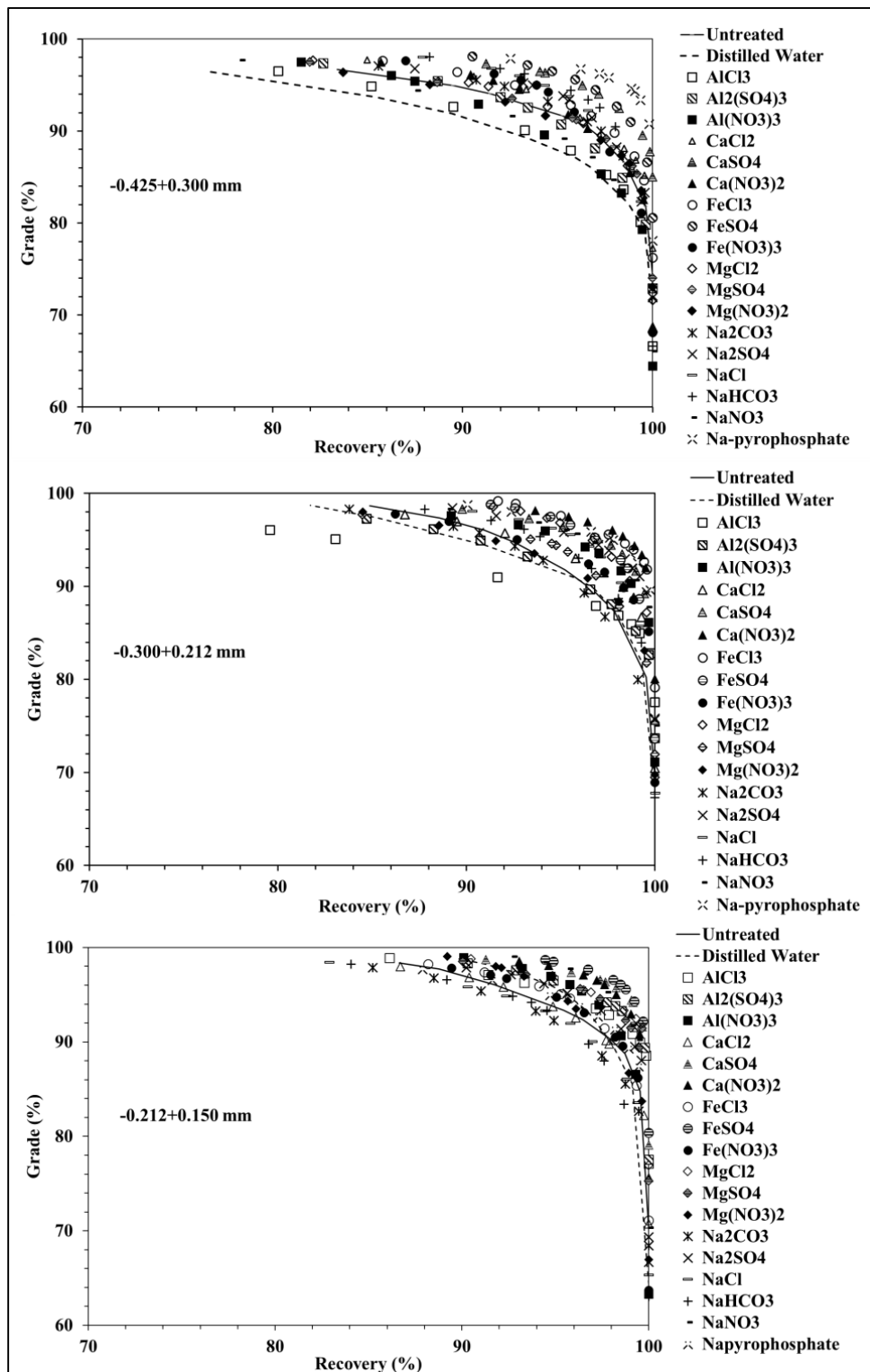
Figure 4.9 Grade-recovery plots of chromite in progeny products of untreated sample and the samples treated in slightly-acidic (pH 6) water at different temperatures
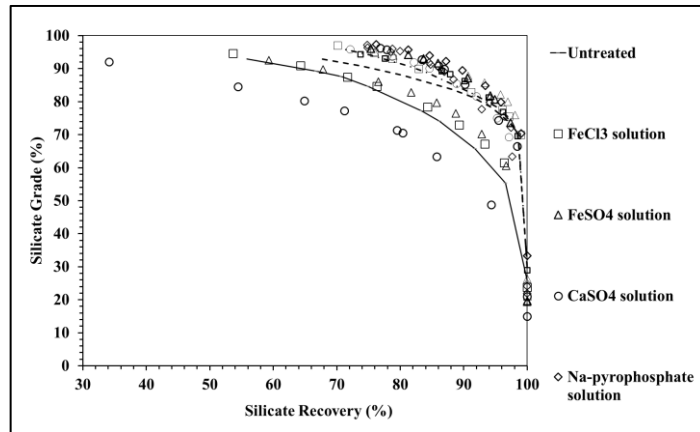

Figure 4.10 Grade-recovery plots of chromite in progeny products of untreated sample (shown by solid and dashed lines) and the samples treated in slightly-acidic (pH 6) water at 30 and 50°C (shown by symbols only).

Figure 4.11a shows the pH and conductivity change in water during pretreatment of sample particles in the slightly-acidic (pH 6) water at different temperatures. The pH and conductivity of water increases while treatment which could be initially attributed to the proton-exchange mechanism releasing Mg ions from the silicate minerals. As shown in Figure 4.11b, the decrease in H^+ concentration does not affect the conductivity of water within a pH range approximately between 5-8.5; therefore, any increase in conductivity should be provided by the dissolved species from the sample particles. The previous studies already show the occurrence of proton-exchange in Mg-silicates even up to an alkaline pH of 8-9 (Oelkers et al., 2009; Pokrovsky and Schott, 2000a), which should have led to the preferential dissolution of Mg^{2+}. However, Figure 4.12 shows that the aqueous concentrations of Mg are lower than Si after pretreatment, which is consistent with the hydrolysis activity rather than proton-exchange mechanism (Section 2.4). Then, this pH might represent a transition range in which proton-exchange and hydrolysis activity occurs simultaneously. In fact, when slightly-acidic water at 30°C and 50°C promotes chromite liberation (Figure 4.9), they are observed to dissolve Si more than Mg by increased hydrolysis activity. On the other hand, when slightly-acidic water at 90°C decreases chromite liberation, dissolution of Mg increases remarkably by increased proton-exchange activity. Then, the above mentioned results suggest that chromite liberation has a positive correlation with the preferential dissolution of Si by hydrolysis. As shown in Figure 3.3, Si concentration is higher at the grain-boundary regions than it is at the bulk texture. Therefore, Si dissolution is expected to occur near to the grain-boundary regions, causing grain-boundary weakening. Figure D.8 and Figure D.9 shows the relative concentrations of elements on particle surfaces after pretreatment in the slightly-acidic water at 30°C and 50°C, respectively, which promote chromite liberation (Figure 4.9). The concentrations of Al, Si and Mg tend to fluctuate at the grain-boundaries, which could be attributed to dissolution and eventually weakening of the grain-boundary surfaces. The dissolution of Si and Mg might be attributed to the hydrolysis activity on silicates; however, it is not known how Al can be dissolved.
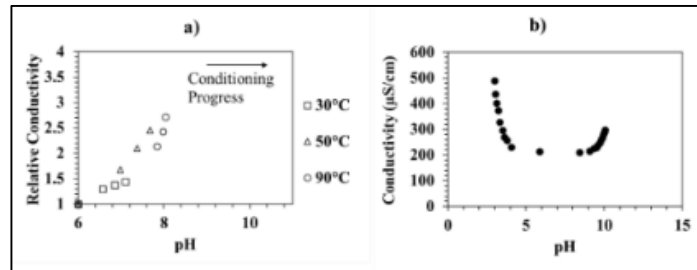
Figure 4.11 (a) pH and relative conductivity change in slightly-acidic (pH 6) water at different temperatures. (b) Conductivity of water as a function of pH only at 50°C.
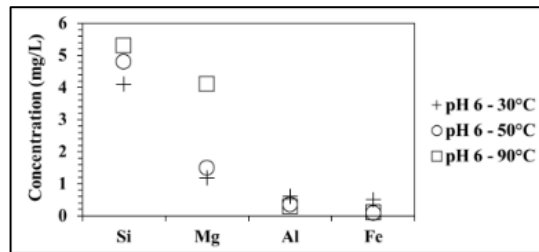
Figure 4.12 Chemical analyses of the slightly-acidic (pH 6) water after treatment at different temperatures

Figure 4.13 shows grade-recovery plots of chromite in progeny particles of the untreated sample and the samples treated in slightly-acidic (pH 6) salt solutions and slightly-acidic water at 50°C. The plots in the coarse progeny classes rise significantly after pretreatment in the slightly-acidic solutions of Na, Fe and Ca salts, which suggests that these salt solutions improve chromite liberation. As shown in Figure 4.14, grade-recovery plots of silicate minerals rise significantly after pretreatment in some of these salt solutions. Therefore, Na, Fe and Ca salts at slightly-acidic pH enhance grain-boundary fracturing. However, as shown in Figure 4.13, the grade-recovery plots of chromite after pretreatment in the slightly-acidic solutions of Mg and Al salts tend to be lower than those of the untreated sample and the sample treated in acidic water. Therefore, Mg and Al salts at slightly-acidic pH are not expected to enhance chromite liberation and grain-boundary fracturing.
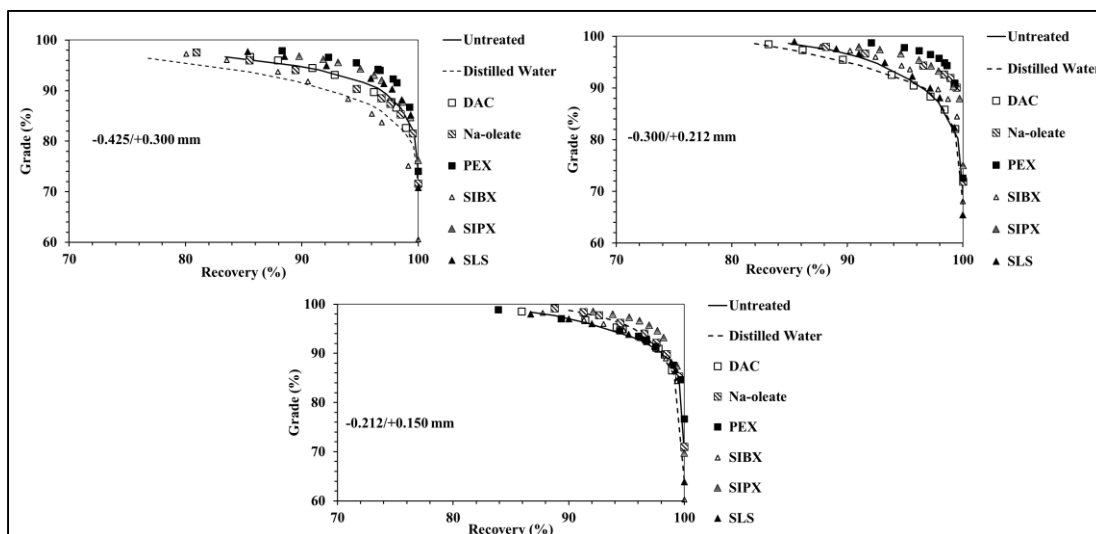
Figure 4.13 Grade-recovery plots of chromite in progeny products of untreated sample and the samples treated in slightly-acidic (pH 6) salt solutions at 50°C.
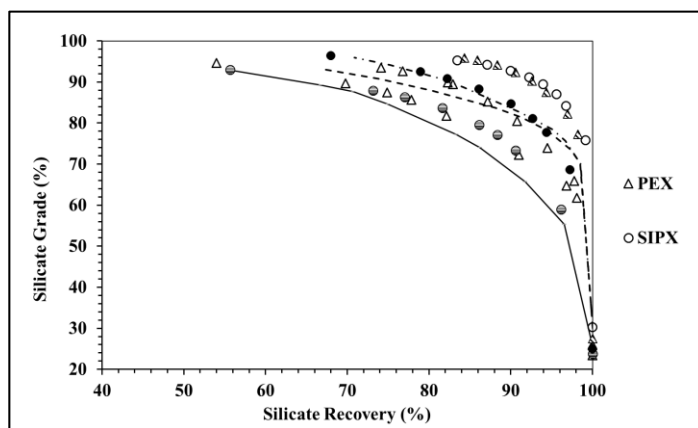
Figure 4.14 Grade-recovery plots of silicate minerals in progeny products of untreated sample (shown by solid and dashed lines) and the samples treated in slightly-acidic (pH 6) solutions of Na, Fe and Ca-salts at 50°C (shown by symbols only).

Table 4.3 shows the change in aqueous concentrations of some cationic or anionic salt species during treatment in some slightly-acidic salt solutions. This table shows that concentrations of some cationic or anionic salt species decrease during treatment, indicating that salt species can generate surface complexes. As pretreatment in slightly-acidic salt solutions and slightly-acidic water can generate different chromite liberation spectra in progeny particles (Figure 4.13), formation of these salt-surface complexes should affect the fracture pattern. Equilibrium diagrams of salt solutions, shown in Appendix B, suggest that the cationic Fe^{3+} and Al^{3+} species should be adsorbed to the surfaces as hydroxylated solid phase, whereas Mg^{2+}, Na^+ and Fe^{2+} can be adsorbed either in their ionic form or compound forms with hydroxyl and other anions. Anionic salt species, on the other hand, can be adsorbed in their ionic forms.

63

Table 4.3 Concentration of cationic and anionic salt components of salts before and after treatment in some of the slightly-acidic (pH 6) salt solutions

Slightly-Acidic Salt Solution	Concentration of Dissolved Cation			Concentration of Dissolved Anion		
	Before Treatment (mg/L)	After Treatment (mg/L)	Error (±)	Before Treatment (mg/L)	After Treatment (mg/L)	Error (±)
$AlCl_3$	2.7	1.18	0.01	* (Cl)	* (Cl)	*
NaCl	2.3	2	0.1	* (Cl)	* (Cl)	*
$FeCl_3$	5.58	0.14	0.01	* (Cl)	* (Cl)	*
$Fe(NO_3)_3$	5.58	0.32	0.01	* (N)	* (N)	*
$FeSO_4$	5.58	0.2	0.01	3.21 (S)	2.9 (S)	0.2
* Unmeasurable by ICP						

Figure D.10 through Figure D.12 show the relative composition of elements on randomly-selected mineral surfaces after pretreatment in the slightly-acidic Na_2CO_3, $FeCl_3$, and $Fe(NO_3)_3$ solutions, respectively, which promote chromite liberation (Figure 4.4). Concentrations of the elements which constitute these salt additives seem to increase at the grain-boundaries, showing that these salt species can adsorb and form surface complexes. Meanwhile, Al concentration which constitute chromite minerals dropped significantly when the salt species adsorb to the grain-boundaries. The above mentioned results suggest that salt solutions will promote chromite liberation when salt-surface complexes at the grain-boundaries dissolve Al-layers. On the other hand, as shown in Figure D.13 and Figure D.14, the solutions of $Al(NO_3)_3$ and $Mg(NO_3)_2$ which hinder chromite liberation do not seem to induce such effect even though NO_3^- might adsorb to the mineral surfaces, which is evident from high N concentration.

Figure 4.15 shows the grade-recovery plots of chromite in progeny classes of untreated sample and sample particles treated in the slightly-acidic (pH 6) surfactant solutions and slightly-acidic water. The plots in coarse progeny sizes shift higher after treatment in the solutions of PEX and Na-oleate, suggesting that these surfactant solutions improve chromite liberation. Figure 4.16 shows that grade-recovery plots of silicate minerals could be improved by PEX and Na-oleate solutions, supporting that these surfactants enhance grain-boundary fracturing. Meanwhile, as shown in Figure 4.15, pretreatment in other anionic surfactants and cationic DAC do not improve grade-recovery plots of chromite; therefore, they are not expected to promote grain-boundary fracturing.
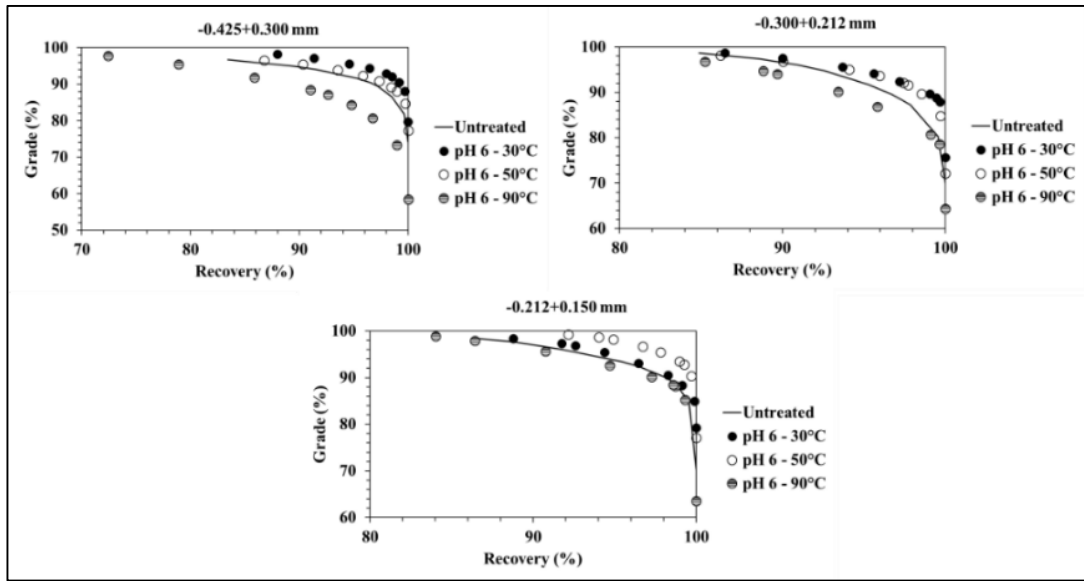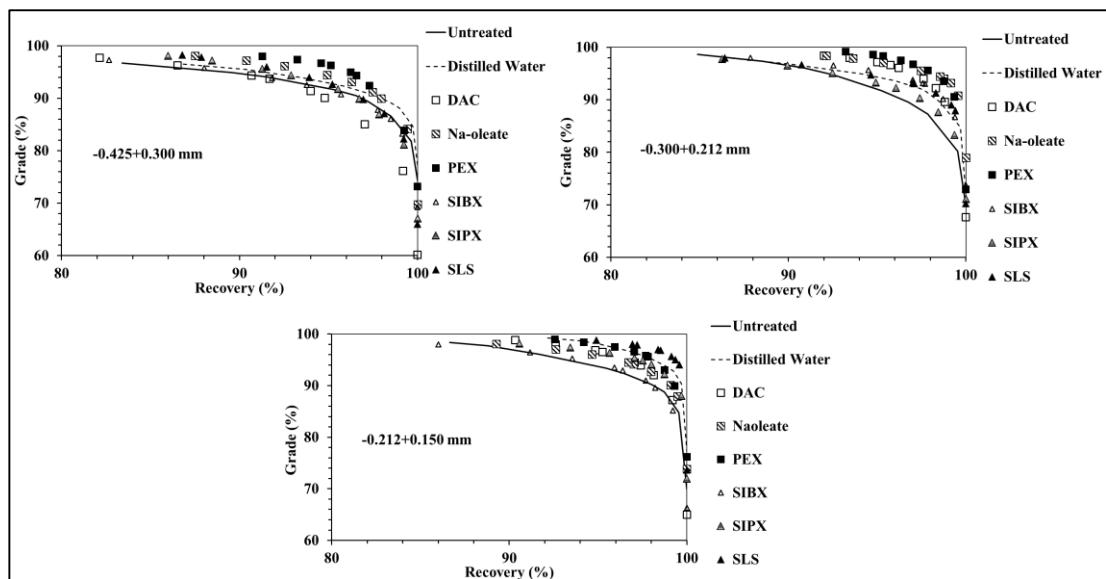

Figure 4.15 Grade-recovery plots of chromite in progeny products of untreated sample and the samples treated in slightly-acidic (pH 6) solutions of surfactants at 50°C.
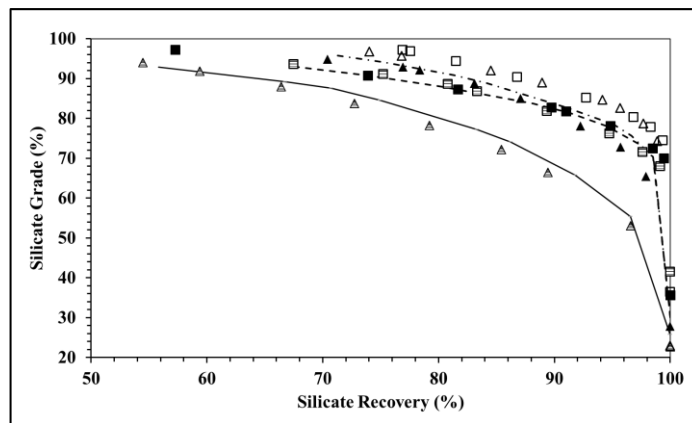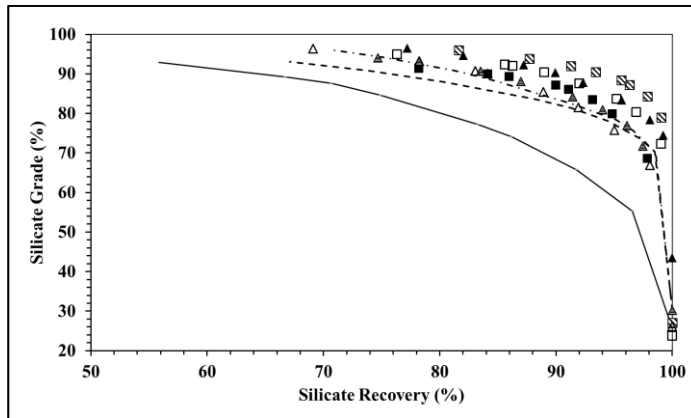
Figure 4.16 Grade-recovery plots of silicate minerals in progeny products of untreated sample (shown by solid and dashed lines) and the samples treated in slightly-acidic (pH 6) solutions of PEX and Na-oleate at 50°C (shown by symbols only).

Table 4.4 shows the aqueous concentration of S before and after treatment in slightly-acidic PEX solution. The decrease in S concentration is associated with adsorption of xanthate species on particle surfaces during treatment, which might enhance grain-boundary weakening. Equilibrium diagram of xanthate solution (Figure 4.8) suggest that xanthate is abundant at slightly-acidic pH; therefore, it is the xanthate ion that should adsorb to the sample surfaces. The relative compositions of particle surfaces after pretreatment in the slightly-acidic PEX solution (Figure D.15) show increased C concentration at the grain boundaries, associated with sharp decreases in Al concentration. This suggests adsorption of xanthate species dissolve chromite mineral at the grain-boundary surface and possibly promote grain-boundary fracturing. On the other hand, as shown in Figure D.16, amine does not alter the grain-boundary structure even if it can be adsorbed to the chromite and grain-boundary which is evident from the increase in C and N concentrations.

Table 4.4 The aqueous concentration of sulfur before and after treatment with slightly-acidic (pH 6) solution of PEX

Component	Before Treatment (mg/L)	After Treatment (mg/L)	Error (±)
S	6.4	0	0.02

4.3. Pretreatment of Samples in Alkaline Water and Alkaline Solutions of Salts and Surfactants

Figure 4.17 shows the grade-recovery plots of chromite in progeny particles of the untreated sample and the samples treated in alkaline (pH 10) water at different temperatures. Samples treated in alkaline water at 50°C and 90°C produce higher plots in progeny particles than ones of untreated sample, suggesting that these conditions yield higher chromite liberation. Besides, as shown in Figure 4.18, alkaline water at 50°C and 90°C improves the grade-recovery plots of silicate minerals in progeny particles. Therefore, these pretreatment conditions are expected to promote grain-boundary fracturing since they improve both chromite and silicate liberation. On the other hand, as shown in Figure 4.17, samples treated in alkaline water at 30°C produces lower grade-recovery plots than those of untreated sample; therefore, this pretreatment condition does not enhance chromite liberation and grain-boundary fracturing.
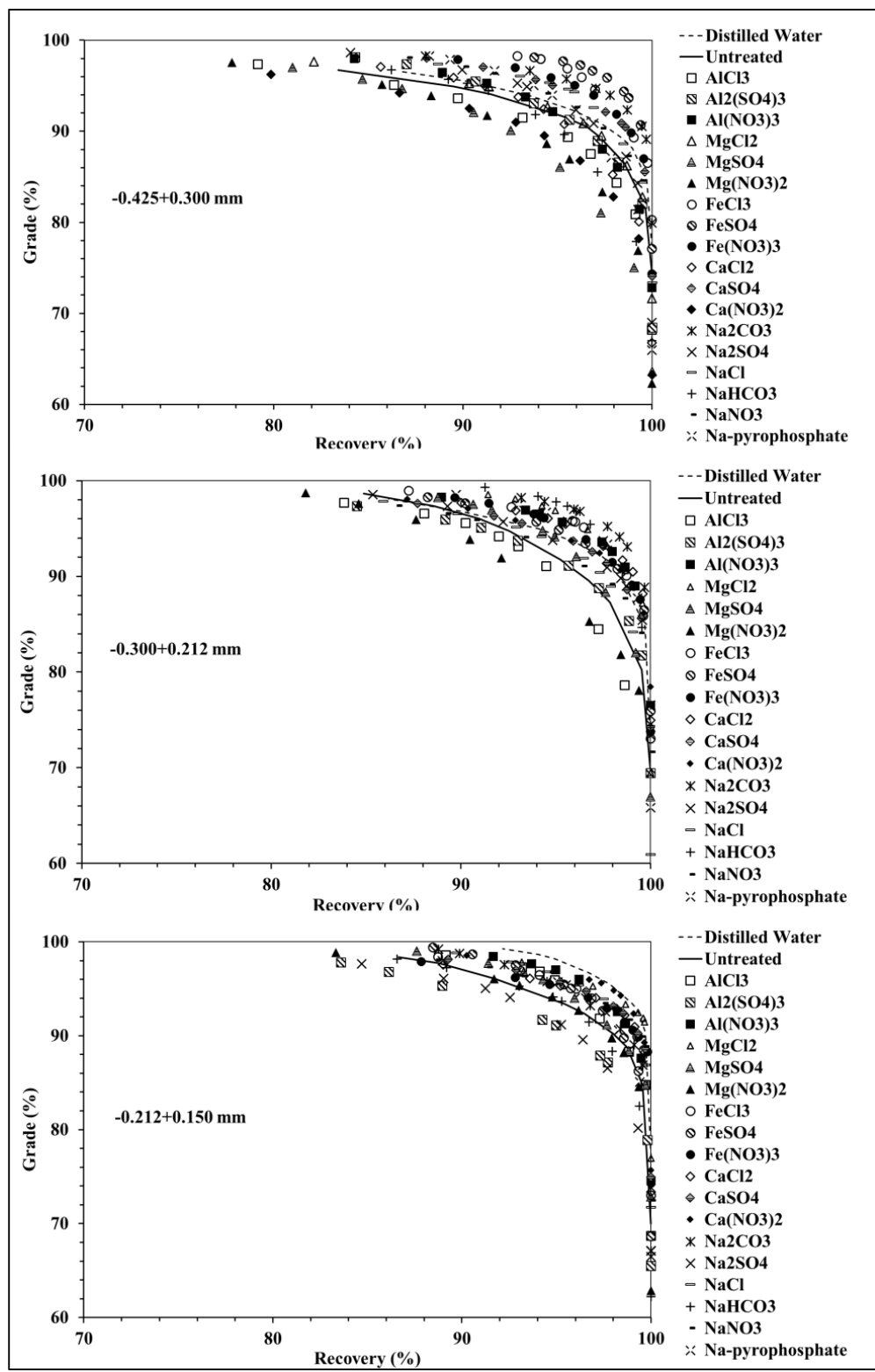
Figure 4.17 Grade-recovery plots of chromite in progeny products of untreated sample and the samples treated in alkaline (pH 10) water at different temperatures.
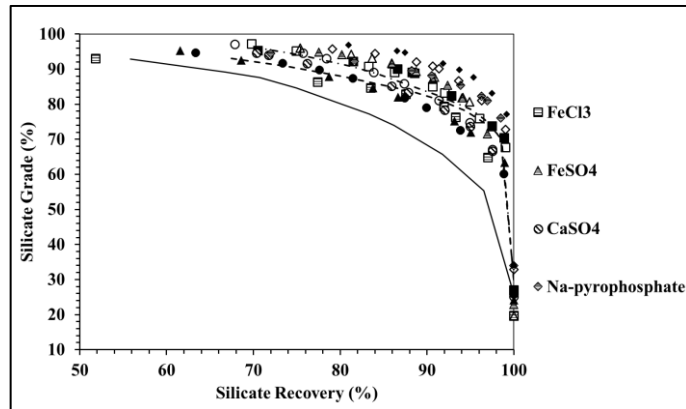

Figure 4.18 Grade-recovery plots of silicate minerals in progeny products of untreated sample (shown by solid and dashed lines) and the samples treated in alkaline (pH 10) water at 50 and 90°C (shown by symbols only).

68

Figure 4.19 shows the pH and conductivity change while pretreatment of sample particles in alkaline water at different temperatures. This figure shows that pH of the water decreases during pretreatment; however, the conductivity increases. The decrease in pH suggests hydrolysis of minerals where OH⁻ ions in water adsorb to the sample surfaces. Meanwhile, increase in the conductivity should be provided by the dissolved sample species because decreasing OH⁻ concentration in alkaline water cannot increase conductivity, as shown in Figure 4.11b. In fact, Figure 4.20 shows that alkaline water mostly contains Si and Mg after treatment, suggesting that hydrolysis dissolves silicate minerals. A common attribute for the hydrolysis of silicates is the preferential dissolution of Si over Mg (Section 2.4), which becomes apparent in alkaline water at 50°C and 90°C. These pretreatment conditions are expected to enhance chromite liberation (Figure 4.17) and grain-boundary weakening, and it might be attributed to the dissolution of Si which is more at the grain-boundary than it is at the bulk (Figure 3.3). However, pretreatment in alkaline water at 30°C dissolves Mg more than Si, which hinders grain-boundary fracturing.
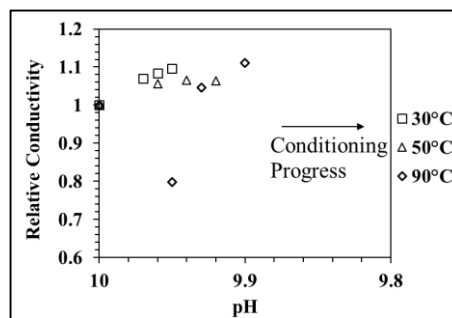
Figure 4.19 pH and relative conductivity change in alkaline (pH 10) water during treatment at different temperatures.
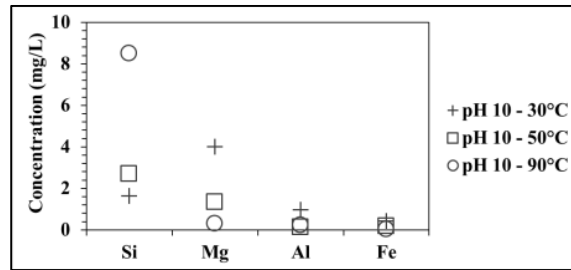
Figure 4.20 Chemical analysis of the alkaline (pH 10) water after treatment at different temperatures

Figure 4.21 shows the grade-recovery plots of chromite in progeny particles of the untreated sample and the samples treated in alkaline salt solutions and alkaline water at 50°C. The plots in the coarse progeny classes rise significantly after pretreatment in most of the alkaline solutions of Na, Fe and Ca salts, which suggests that these salt solutions improve chromite liberation. As shown in Figure 4.22, some of these salt solutions improve grade-recovery plots of silicate minerals. Therefore, salts of Na, Fe and Ca at alkaline pH are expected to promote grain-boundary fracturing. However, as shown in Figure 4.21, the grade-recovery plots of chromite after pretreatment in the alkaline solutions of Mg and Al salts become lower than those of the untreated sample and the sample treated in alkaline water. Then, Mg and Al salts at alkaline pH does not enhance chromite liberation and grain-boundary fracturing.
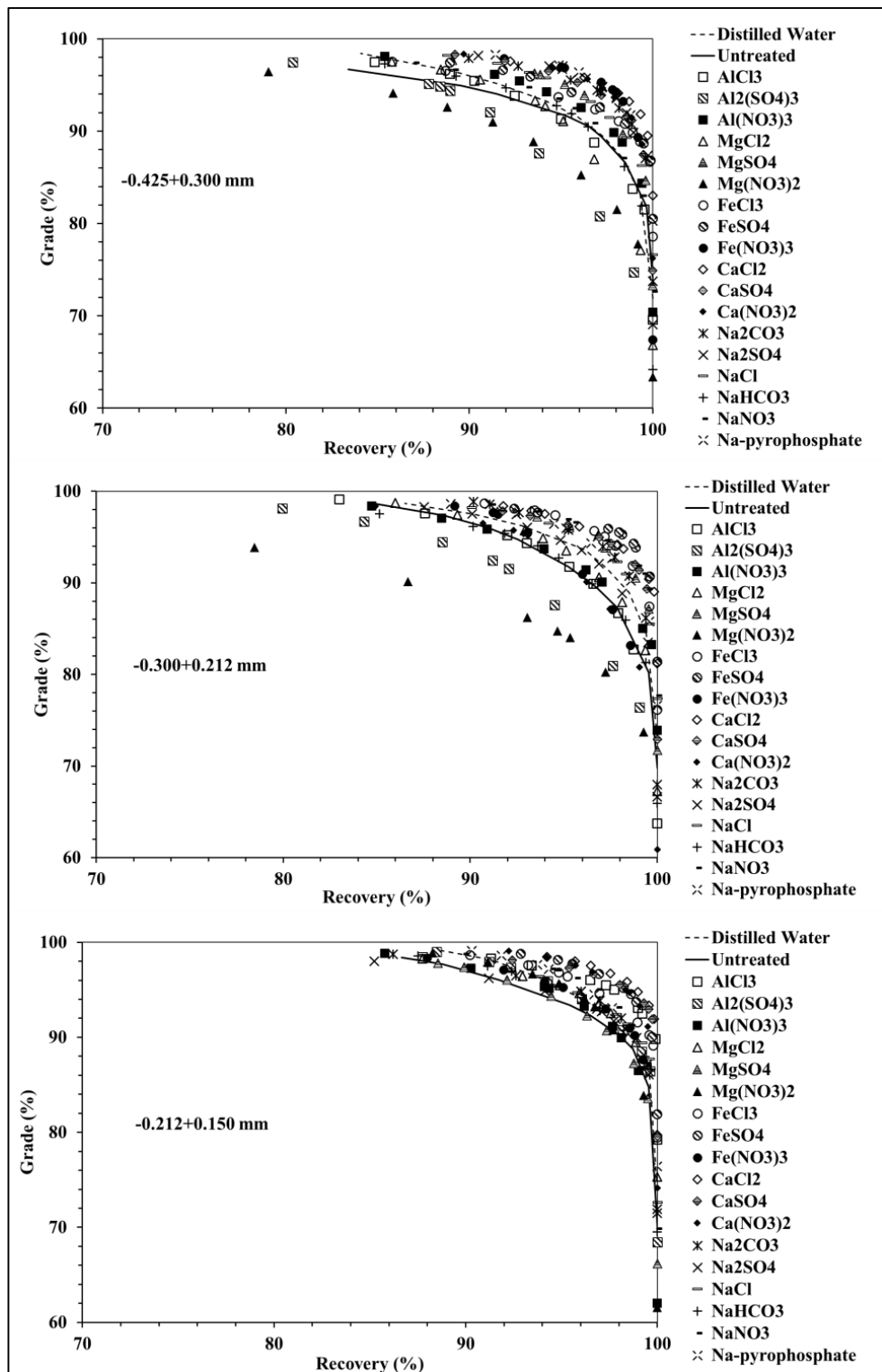
Figure 4.21 Grade-recovery plots of chromite in progeny products of untreated
sample and the samples treated in alkaline (pH 10) salt solutions at 50°C.
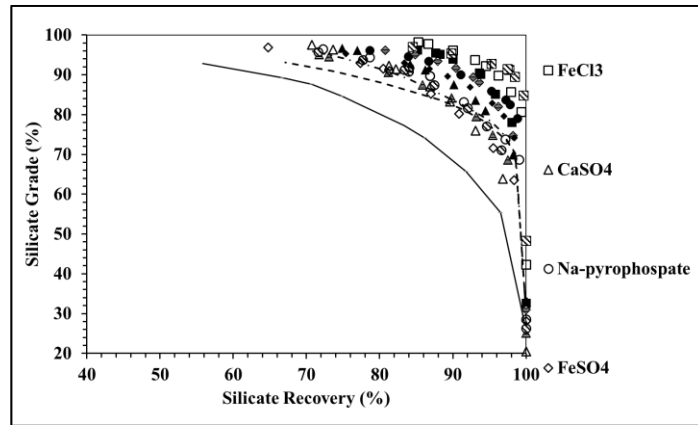
Figure 4.22 Grade-recovery plots of silicate minerals in progeny products of untreated sample (shown by solid and dashed lines) and the samples treated in alkaline (pH 10) solutions of some Na, Fe and Ca-salts at 50°C (shown by symbols only).

Table 4.5 shows the change in the concentrations of the cationic and anionic salt species in alkaline solutions during treatment. The aqueous concentrations of salt components tend to decrease during treatment, supporting that salt species can make surface complexes. As alkaline salt solutions and alkaline water can generate different effect on chromite liberation spectra (Figure 4.21), formation of these salt-surface complexes should affect the fracture pattern. Appendix B shows that even the cationic salt species, except Na^+, which are hydrolyzed to solid phases in alkaline water can make such surface complexes, which is evident from the decrease in the concentration of cationic species from the solution.

Table 4.5 Concentration of cationic and anionic salt components of salts before and after treatment in some of the alkaline (pH 10) salt solutions

Alkaline Salt Solution	Concentration of Cationic Component			Concentration of Anionic Component		
	Before Treatment (mg/L)	After Treatment (mg/L)	Error (±)	Before Treatment (mg/L)	After Treatment (mg/L)	Error (±)
AlCl$_3$	2.7	1.74	0.9	* (Cl)	* (Cl)	*
FeCl$_3$	5.58	0.66	0.01	* (Cl)	* (Cl)	*
CaCl$_2$	4.01	2.1	0.1	* (Cl)	* (Cl)	*
Fe(NO$_3$)$_3$	5.58	0.41	0.1	* (N)	* (N)	*
FeSO$_4$	5.58	0.2	0.02	3.21 (S)	3.1 (S)	0.1
* Unmeasurable by ICP						

Figure D.17 through Figure D.19 show the relative composition of elements on mineral surfaces after pretreatment in the alkaline solutions of CaCl$_2$, FeCl$_3$, FeSO$_4$, respectively, which promote chromite liberation (Figure 4.21). Concentrations of the elements which constitute these salts seem to increase at the grain-boundaries, showing that these salt species can form surface complexes. Meanwhile, such salt-surface complexes are associated with sharp decreases in Al concentration. This suggests that the formation of salt-surface complexes at alkaline pH dissolves Al-layers at the grain-boundaries and promote grain-boundary fracturing. On the other hand, as shown in Figure D.20, alkaline solution of Al$_2$(SO$_4$)$_3$ which is detrimental to chromite liberation (Figure 4.21) does not dissolve any element from the grain-boundary composition although sulfate ions adsorb to the grain-boundary surfaces which is evident from high S concentration at the grain-boundaries.

Figure 4.23 shows the grade-recovery plots of chromite in progeny classes of untreated sample and sample particles treated in the alkaline (pH 10) surfactant solutions and alkaline water. The plots in coarse progeny sizes shift higher after treatment in the alkaline solutions of PEX and SLS, suggesting that these surfactant solutions improve chromite liberation. Figure 4.24 shows that grade-recovery plots of silicate minerals could be improved by PEX and Na-oleate solutions, supporting that these surfactants enhance grain-boundary fracturing. Meanwhile, as shown in Figure 4.23, pretreatment in other alkaline solutions of anionic surfactants and cationic DAC do not improve the grade-recovery plots in coarse progeny classes; therefore, they are not expected to promote grain-boundary fracturing.
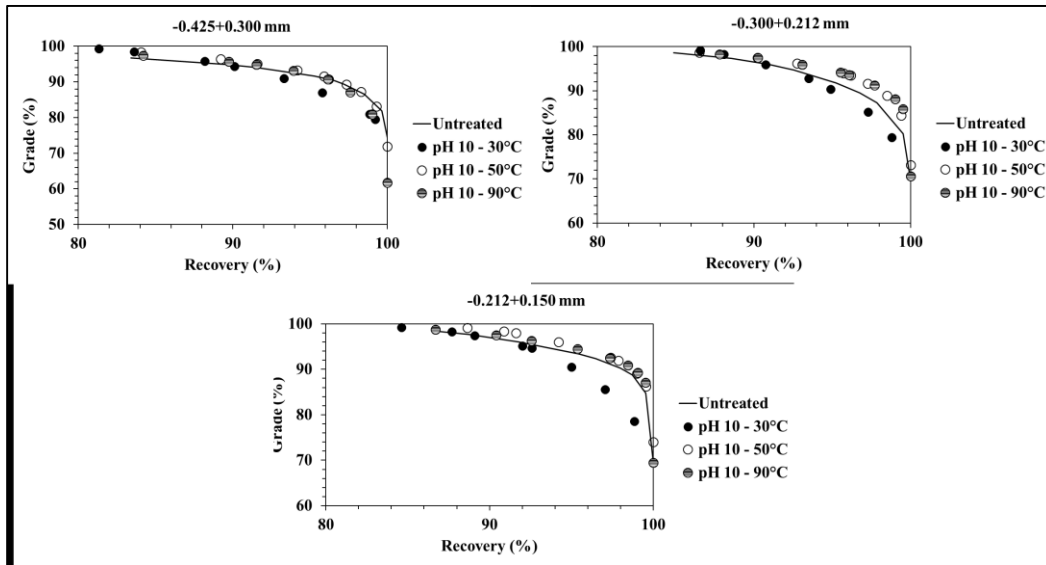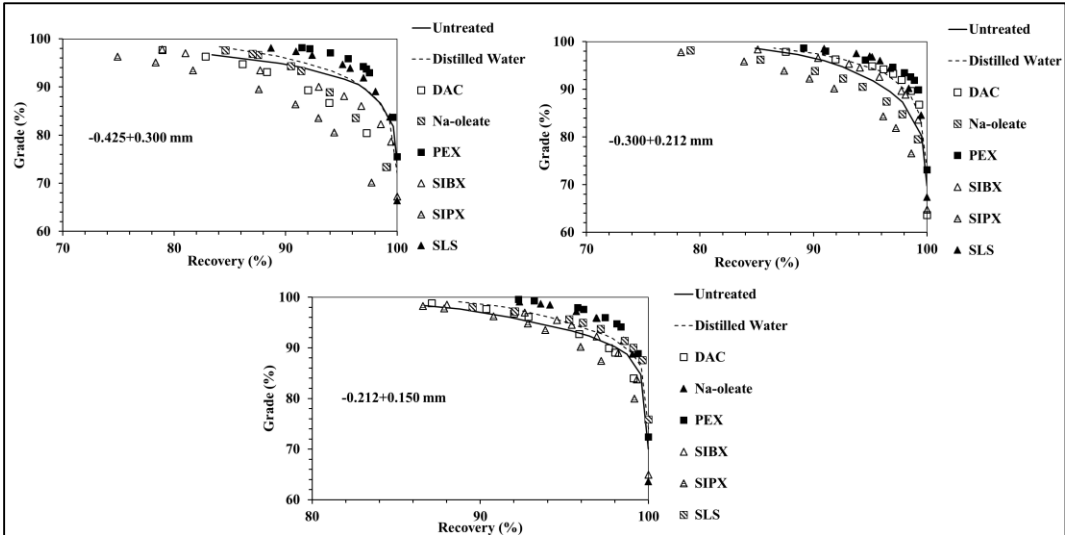

Figure 4.23 Grade-recovery plots of chromite in progeny products of untreated sample and the samples treated in alkaline (pH 10) surfactant solutions and alkaline water at 50°C.
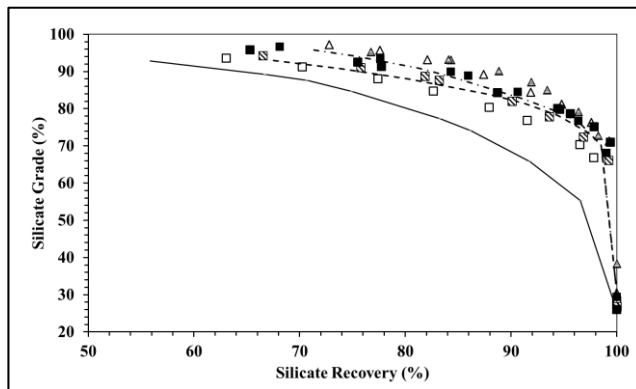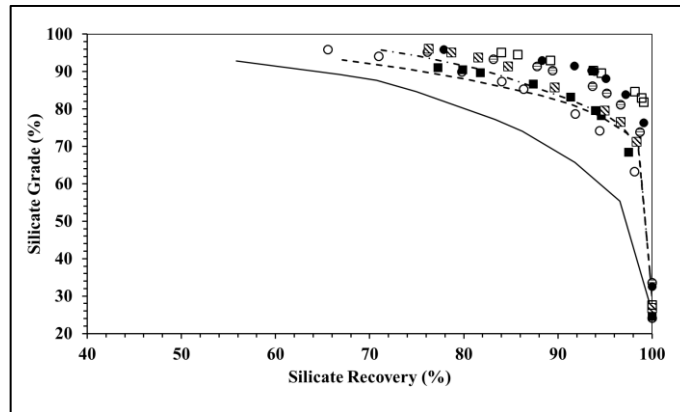
Figure 4.24 Grade-recovery plots of silicate minerals in progeny products of untreated sample (shown by solid and dashed lines) and the samples treated in alkaline (pH 10) solutions of PEX and SIPX at 50°C (shown by symbols only).

Table 4.6 shows changes in the aqueous concentration of S in alkaline solutions of PEX and SLS during treatment. Adsorption of these surfactants is evident from the decrease in S concentration during treatment because sulfur is provided to the solution from the molecular structure of surfactants. Equilibrium diagram of xanthate solution (Figure 4.8) suggest that xanthate ion should be adsorbed to the surfaces in their ionic form. However, there is no information regarding the aqueous species of lauryl sulfate at alkaline pH; therefore, no suggestion can be made on how it is adsorbed to the sample surfaces. Figure D.21 and Figure D.22 shows relative compositions of particle surfaces after pretreatment in the alkaline PEX and SLS solution, respectively. The results show that C concentration at the grain-boundaries increase sharply after pretreatment, indicating adsorption of PEX and SLS. Besides, increased C concentration is associated with sharp decreases in Al concentration, suggesting that formation of such surface complexes weaken the grain-boundaries by dissolving Al-layers.

Table 4.6 The aqueous concentration of sulfur before and after treatment with alkaline (pH 10) PEX and SLS solutions

	PEX			SLS		
Component	Before Treatment (mg/L)	After Treatment (mg/L)	Error (±)	Before Treatment (mg/L)	After Treatment (mg/L)	Error (±)
S	6.4	5	0.4	3.2	2.9	0.2

4.4. Correlation of Grain-Boundary Fracturing to Particle Morphology and Breakage Pattern

Figure E.1 through Figure E.3 show the SE and BSE images of bulk surfaces of progeny particles after pretreatment in $FeCl_3$, $FeSO_4$, and PEX solutions which enhances grain-boundary fracturing. These surfaces include exposed smooth chromite surfaces separated from rough silicate matrix, which should be typical of intergranular breakage (Chanturiya et al., 2011; Charikinya et al., 2015; Guo et al., 2011; Sahoo et al., 2011; Zhong et al., 2017). Figure E.4 and Figure E.5, on the other hand, show the bulk surfaces of progeny particles after pretreatment in $AlCl_3$ and DAC solutions which does not promote chromite liberation. These figures show a rough surface texture, in which chromite is locked with silicate minerals (Figure E.4 and Figure E.5).

Figure 4.25 shows the cumulative progeny size distributions of sample particles after pretreatment in some salt or surfactant solutions which promote grain-boundary fracturing. The size distributions after pretreatment become finer with respect to untreated feed, leading to a steep slope at a coarse size range approximately between 0.425 mm and 2 mm. This size region may actually represent the abnormal jump (Section 2.2) containing liberated chromite grains formed after grain-boundary fracturing. The elemental compositions of progeny particles, shown in Figure 4.26, also suggest enrichment of Cr_2O_3 (or equivalently chromite) within this size range after pretreatment, suggesting higher chromite liberation. On the contrary, Figure 4.27 shows progeny size distributions after pretreatment in some salt or surfactant solutions

which is expected to hinder grain-boundary fracturing. Although the size distributions after pretreatment become finer; they do not promote chromite enrichment in coarser progenies (Figure 4.28).
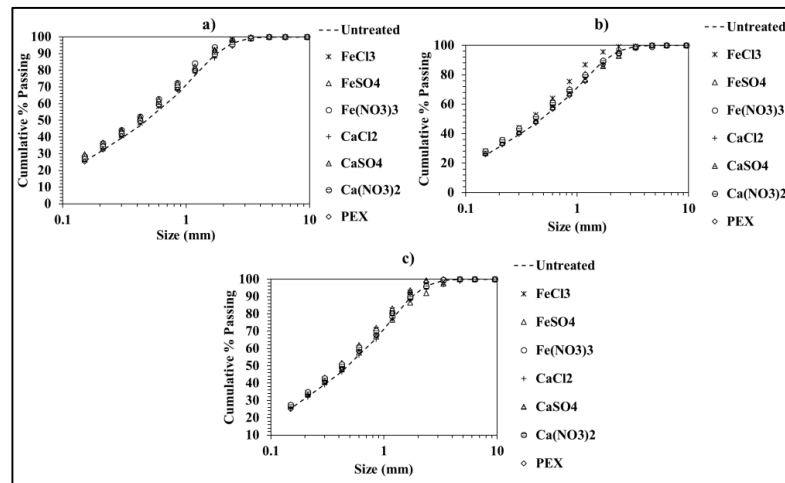
Figure 4.25 Cumulative progeny size distribution of chromite samples treated in acidic (a) slightly-acidic (b) and alkaline (c) salt or surfactant solutions which improved the chromite liberation in progeny particles [Drop-weight energy = 10 J/g]
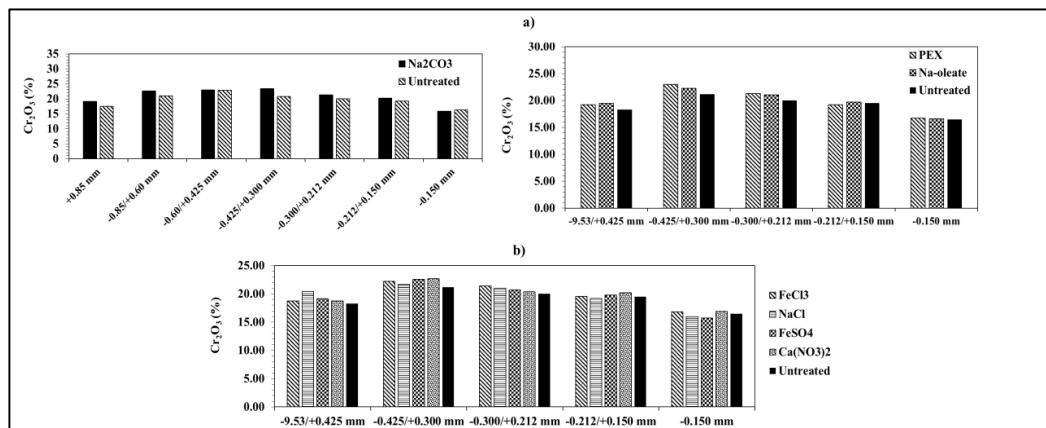
Figure 4.26 Cr_2O_3 (%) grades of the progeny classes of some samples treated in slightly-acidic salt and surfactant solutions (a) and alkaline salt solutions (b) which yielded high liberation
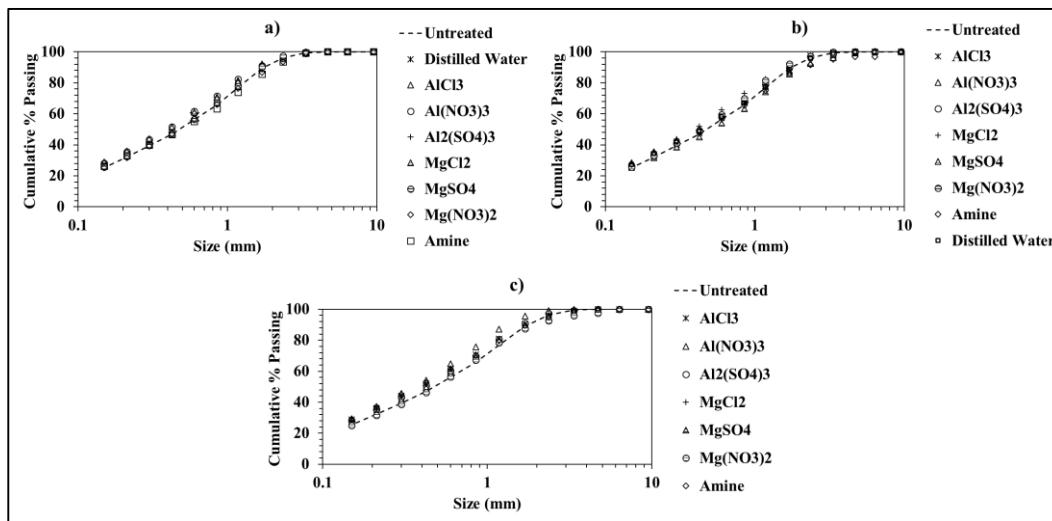
Figure 4.27 Cumulative progeny size distribution of chromite samples treated in acidic (a) slightly-acidic (b) alkaline (c) salt or surfactant solutions which hindered chromite liberation in progeny particles [Drop-weight energy = 10 J/g]
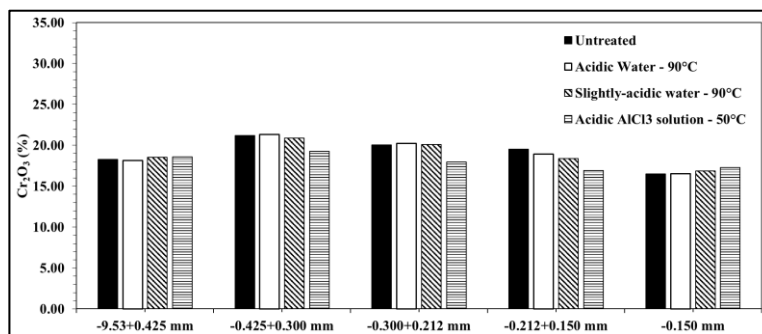
Figure 4.28 Cr_2O_3 (%) grades of the progeny classes of some samples treated in acidic and slightly-acidic salt water at 90°C which yielded poor liberation

It is interesting to note that the change in the progeny size distributions after pretreatment is very slight and even might be statistically-insignificant, although chromite liberation in the progeny sizes may change significantly by the pretreatment. It should be kept in mind that if the Cr_2O_3 (%), or equivalently chromite content in the parent sample is quite low (Table 3.1), the size distributions may be insensitive to

78

grain-boundary detachment (Wen et al., 1998). Furthermore, the adopted specific breakage-energy (10 J/g) somehow yields excessive breakage where the progeny particles may gain an invariant size distribution. Nevertheless, the effect of such treatment on particle breakage pattern is still minute even at lower energy levels, as shown in Figure 4.29.
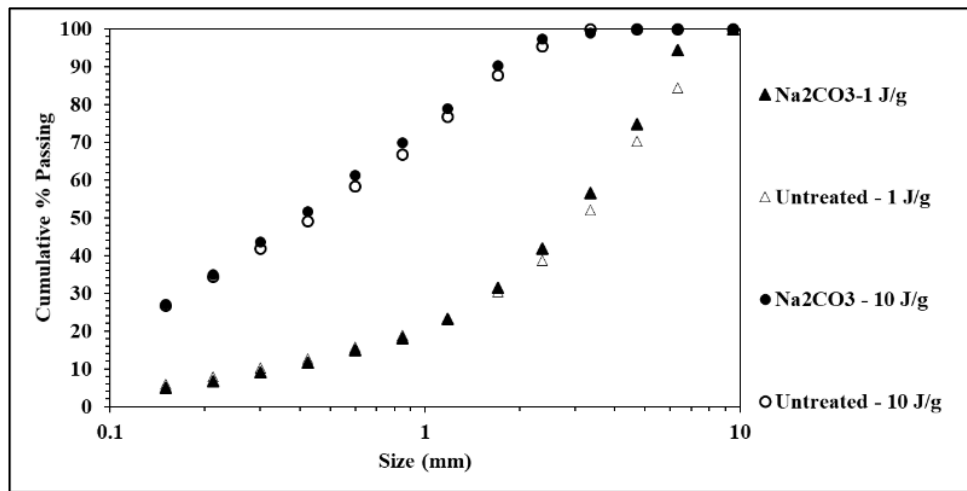
Figure 4.29 Cumulative progeny size distribution of chromite samples treated in slightly-acidic Na_2CO_3 solutions at 50°C, and broken in drop-weight tester at different specific energy levels.

CHAPTER 5

CONCLUSIONS AND RECOMMENDATIONS

Pretreatment of the chromite ore with water is likely to enhance chromite liberation if it dissolves silicate minerals at or near the grain-boundary regions. Si and Mg are accumulated near the grain-boundaries and bulk silicate texture, respectively; therefore, the detachment of Si weakens surfaces near to the grain-boundary region. Then, slightly-acidic or alkaline water will be beneficial for grain-boundary fracturing if it preferentially dissolves Si by hydrolysis. On the contrary, acidic water induces transgranular fracturing as it dissolves Mg by proton-exchange. In fact, surface hydrolysis of silicates is expected to enhance grain-boundary fracturing in any ore type whose gangue minerals are mainly silicate minerals since Si is expected to accumulate near the grain-boundary regions; Further studies are required to validate the promoting effect of surface hydrolysis of silicates on grain-boundary fracturing in various ore types.

Pretreatment of the chromite ore with dilute solutions of Na, Ca and Fe salts enhances grain-boundary weakening and consequently chromite liberation by forming surface complexes and dissolving Al-layers at the grain-boundaries. However, the reasons why these salt-surface complexes dissolve Al-layers are currently unknown. The effect of these salt species on grain-boundary weakening are independent of the pH of the solution. Then, it might be better to use concentrated solutions of Na, Ca, Fe-salts in order to promote their effect on grain-boundary weakening. Further studies are then required to investigate the effect of concentrated salt solutions on grain-boundary weakening and chromite liberation particularly in ball mills.

Adsorption of anionic surfactants are effective to promote grain-boundary fracturing and chromite liberation by adsorbing to the grain-boundaries and dissolving Al-layers. Chromite liberation is promoted by dilute solutions of PEX at all pH values, acidic solution of SIPX, slightly-acidic solution of Na-oleate, and alkaline solution of SLS.

SE and BSE images reveal that the grain-boundary fracturing is associated with exposed chromite grains on the surface. It generates a finer product in which coarse progeny particles are enriched in chromite. However, the change in product fineness is quite minute or even may be statistically-insignificant due to low chromite content in parent particles.

REFERENCES

Agrawal, A.K., Mehra, A., 2016. Olivine dissolution from Indian dunite in saline water. Environ. Sci. Pollut. Res. 23, 22331–22339.

Al-Wakeel, M.I., Lin, C.L., Miller, J.D., 2009. Significance of liberation characteristics in the fatty acid flotation of Florida phosphate rock. Miner. Eng. 22, 244–253.

Ali, A.Y., Bradshaw, S.M., 2011. Confined particle bed breakage of microwave treated and untreated ores. Miner. Eng. 24, 1625–1630.

Alley, D.W., 1999. Performance improvement in the grinding of ceramics via the rebinder effect. University of Connecticut.

Amer, A.M., Ibrahim, I.A., 1996. Leaching of a low grade Egyptian chromite ore. Hydrometallurgy 43, 307–316.

Andres, U., 2010. Development and prospects of mineral liberation by electrical pulses. Int. J. Miner. Process. 97, 31–38.

Andres, U., Bialecki, R., 1986. Liberation of mineral constituents by high-voltage pulses. Powder Technol. 48, 269–277.

Andres, U., Jirestig, J., Timoshkin, I., 1999. Liberation of minerals by high-voltage electrical pulses. Powder Technol. 104, 37–49.

Andres, U., Timoshkin, I., Jirestig, J., Stallknecht, H., 2001. Liberation of valuable inclusions in ores and slags by electrical pulses. Powder Technol. 114, 40–50.

Arganda-Carreras, I., Kaynig, V., Rueden, C., Eliceiri, K.W., Schindelin, J., Cardona, A., Seung, H.S., 2017. Trainable Weka Segmentation: A machine learning tool for microscopy pixel classification. Bioinformatics 33, 2424–2426.

Austin, L.G., Luckie, P.T., 1988. The problems of quantifying mineral liberation: a review. Part. Part. Syst. 5, 122–129.

Babinsky, K., Weidow, J., Knabl, W., Lorich, A., Leitner, H., Primig, S., 2014. Atom probe study of grain boundary segregation in technically pure molybdenum. Mater. Charact. 87, 95–103.

Bartyzel, K., 2016. Adaptive Kuwahara filter. Signal, Image Video Process. 10, 663–670.

Bickmore, B.R., Nagy, K.L., Gray, A.K., Brinkerhoff, A.R., 2006. The effect of Al(OH)4-on the dissolution rate of quartz. Geochim. Cosmochim. Acta 70, 290–305.

Blenkinsop, T.G., Fernandes, T.R.C., 2000. Fractal characterization of particle size distributions in chromitites from the Great Dyke, Zimbabwe. Pure Appl. Geophys. 157, 505–521.

Blum, A., Lasaga, A., 1988. Role of surface speciation in the low-temperature dissolution of minerals. Nature 331, 431–433.

Bradt, R.C., Lin, C.L., Miller, J.D., Chi, G., 1995. Interfacial fracture of multiphase particles and its influence on liberation phenomena. Miner. Eng. 8, 359–366.

Brady, P. V., Walther, J. V., 1989. Controls on silicate dissolution rates in neutral and basic pH solutions at 25C. Geochim. Cosmochim. Acta 53, 2823–2830.

Breiman, L., 2001. Random forests. Mach. Learn. 45, 5–32.

Camalan, M., Çavur, M., Hoşten, Ç., 2017. Assessment of chromite liberation spectrum on microscopic images by means of a supervised image classification. Powder Technol. 322, 214–225.

Carrasco, N., Kretzschmar, R., Pesch, M.L., Kraemer, S.M., 2008. Effects of anionic surfactants on ligand-promoted dissolution of iron and aluminum hydroxides. J. Colloid Interface Sci. 321, 279–287.

Cebeci, Y., Bayat, O., 2004. Effect of flotation reagents on the wet grinding of celestite concantrate. Indian J. Chem. Technol. 11, 382–387.

Celik, I.B., Can, N.M., Sherazadishvili, J., 2010. Influence of process mineralogy on improving metallurgical performance of a flotation plant. Miner. Process. Extr. Metall. Rev. 32, 30–46.

Chanturiya, V. a., Bunin, I.Z., Ryazantseva, M. V., Filippov, L.O., 2011. Theory and Applications of High-Power Nanosecond Pulses to Processing of Mineral Complexes. Miner. Process. Extr. Metall. Rev. 32, 105–136.

Charikinya, E., Bradshaw, S., Becker, M., 2015. Characterising and quantifying microwave induced damage in coarse sphalerite ore particles. Miner. Eng. 82,

14–24.

Choi, H., Lee, W., Kim, D.U., Kumar, S., Kim, S.S., Chung, H.S., Kim, J.H., Ahn, Y.C., 2010. Effect of grinding aids on the grinding energy consumed during grinding of calcite in a stirred ball mill. Miner. Eng. 23, 54–57.

Choi, H., Lee, W., Kim, S., 2009. Effect of grinding aids on the kinetics of fine grinding energy consumed of calcite powders by a stirred ball mill. Adv. Powder Technol. 20, 350–354.

Chou, L., Wollast, R., 1984. Study of the weathering of albite at room temperature and pressure with a fluidized bed reactor. Geochim. Cosmochim. Acta 48, 2205–2217.

Christiansen, F.G., 1986. Deformation of chromite: S.E.M. investigations. Tectonophysics 121, 175–196.

Craig, J.R., Vaughan, D.J., 1994. Ore microscopy and ore petrography, 2nd ed. John Wiley & Sons, New York.

Crundwell, F.K., 2014. The mechanism of dissolution of minerals in acidic and alkaline solutions: Part II Application of a new theory to silicates, aluminosilicates and quartz. Hydrometallurgy 149, 265–275.

Daval, D., Hellmann, R., Martinez, I., Gangloff, S., Guyot, F., 2013. Lizardite serpentine dissolution kinetics as a function of pH and temperature, including effects of elevated pCO2. Chem. Geol. 351, 245–256.

Delbem, I.D., Galéry, R., Brandão, P.R.G., Peres, A.E.C., 2015. Semi-automated iron ore characterisation based on optical microscope analysis: Quartz/resin classification. Miner. Eng. 82, 2–13.

Donskoi, E., Suthers, S.P., Fradd, S.B., Young, J.M., Campbell, J.J., Raynlyn, T.D., Clout, J.M.F., 2007. Utilization of optical image analysis and automatic texture classification for iron ore particle characterisation. Miner. Eng. 20, 461–471.

El-Shall, H., 1980. Effect of chemical additives on grinding. Colombia University.

El-Shall, H., Somasundaran, P., 1984a. Physico-chemical aspects of grinding: a review of use of additives. Powder Technol. 38, 275–293.

El-Shall, H., Somasundaran, P., 1984b. Mechanisms of grinding modification by chemical additives: organic reagents. Powder Technol. 38, 267–273.

Eriksson, G., 1979. An algorithm for the computation of aqueous multi-component, multiphase equilibria. Anal. Chim. Acta 112, 375–383.

Fandrich, R., Gu, Y., Burrows, D., Moeller, K., 2007. Modern SEM-based mineral liberation analysis. Int. J. Miner. Process. 84, 310–320.

Feng, D., Aldrich, C., 2004. Recovery of chromite fines from wastewater streams by column flotation. Hydrometallurgy 72, 319–325.

Flaathen, T.K., Gislason, S.R., Oelkers, E.H., 2010. The effect of aqueous sulphate on basaltic glass dissolution rates. Chem. Geol. 277, 345–354.

Fuchs, Y., Linares, J., Mellini, M., 1998. Mössbauer and infrared spectrometry of lizardite- 1T from Monte Fico , Elba. Phys. Chem. Miner. 26, 111–115.

Fuerstenau, D.W., 1995. Grinding aids. KONA Powder Part. J. 13, 5–18.

Fuerstenau, M.C., 1995. Oxide and Silicate Flotation, in: Matis, K.A. (Ed.), Flotation Science and Engineering. CRC Press, New York, pp. 89–126.

Gallios, G.P., Deliyanni, E.A., Peleka, E.N., Matis, K.A., 2007. Flotation of chromite and serpentine. Sep. Purif. Technol. 55, 232–237.

Gaudin, A.M., 1939. Liberation, in: Principles of Mineral Dressing. McGraw-Hill Book Company, Inc., New York, pp. 70–91.

Gay, S.L., 2004. A liberation model for comminution based on probability theory. Miner. Eng. 17, 525–534. doi:10.1016/j.mineng.2003.11.012

Geveci, A., Topkaya, Y., Ayhan, E., 2002. Sulfuric acid leaching of Turkish chromite concentrate. Miner. Eng. 15, 885–888.

Gräbner, M., Lester, E., 2016. Proximate and ultimate analysis correction for kaolinite-rich Chinese coals using mineral liberation analysis. Fuel 186, 190–198.

Gu, Y., 2003. Automated scanning electron microscope based mineral liberation analysis. J. Miner. Mater. Charact. Eng. 2, 33–41.

Guo, S.H., Chen, G., Peng, J.H., Chen, J., Li, D.B., Liu, L.J., 2011. Microwave assisted grinding of ilmenite ore. Trans. Nonferrous Met. Soc. China (English Ed. 21, 2122–2126.

Gyollai, I., Krebsz, M., Kereszturi, Á., Bérczi, S., Gucsik, A., 2014. FTIR-ATR Spectroscopy of shock vein in Mócs L6 chondrite, in: Modern Analytical Methods I.

Haecker, R.W., 1984. Survey of environmental effects on rock disintegration processes. Montana College of Mineral Science and Technology.

Hammond, M.., Ravitz, S.F., 1963. Influence of environment on brittle fracture of silica. J. Am. Ceram. Soc. 46, 329–332.

Hasegawa, M., Kimata, M., Shimane, M., Shoji, T., Tsuruta, M., 2001. The effect of liquid additives on dry ultrafine grinding of quartz. Powder Technol. 114, 145–151.

Heller-Kallai, L., Yariv, S., Gross, S., 1975. Hydroxyl-stretching frequencies of serpentine minerals. Mineral. Mag. 40, 197–200.

Hondros, E.D., Seah, M.P., Hofmann, S., 1996. Interfacial and surface microchemistry, in: Cahn, R.W., Haasen, P. (Eds.), Physical Metallurgy. Elsevier B.V., pp. 1201–1289.

Hsih, C.S., Wen, S.B., Kuan, C.C., 1995. An exposure model for valuable components in comminuted particles. Int. J. Miner. Process. 43, 145–165.

Huang, J.J., Siu, W.C., Liu, T.R., 2015. Fast image interpolation via random forests. IEEE Trans Image Process 24, 3232–3245.

Huang, W.H., Keller, W.D., 1970. Dissolution of rock-forming silicate minerals in organic acids : simulated first-stage weathering of fresh mineral surfaces. Am. Mineral. 55, 2076–2094.

Hunt, J., Berry, R., Bradshaw, D., 2011. Characterising chalcopyrite liberation and flotation potential: Examples from an IOCG deposit. Miner. Eng. 24, 1271–1276.

Hunt, J., Berry, R., Walters, S., 2010. Using mineral maps to rank potential processing behaviour, in: 25th International Mineral Processing Congress. Australasian Institute of Mining and Metallurgy, Brisbane, pp. 2899–2905.

Icenhower, J.P., Dove, P.M., 2000. The dissolution kinetics of amorphous silica into sodium chloride solutions: Effects of temperature and ionic strength. Geochim. Cosmochim. Acta 64, 4193–4203.

Ingri, N., Kakolowicz, W., Sillén, L.G., Warnqvist, B., 1967. High-speed computers as a supplement to graphical methods—V*Haltafall, a general program for calculating the composition of equilibrium mixtures. Talanta 14, 1261–1286.

Jones, R.H., 2007. Environment induced crack growth of ceramics and glasses, in:

Shipilov, S.A., Jones, R.H., Olive, J.-M., Rebak, R.B. (Eds.), Environment-Induced Cracking of Materials. Elsevier, Amsterdam, pp. 449–466.

Jones, R.H., Baer, D.R., Danielson, M.J., Vetrano, J.S., 2001. Role of Mg in the stress corrosion cracking of an Al-Mg alloy. Metall. Mater. Trans. A 32A, 1699–1711.

Kaplan Can, H., Şahin, Ö., 2015. Design, synthesis and characterization of 3,4-dihydro-2H-pyran containing copolymer/clay nanocomposites. J. Macromol. Sci. Part A Pure Appl. Chem. 52, 465–475.

Katzer, M., Klimpel, R.R., Sewell, J., 1981. Example of the laboratory characterization of grinding aids in the wet grinding of ores. Min. Eng. 1471–1476.

Khisina, N.R., Wirth, R., Andrut, M., Ukhanov, A. V., 2001. Extrinsic and intrinsic mode of hydrogen occurence in natural olivines: FTIR and TEM investigation. Phys. Chem. Miner. 28, 291–301.

Khorram, F., Memarian, H., Tokhmechi, B., 2011. Limestone chemical components estimation using image processing and pattern recognition techniques. J. Min. Environ. 2, 126–135.

King, R.P., 2001. Comminution operations, in: Modeling and Simulation of Mineral Processing Systems. Butterworth-Heinmann Publications, Oxford, pp. 127–210.

King, R.P., 1979. A model for the quantitative estimation of mineral liberation by grinding. Int. J. Miner. Process. 6, 207–2207.

Kingman, S.W., Jackson, K., Cumbane, A., Bradshaw, S.M., Rowson, N.A., Greenwood, R., 2004. Recent developments in microwave-assisted comminution. Int. J. Miner. Process. 74, 71–83.

Kingman, S.W., Vorster, W., Rowson, N.A., 2000. The influence of mineralogy on microwave asssted grinding. Miner. Eng. 13, 313–327.

Klimpel, R.R., Austin, L.G., 1983. A preliminary model of liberation from a binary system. Powder Technol. 34, 121–130.

Klimpel, R.R., Austin, L.G., 1982. Chemical additives of wet grinding of minerals. Powder Technol. 31, 239–253.

Klimpel, R.R., Manfroy, W., 1978. Chemical grinding aids for increasing throughput in the wet grinding of ores. Ind. Eng. Chem. Process Des. Dev. 17, 518–523.

Klimpel, R.R., Manfroy, W., 1978. Chemical Grinding Aids for Increasing

Throughput in the Wet Grinding of Ores. Ind. Eng. Chem. Process Des. Dev. 17, 518–523.

Köse, C., Alp, İ., İkibaş, C., 2012. Statistical methods for segmentation and quantification of minerals in ore microscopy. Miner. Eng. 30, 19–32.

Lacinska, A.M., Styles, M.T., Bateman, K., Wagner, D., Hall, M.R., Gowing, C., Brown, P.D., 2016. Acid-dissolution of antigorite, chrysotile and lizardite for ex situ carbon capture and storage by mineralisation. Chem. Geol. 437, 153–169.

Lane, G.R., Martin, C., Pirard, E., 2008. Techniques and applications for predictive metallurgy and ore characterization using optical image analysis. Miner. Eng. 21, 568–577.

Lätti, D., Adair, B.J.I., 2001. An assessment of stereological adjustment procedures. Miner. Eng. 14, 1579–1587.

Leigh, G.M., Lyman, G.J., Gottlieb, P., 1996. Stereological estimates of liberation from mineral section measurements: A rederivation of Barbery's formulae with extensions. Powder Technol. 87, 141–152.

Leißner, T., Hoang, D.H., Rudolph, M., Heinig, T., Bachmann, K., Gutzmer, J., Schubert, H., Peuker, U.A., 2016. A mineral liberation study of grain boundary fracture based on measurements of the surface exposure after milling. Int. J. Miner. Process. 156, 3–13.

Leißner, T., Mütze, T., Bachmann, K., Rode, S., Gutzmer, J., Peuker, U.A., 2013. Evaluation of mineral processing by assessment of liberation and upgrading. Miner. Eng. 53, 171–173.

Lin, C.L., Miller, J.D., 1996. Cone beam X-ray microtomography for three-dimensional liberation analysis in the 21st century. Int. J. Miner. Process. 47, 61–73.

Lin, F.C., Clemency, C. V., 1981. The dissolution kinetics of brucite, antigorite, talc, and phlogopite at room temperature and pressure. Am. Mineral. 66, 801–806.

Lin, I.J., Mitzmager, A., 1968. The influence of the environment on the comminution of quartz. Trans. AIME 241, 412–418.

Lind, R., 2012. Open source software for image processing and analysis: picture this with ImageJ, in: Harland, L., Forster, M. (Eds.), Open Source Software in Life

Science Research. Woodhead Publishing Limited, pp. 131–149.

Liu, Y., Olsen, A.A., Rimstidt, J.D., 2006. Mechanism for the dissolution of olivine series minerals in acidic solutions. Am. Mineral. 91, 455–458.

Locher, F.W., Von Seebach, H.M., 1972. Influence of adsorption on industrial grinding. Ind. Eng. Chem. Process Des. Dev. 11.

Lotter, N.O., Kormos, L.J., Oliveira, J., Fragomeni, D., Whiteman, E., 2011. Modern process mineralogy: Two case studies. Miner. Eng. 24, 638–650.

Lumpkin, G.R., 2001. Crystal chemistry and durability of the spinel structure type in natural systems. Prog. Nucl. Energy 38, 447–454.

Lund, C., Lamberg, P., Lindberg, T., 2015. Development of a geometallurgical framework to quantify mineral textures for process prediction. Miner. Eng. 82, 61–77.

Lyman, G.J., 1995. Method for interpolation of 2-D histogram data: application to mineral liberation data. Powder Technol. 83, 133–138.

Lynch, S.P., 2007. Towards understanding mechanisms and kinetics of environmentally assisted cracking, in: Shipilov, S.A., Jones, R.H., Olive, J.-M., Rebak, R.B. (Eds.), Environment-Induced Cracking of Materials. Elsevier, Amsterdam, pp. 167–177.

Lynch, S.P., Moutsos, S., 2006. A brief history of fractography. J. Fail. Anal. Prev. 6, 54–69.

Maiti, K., Sil, A., 2010. Relationship between fracture toughness characteristics and morphology of sintered Al2O3 ceramics. Ceram. Int. 36, 2337–2344.

Makokha, A.B., Moys, M.H., Bwalya, M.M., 2011. Modeling the RTD of an industrial overflow ball mill as a function of load volume and slurry concentration. Miner. Eng. 24, 335–340.

Makreski, P., Jovanovski, G., Stojančeska, S., 2005. Minerals from Macedonia XIII: Vibrational spectra of some commonly appearing nesosilicate minerals. J. Mol. Struct. 744–747, 79–92.

Mariano, R.A., 2016. Measurement and Modelling of the Liberation and Distribution of Minerals in Comminuted Ores. The University of Queensland.

Mariano, R.A., Evans, C.L., Manlapig, E., 2016. Definition of random and non-

random breakage in mineral liberation - A review. Miner. Eng. 94, 51–60.

Marincea, Ş., 2001. New data on Szaibelyite from the type locality, Baita Bihor, Romania. Can. Mineral. 39, 111–127.

McMahon Jr., C.J., 2001. Hydrogen-induced intergranular fracture of steels. Eng. Fract. Mech. 68, 773–788.

Medina, J.F., 2012. Liberation-limited grade/recovery curves for auriferous pyrite ores as determined by high resolution x-ray microtomography. The University of Utah.

Mellini, M., Fuchs, Y., Viti, C., Lemaire, C., Linarès, J., 2002. Insights into the antigorite structure from Mössbauer and FTIR spectroscopies. Eur. J. Mineral. 14, 97–104.

Meloy, T.P., Gotoh, K., 1985. Liberation in a homogenous two-phase ore. Int. J. Miner. Process. 14, 45–55.

Metha, R.K., Adel, G.T., Yoon, R.H., 1989. Liberation modeling and parameter estimation for multicomponent mineral systems. Powder Technol. 58, 195–209.

Miller, G.H., Rossman, G.R., Harlow, G.E., 1987. The natural occurrence of hydroxide in olivine. Phys. Chem. Miner. 14, 461–472.

Minnis, M.M., 1984. An automatic point-counting method for mineralogical assessment. Am. Assoc. Pet. Geol. Bull. 68:744-752, 744–752.

Mogollón, J.L., Pérez-Diaz, A., Lo Monaco, S., 2000. The effects of ion identity and ionic strength on the dissolution rate of a gibbsitic bauxite. Geochim. Cosmochim. Acta 64, 781–795.

Moorthy, V.K., Tooley, F. V, 1951. Effect of certain organic liquids on strength of glass 21.

Morris, P.M., Wogelius, R.A., 2008. Phthalic acid complexation and the dissolution of forsteritic glass studied via in situ FTIR and X-ray scattering. Geochim. Cosmochim. Acta 72, 1970–1985.

Nagao, A., Smith, C.D., Dadfarnia, M., Sofronis, P., Robertson, I.M., 2012. The role of hydrogen in hydrogen embrittlement fracture of lath martensitic steel. Acta Mater. 60, 5182–5189.

Oelkers, E.H., 2001. An experimental study of forsterite dissolution rates as a function

of temperature and aqueous Mg and Si concentrations. Chem. Geol. 175, 485–494.

Oelkers, E.H., Golubev, S. V., Chairat, C., Pokrovsky, O.S., Schott, J., 2009. The surface chemistry of multi-oxide silicates. Geochim. Cosmochim. Acta 73, 4617–4634.

Olsen, A.A., 2007. Forsterite dissolution kinetics: Applications and implications for chemical weathering. Virginia Polytechnic Institute and State University.

Olsen, A.A., Donald Rimstidt, J., 2008. Oxalate-promoted forsterite dissolution at low pH. Geochim. Cosmochim. Acta 72, 1758–1766.

Orowan, E., 1949. Fracture and strength of solids. Reports Prog. Phys. 12, 185–232.

Ozcan, O., Benzer, H., 2013. Comparison of different breakage mechanisms in terms of product particle size distribution and mineral liberation. Miner. Eng. 49, 103–108.

Parian, M., Lamberg, P., Möckel, R., Rosenkranz, J., 2015. Analysis of mineral grades for geometallurgy: Combined element-to-mineral conversion and quantitative X-ray diffraction. Miner. Eng. 82, 25–35.

Parirenyatwa, S., Escudero-Castejon, L., Sanchez-Segado, S., Hara, Y., Jha, A., 2016. Comparative study of alkali roasting and leaching of chromite ores and titaniferous minerals. Hydrometallurgy 165, 213–226.

Parker, T., Shi, F., Evans, C., Powell, M., 2015. The effects of electrical comminution on the mineral liberation and surface chemistry of a porphyry copper ore. Miner. Eng.

Parks, G.A., 1984. Surface and interfacial free energies of quartz. J. Geophys. Res. 89, 3997–4008.

Pascoe, R.D., Power, M.R., Simpson, B., 2007. QEMSCAN analysis as a tool for improved understanding of gravity separator performance. Miner. Eng. 20, 487–495.

Peck, L., 1982. Stress corrosion and crack propagation in sioux quartzite. Yale University.

Petruk, W., 2000. Applied Mineralogy in the Mining Industry, 1st ed. Elsevier, Ottawa.

Philander, C., Rozendaal, A., 2013. The application of a novel geometallurgical

template model to characterise the Namakwa Sands heavy mineral deposit, West Coast of South Africa. Miner. Eng. 52, 82–94.

Pirard, E., Lebichot, S., Krier, W., 2007. Particle texture analysis using polarized light imaging and grey level intercepts. Int. J. Miner. Process. 84, 299–309.

Pokrovsky, O.S., Schott, J., 2000a. Kinetics and mechanism of forsterite dissolution at 25°C and pH from 1 to 12. Geochim. Cosmochim. Acta 64, 3313–3325.

Pokrovsky, O.S., Schott, J., 2000b. Forsterite surface composition in aqueous solutions: A combined potentiometric, electrokinetic, and spectroscopic approach. Geochim. Cosmochim. Acta 64, 3299–3312.

Povnnennykh, A.S., 1978. The use of infrared spectra for the determination of minerals. Am. Mineral. 63, 956–959.

Reddy, B.J., Frost, R.L., 2005. Spectroscopic characterization of chromite from the Moa-Baracoa Ophiolitic Massif, Cuba. Spectrochim. Acta - Part A Mol. Biomol. Spectrosc. 61, 1721–1728.

Rehbinder, P.A., 1931. Physik 72, 191.

Rehbinder, P.A., 1928. in: VI S''ezd Russkikh Fizikov (VI Congress of Russian Physicists). OGIZ, Moscow, p. 29.

Rehbinder, P.A., Kalinkovaskaya, 1932. J.Tech. Phys 2, 726–755.

Rice, R.W., 1997. Review: Effects of environment and temperature on ceramic tensile strength – grain size relations. J. Mater. Sci. 32, 3071–3087.

Ridley, M.K., Wesolowski, D.J., Palmer, D.A., Bénézeth, P., Kettler, R.M., 1997. Effect of sulfate on the release rate of Al3+ from gibbsite in low- temperature acidic waters. Environ. Sci. Technol. 31, 1922–1925.

Roberts, C., Cooper, A., Hawthorne, C., Gault, A., Grice, D., Nikischer, J., 2003. Arthsmithite, a new Hg1+ - Al Phosphate - Hydroxide from the Funderburk Prospect, Pike county, Arkansas, U.S.A. Can. Mineral. 41, 721–725.

Rosso, J., Rimstidt, J., 2000. A high resolution study of forsterite dissolution rates. Geochim. Cosmochim. Acta 64, 797–811.

Rozalen, M., Huertas, F.J., 2013. Comparative effect of chrysotile leaching in nitric, sulfuric and oxalic acids at room temperature. Chem. Geol. 352, 134–142.

Ryncarz, A., Laskowski, J., 1977. Influence of flotation reagents on the wet grinding

of quartz. Powder Technol. 18, 179–185.

Sacks, M.D., Tseng, T., 1983. Role of Sodium Citrate in aqueous milling of aluminum oxide. J. Am. Ceram. Soc. 66, 242–247.

Sahoo, B.K., De, S., Meikap, B.C., 2011. Improvement of grinding characteristics of Indian coal by microwave pre-treatment. Fuel Process. Technol. 92, 1920–1928.

Sanna, A., Wang, X., Lacinska, A., Styles, M., Paulson, T., Maroto-Valer, M.M., 2013. Enhancing Mg extraction from lizardite-rich serpentine for CO2 mineral sequestration. Miner. Eng. 49, 135–144.

Schena, G., Santoro, L., Favretto, S., 2007. Conceiving a high resolution and fast X-ray CT system for imaging fine multi-phase mineral particles and retrieving mineral liberation spectra. Int. J. Miner. Process. 84, 327–336.

Schindelin, J., Arganda-Carreras, I., Frise, E., Kaynig, V., Longair, M., Pietzsch, T., Preibisch, S., Rueden, C., Saalfeld, S., Schmid, B., Tinevez, J.-Y.J.-Y., White, D.J., Hartenstein, V., Eliceiri, K., Tomancak, P., Cardona, A., Liceiri, K., Tomancak, P., A., C., 2012. Fiji: An open source platform for biological image analysis. Nat. Methods 9, 676–682.

Schnatz, R., 2004. Optimization of continuous ball mills used for finish-grinding of cement by varying the L/D ratio, ball charge filling ratio, ball size and residence time. Int. J. Miner. Process. 74, 55–63.

Schneider, C.L., 1995. Measurement and calculation of liberation in continuous milling circuit. The University of Utah.

Scott, G., Bradshaw, S.M., Eksteen, J.J., 2008. The effect of microwave pretreatment on the liberation of a copper carbonatite ore after milling. Int. J. Miner. Process. 85, 121–128.

Seah, M.P., 1975. Interface adsorption, embrittlement and fracture in metallurgy. Surf. Sci. 53, 168–212.

Shi, F., 2016. An overfilling indicator for wet overflow ball mills. Miner. Eng. 95, 146–154.

Shi, F., Manlapig, E., Zuo, W., 2014. Progress and challenges in electrical comminution by high-voltage pulses. Chem. Eng. Technol. 37, 765–769.

Siegel, D.I., Pfannkuch, H.O., 1984. Silicate mineral dissolution at pH 4 and near

standard temperature and pressure. Geochim. Cosmochim. Acta 48, 197–201.

Singh, V., Obed Samuelraj, I., Venugopal, R., Jagadeesh, G., Banerjee, P.K., 2015. Study the effect of electrical and mechanical shock loading on liberation and milling characteristics of mineral materials. Miner. Eng. 70, 207–216.

Sivakumar, S., Ravisankar, R., Raghu, Y., Chandrasekaran, A., Chandramohan, J., 2013. FTIR spectroscopic studies on coastal sediment samples from Cuddalore district, Tamilnadu, India. Int. Res. J. Pure Appl. Chem. 3, 366–376.

Smith, K.S., 1999. Metal sorption on mineral surfaces: an overview with examples relating to mineral deposits. Rev. Econ. Geol. 6A–6B, 161–182.

Somasundaran, P., 1978. Theories of Grinding, in: Onoda, G.Y., Hench, L.L. (Eds.), Ceramic Processing Before Firing. John Wiley & Sons, New York, pp. 105–123.

Somasundaran, P., Lin, I.J.I.J., 1972. Effect of the nature of environment on comminution processes. Ind. Eng. Chem. Process Des. Dev. 11, 321–331.

Somasundaran, P., Wang, D., 2007. Solution Chemistry: Minerals and Reagents. Elsevier.

Stamboliadis, E.T., 2008. The evolution of a mineral liberation model by the repetition of a simple random breakage pattern. Miner. Eng. 21, 213–223.

Stumm, W., 1995. The Inner-Sphere surface complex. Aquat. Chem. 244, 1–32.

Stumm, W., 1992. Chemistry of the Interface Processes at the Solid-Water Interface. Wiley, Chichester.

Sylvester, P.J., 2012. Use of the mineral liberation analyzer (MLA) for mineralogical studies of sediments and sedimentary rocks, in: Quantitative Mineralogy and Microanalysis of Sediments and Sedimentary Rocks. Mineralogical Association of Canada Short Course Series 42, pp. 1–16.

Takigawa, Y., Ikuhara, Y., Sakuma, T., 1999. Grain boundary bonding state and fracture energy in small amount of oxide-doped fine-grained Al2O3. J. Mater. Sci. 34, 1991–1997.

Tamura, H., Mita, K., Tanaka, A., Ito, M., 2001. Mechanism of hydroxylation of metal oxide surfaces. J. Colloid Interface Sci. 243, 202–207.

Tarte, P., 1962. Etude infra-rouge des orthosilicates et des orthogermanates - II Structures du type olivine et monticellite. Spectrochim. Acta 19, 25–47.

Taşdemir, A., 2008. Evaluation of grain size distribution of unbroken chromites. Miner. Eng. 21, 711–719.

Teir, S., Revitzer, H., Eloneva, S., Fogelholm, C.-J., Zevenhoven, R., 2007. Dissolution of natural serpentinite in mineral and organic acids. Int. J. Miner. Process. 83, 36–46.

Tsuji, H., Okamura-Yoshida, A., Shishido, T., Hattori, H., 2003. Dynamic behavior of carbonate species on metal oxide surface: oxygen scrambling between adsorbed carbon dioxide and oxide surface. Langmuir 19, 8793–8800.

Tungpalan, K., Manlapig, E., Andrusiewicz, M., Keeney, L., Wightman, E., Edraki, M., 2015a. An integrated approach of predicting metallurgical performance relating to variability in deposit characteristics. Miner. Eng. 71, 49–54.

Tungpalan, K., Wightman, E., Manlapig, E., 2015b. Relating mineralogical and textural characteristics to flotation behaviour. Miner. Eng. 82, 136–140.

Ucbas, Y., Bozkurt, V., Bilir, K., Ipek, H., 2014. Concentration of chromite by means of magnetic carrier using sodium oleate and other reagents. Physicochem. Probl. Miner. Process. 50, 767–782.

van Geen, A., Robertson, A.P., Leckie, J.O., 1994. Complexation of carbonate species at the goethite surface: Implications for adsorption of metal ions in natural waters. Geochim. Cosmochim. Acta 58, 2073–2086.

Vardar, E., Eric, R.H., Letowski, F.K., 1994. Acid Leaching of Chromite. Miner. Eng. 7, 605–617.

Veasey, T.J., Wills, B.A., 1991. Review of methods of improving mineral liberation. Miner. Eng. 4, 747–752.

Vizcarra, T.G., Wightman, E.M., Johnson, N.W., Manlapig, E.V., 2010. The effect of breakage mechanism on the mineral liberation properties of sulphide ores. Miner. Eng. 23, 374–382.

Von Seebach, H.M., 1969. The effect of vapours of organic liquids on the grinding of cement clinker in ball mills. Zement-Kalk-Gips 202–211.

Wang, C.M., Iii, G.S.C., Chan, H.M., Harmer, M.P., 2000. Structure of Y and Zr segregated grain boundaries in alumina. Interface Sci. 8, 243–255.

Wang, E., Shi, F., Manlapig, E., 2012. Mineral liberation by high voltage pulses and

conventional comminution with same specific energy levels. Miner. Eng. 27–28, 28–36.

Wang, F., Giammar, D.E., 2013. Forsterite dissolution in saline water at elevated temperature and high CO2 pressure. Environ. Sci. Technol. 47, 168–173.

Wang, Y., Forssberg, E., 1995. Dispersants in stirred ball mill grinding. KONA Powder Part. J. 13, 67–77.

Wang, Y., Forssberg, E., Svensson, M., 2000. Microwave assisted comminution and liberation of minerals, in: Özbayoğlu, G., Hoşten, Ç., Atalay, Ü.M., Hiçyılmaz, C., Arol, A.İ. (Eds.), Mineral Processing on the Verge of 21st Century. A.A. Balkema, Rotterdam, pp. 3–9.

Watanabe, T., 2011. Grain boundary engineering: historical perspective and future prospects. J. Mater. Sci. 46, 4095–4115.

Wei, X., Gay, S., 1999. Liberation modelling using a dispersion equation. Miner. Eng. 12, 219–227.

Wen, S.., Yang, C.., Hsih, C.., 1998. The abnormal size distribution of comminuted heterogeneous ores due to detachment of grain boundaries fracturing. Int. J. Miner. Process. 53, 183–200.

West, G.D., Perkins, J.M., Lewis, M.H., 2007. The effect of rare earth dopants on grain boundary cohesion in alumina. J. Eur. Ceram. Soc. 27, 1913–1918.

Westwood, A.R.C., Goldheim, D.L., 1969. Mechanism for environmental control of drilling in MgO and CaF2 monocrystals.

Whiteman, E., Lotter, N.O., Amos, S.R., 2016. Process mineralogy as a predictive tool for flowsheet design to advance the Kamoa project. Miner. Eng. 96–97, 185–193.

Wightman, E.M., Evans, C.L., 2014. Representing and interpreting the liberation spectrum in a processing context. Miner. Eng. 61, 121–125.

Wills, B.A., Atkinson, K., 1993. Some observations on the fracture and liberation of mineral assemblies. Miner. Eng. 6, 697–706.

Wogelius, R.A., Walther, J. V., 1992. Olivine dissolution kinetics at near-surface conditions. Chem. Geol. 97, 101–112.

Wogelius, R.A., Walther, J. V., 1991. Olivine dissolution at 25°C: Effects of pH, CO2, and organic acids. Geochim. Cosmochim. Acta 55, 943–954.

Yin, Q., Zhu, B., Zeng, H., 2009. Microstructure, property and processing of functional ceramics. Metallurgical Industry Press & Springer, Berlin Heidelberg.

Zdravkov, B.D., Čermák, J.J., Šefara, M., Janků, J., 2007. Pore classification in the characterization of porous materials: A perspective. Cent. Eur. J. Chem. 5, 385–395.

Zhang, H., Xu, H., Zhang, X., Zhang, Y., Zhang, Y., 2014. Pressure oxidative leaching of Indian chromite ore in concentrated NaOH solution. Hydrometallurgy 142, 47–55.

Zhao, Q., Liu, C., Shi, P., Zhang, B., Jiang, M., Zhang, Q., Saxén, H., Zevenhoven, R., 2014. Sulfuric acid leaching of South African chromite. Part 1: Study on leaching behavior. Int. J. Miner. Process. 130, 95–101.

Zheng, J., 1997. Stirred media mills: dynamics, performance, and physico-chemical aspects. Columbia University.

Zhong, C. bin, Xu, C. li, Lyu, R. liang, Zhang, Z. yue, Wu, X. yan, Chi, R. an, 2017. Enhancing mineral liberation of a Canadian rare earth ore with microwave pretreatment. J. Rare Earths.

Zhou, J., Gu, Y., 2016. Geometallurgical characterization and automated mineralogy of gold ores, in: Adams, M.D. (Ed.), Gold Ore Processing. Elsevier, pp. 95–111.

APPENDIX A

pH AND CONDUCTIVITY CHANGE DURING TREATMENT EXPERIMENTS

Table A.1 pH and conductivity change in liquid during pretreatment of samples with distilled water at varying temperatures and pH.

Treatment Environment	Acidic Water at 30°C		Acidic Water at 50°C		Acidic Water at 90°C	
Time (minute)	pH	Conductivity (μs/cm)	pH	Conductivity (μs/cm)	pH	Conductivity (μs/cm)
0	3	340	3	470	3	820
5	3.06	330	3.15	400	3.43	560
10	3.11	320	3.24	370	3.88	470
15	3.15	310	3.32	350	4.61	400
Treatment Environment	Slightly-Acidic Water at 30°C		Slightly-Acidic Water at 50°C		Slightly-Acidic Water at 90°C	
Time (minute)	pH	Conductivity (μs/cm)	pH	Conductivity (μs/cm)	pH	Conductivity (μs/cm)
0	6	15.9	6	10	6	70
5	6.57	20.7	6.98	16.8	7.84	150
10	6.85	21.8	7.37	21	7.98	170
15	7.1	22.9	7.68	24.5	8.04	190
Treatment Environment	Alkaline Water at 30°C		Alkaline Water at 50°C		Alkaline Water at 90°C	
Time (minute)	pH	Conductivity (μs/cm)	pH	Conductivity (μs/cm)	pH	Conductivity (μs/cm)
0	10	187.8	10	112.1	10	1090
5	9.97	200.9	9.96	118.4	9.95	870
10	9.96	203.6	9.94	119.5	9.93	1140
15	9.95	205.9	9.92	119.2	9.9	1210

EQUILIBRIUM DIAGRAMS OF SALT SOLUTIONS
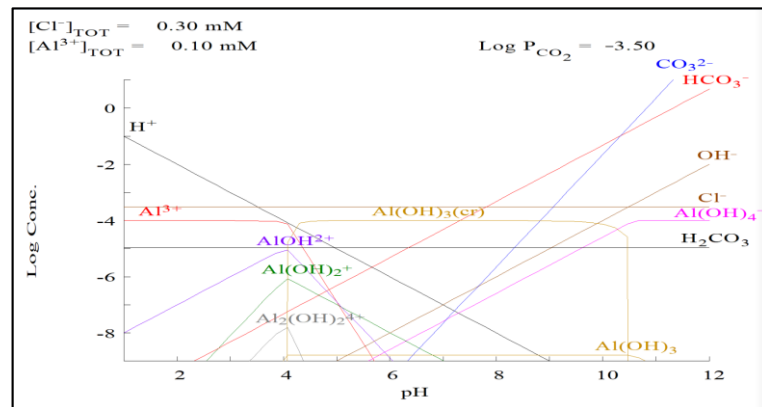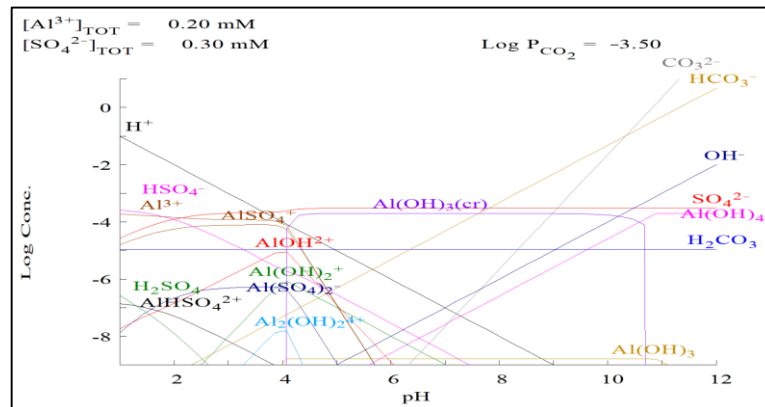

Figure B.1 Equilibrium diagram of 10^{-4} M AlCl$_3$ solution at 25°C

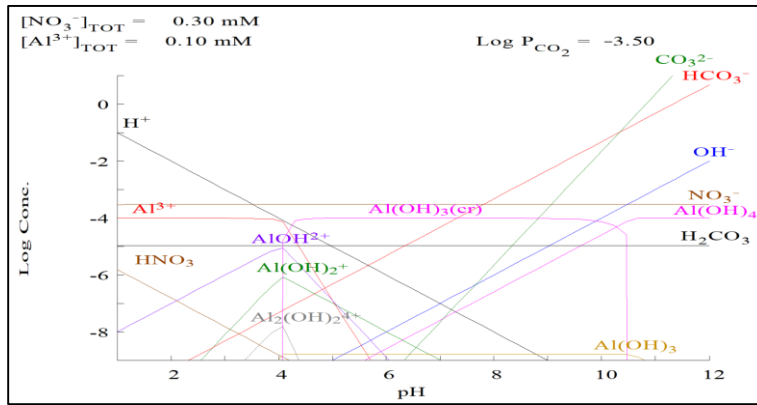

Figure B.2 Equilibrium diagram of 10^{-4} M Al$_2$(SO$_4$)$_3$ solution at 25°C.
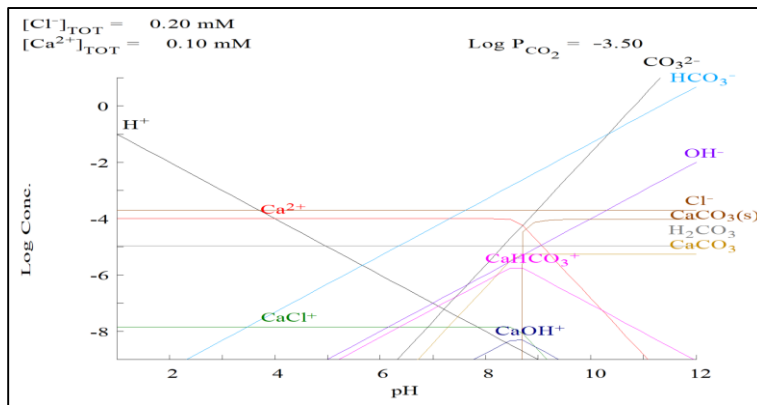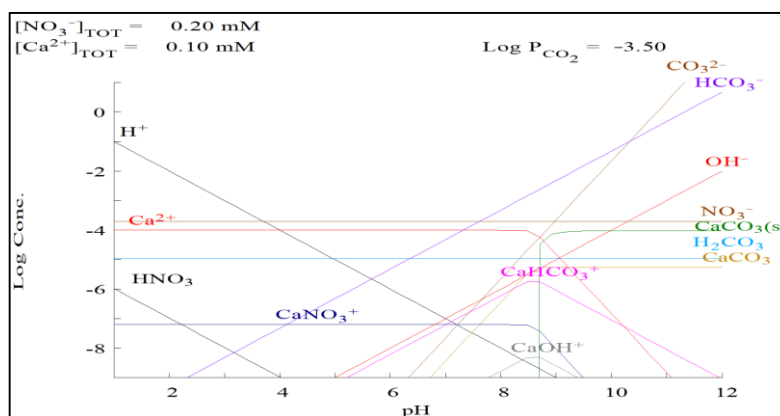
Figure B.3 Equilibrium diagram of 10^{-4} M $Al(NO_3)_3$ solution at 25°C.

Figure B.4 Equilibrium diagram of 10^{-4} M $CaCl_2$ solution at 25°C.
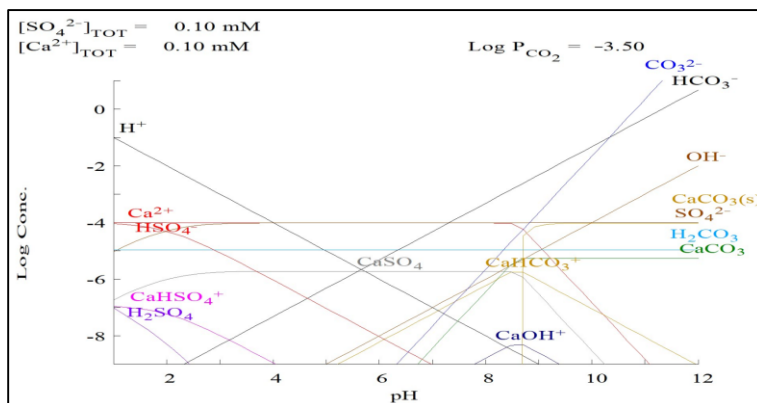
Figure B.5 Equilibrium diagram of 10^{-4} M $CaSO_4$ solution at 25°C.

102

Figure B.6 Equilibrium diagram of 10^{-4} M $Ca(NO_3)_2$ solution at 25°C.
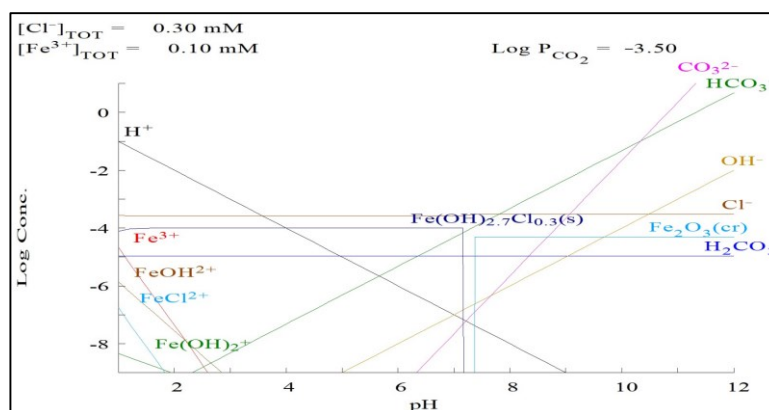
Figure B.7 Equilibrium diagram of 10^{-4} M $FeCl_3$ solution at 25°C.
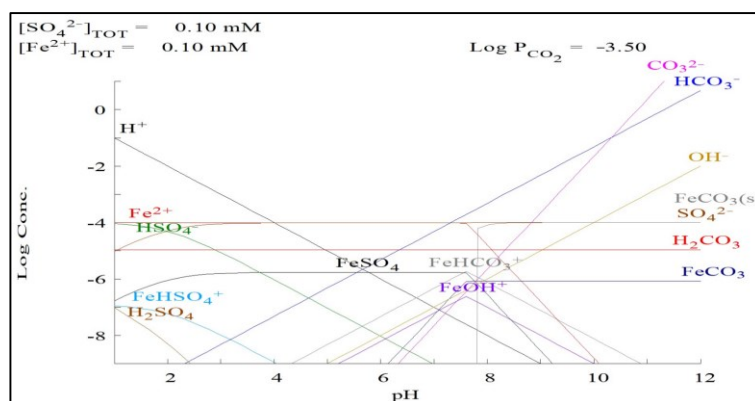
Figure B.8 Equilibrium diagram of 10^{-4} M $FeSO_4$ solution at 25°C.

103

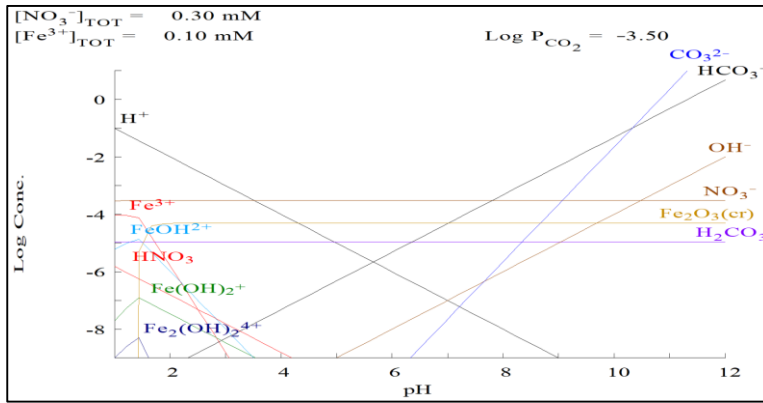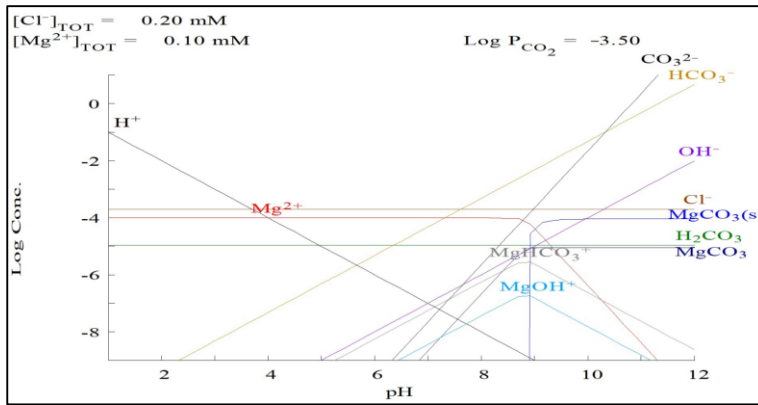Figure B.9 Equilibrium diagram of 10^{-4} M Fe(NO$_3$)$_3$ solution at 25°C.
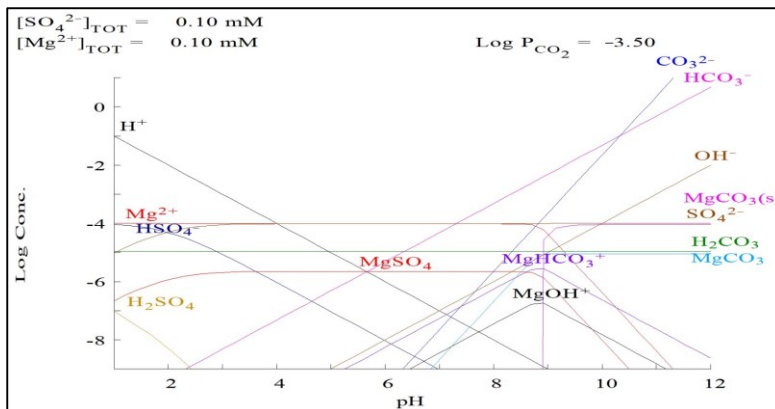

Figure B.10 Equilibrium diagram of 10^{-4} M MgCl$_2$ solution at 25°C.

Figure B.11 Equilibrium diagram of 10^{-4} M MgSO$_4$ solution at 25°C.
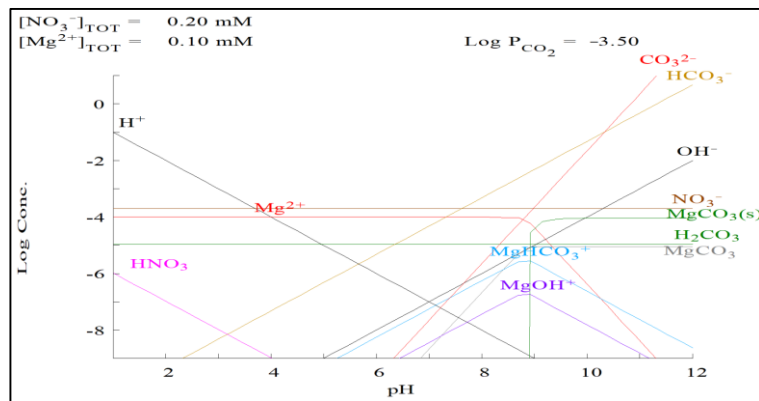
Figure B.12 Equilibrium diagram of 10^{-4} M $Mg(NO_3)_2$ solution at 25°C.

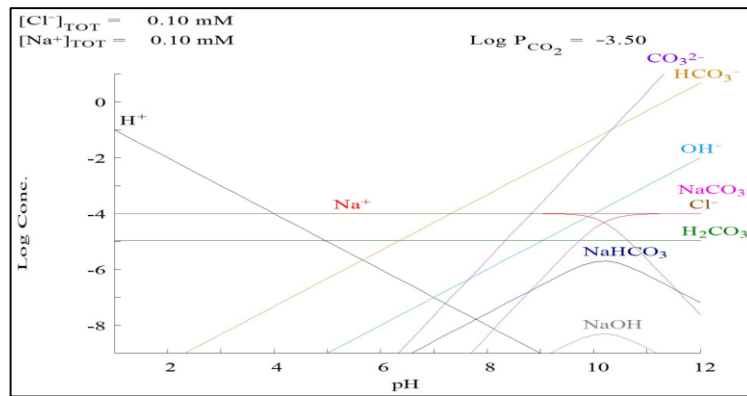Figure B.13 Equilibrium diagram of 10^{-4} M NaCl solution at 25°C.

Figure B.14 Equilibrium diagram of 10^{-4} M Na_2SO_4 solution at 25°C.
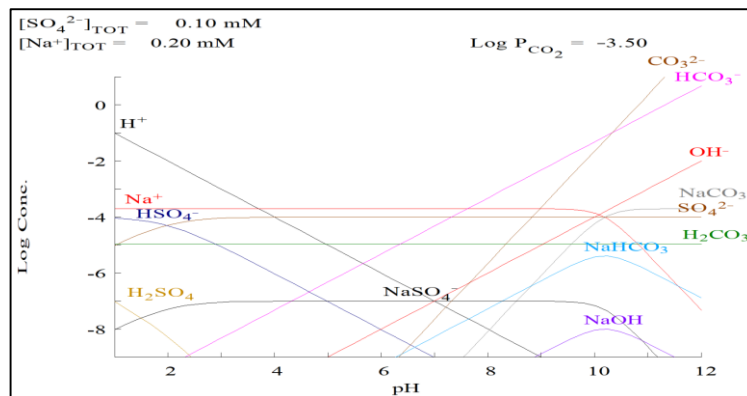
105

Figure B.15 Equilibrium diagram of 10^{-4} M $NaNO_3$ solution at 25°C.

Figure B.16 Equilibrium diagram of 10^{-4} M Na_2CO_3 solution at 25°C.

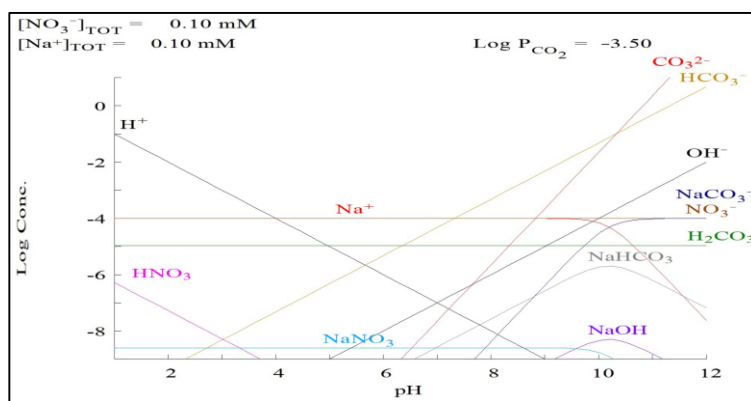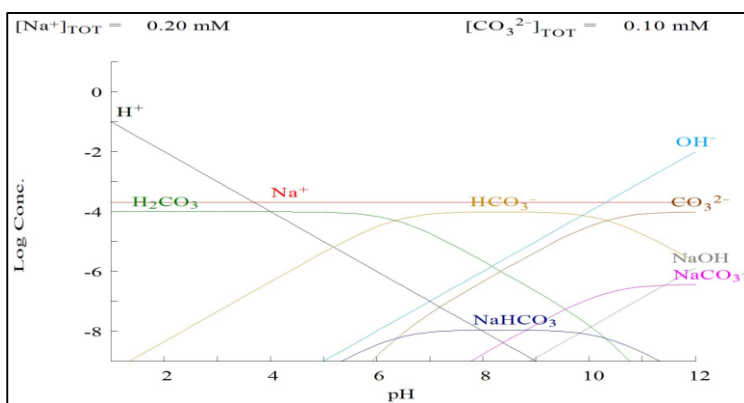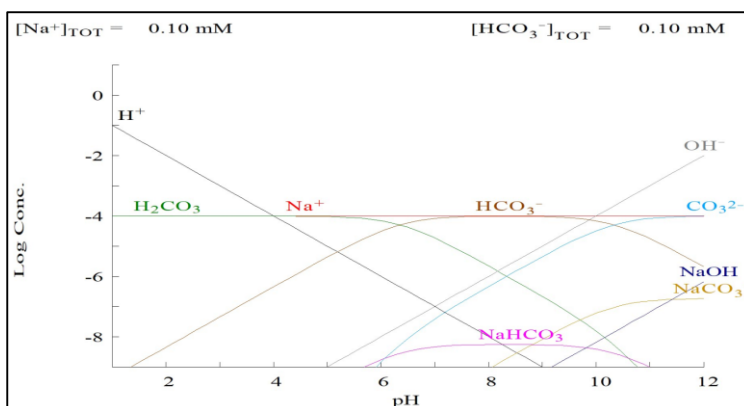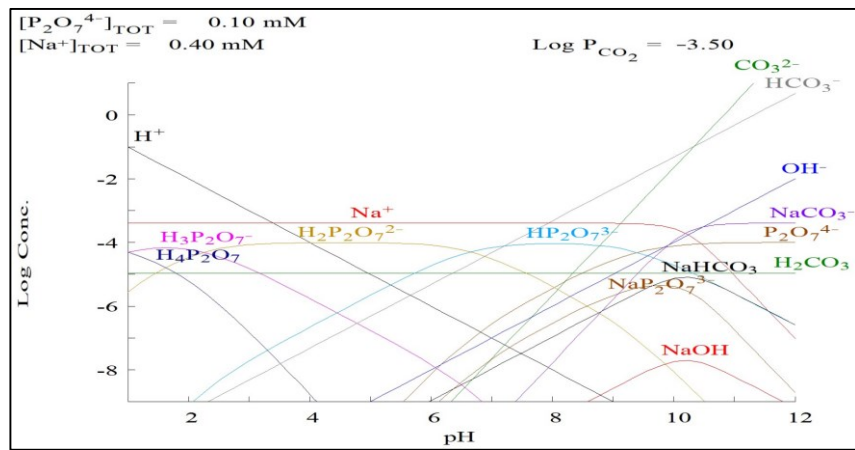Figure B.17 Equilibrium diagram of 10^{-4} M $NaHCO_3$ solution at 25°C.

Figure B.18 Equilibrium diagram of 10^{-4} M Na-pyrophosphate solution at 25°C.

APPENDIX C

SCREENING ANALYSES

Table C.1 Screening analyses of untreated samples broken at various specific breakage energy levels in drop weight tester

Condition	Untreated			
Specific Breakage Energy (J/g)	0.21	1	10	20
Size Class	Weight(g)			
+9.53 mm	0	0	0	0
-9.53+6.35 mm	12.09	3.94	0	0
-6.35+4.7 mm	3.29	3.61	0	0
-4.7+3.35 mm	2.53	4.6	0.15	0
-3.35+2.36 mm	2.31	3.4	0.73	0.08
-2.36+1.7 mm	0.9	2.09	1.89	0.65
-1.7+1.18 mm	0.59	1.84	2.95	2.13
-1.18+0.85 mm	0.4	1.06	2.76	2.82
-0.85+0.60 mm	0.25	0.82	2.24	2.81
-0.60+0.425 mm	0.24	0.79	2.31	3.02
-0.425+0.300 mm	0.15	0.6	1.86	2.36
-0.300+0.212 mm	0.18	0.58	1.86	2.47
-0.212+0.150 mm	0.13	0.52	1.77	2.33
-0.150 mm	0.47	1.48	6.43	11.49
Total	23.53	25.33	24.95	30.16

Table C.2 Screening analyses of samples treated in acidic solutions of Al-salts, Mg-salts, Amine, and then broken in drop weight tester

Treatment Environment	Acidic Salt or Surfactant Solutions						
Additive Type	$AlCl_3$	$Al_2(SO_4)_3$	$Al(NO_3)_3$	$MgCl_2$	$MgSO_4$	$Mg(NO_3)_2$	Amine
Specific Breakage Energy (J/g)	10						
Size (mm)	Weight(g)						
+9.53 mm	0	0	0	0	0	0	0
-9.53+6.35 mm	0	0	0	0	0	0	0
-6.35+4.7 mm	0	0	0	0	0	0	0
-4.7+3.35 mm	0.09	0.05	0.25	0.07	0.07	0.19	0.14
-3.35+2.36 mm	0.6	0.7	0.83	0.62	0.58	1.4	1.43
-2.36+1.7 mm	1.24	1.84	1.14	1.6	1.81	1.62	1.89
-1.7+1.18 mm	2.66	2.75	2.21	2.47	3.09	2.55	2.87
-1.18+0.85 mm	2.7	2.46	2.76	2.56	2.74	2.52	2.54
-0.85+0.60 mm	2.41	2.47	2.47	2.36	2.62	2.25	2.01
-0.60+0.425 mm	2.5	2.38	2.54	2.35	2.36	2.36	2.01
-0.425+0.300 mm	1.96	1.91	2.02	1.88	1.86	1.88	1.66
-0.300+0.212 mm	2.02	1.92	2	1.96	1.81	1.8	1.61
-0.212+0.150 mm	1.86	1.78	1.85	1.79	1.67	1.63	1.71
-0.150 mm	7.01	6.81	7.09	7.17	6.47	6.1	6.32
Total	25.05	25.07	25.16	24.83	25.08	24.3	24.19

Table C.3 Screening analyses of samples treated in slightly-acidic solutions of Al-salts, Mg-salts,Amine, and then broken in drop weight tester

Treatment Environment	Slightly-Acidic Salt or Surfactant Solutions						
Additive Type	$AlCl_3$	$Al_2(SO_4)_3$	$Al(NO_3)_3$	$MgCl_2$	$MgSO_4$	$Mg(NO_3)_2$	Amine
Specific Breakage Energy (J/g)				10			
Size (mm)				Weight(g)			
+9.53 mm	0	0	0	0	0	0	0
-9.53+6.35 mm	0	0	0	0	0	0	0.74
-6.35+4.7 mm	0	0	0.16	0	0	0	0
-4.7+3.35 mm	0.09	0.06	0.8	0	0.47	0.33	0.45
-3.35+2.36 mm	0.47	0.74	0.96	0.69	1.36	0.37	0.84
-2.36+1.7 mm	1.77	1.77	1.41	1.5	1.79	1.21	1.26
-1.7+1.18 mm	2.83	2.68	2.31	2.14	2.82	2.59	2.84
-1.18+0.85 mm	2.92	2.91	2.47	2.28	2.74	2.9	2.33
-0.85+0.60 mm	2.47	2.46	2.11	2.64	2.36	2.51	1.83
-0.60+0.425 mm	2.4	2.4	2.36	2.65	2.2	2.55	2.02
-0.425+0.300 mm	1.83	1.92	1.9	2.02	1.69	2.03	1.76
-0.300+0.212 mm	1.84	1.94	1.93	2.03	1.69	1.93	1.84
-0.212+0.150 mm	1.66	1.75	1.77	1.85	1.58	1.75	1.86
-0.150 mm	6.41	6.64	7.27	6.93	6.36	6.33	6.71
Total	24.69	25.27	25.45	24.73	25.06	24.5	24.48

Table C.4 Screening analyses of samples treated in alkaline solutions of Al-salts, Mg-salts, Amine, and then broken in drop weight tester

Treatment Environment	Alkaline Salt or Surfactant Solutions						
Additive Type	$AlCl_3$	$Al_2(SO_4)_3$	$Al(NO_3)_3$	$MgCl_2$	$MgSO_4$	$Mg(NO_3)_2$	Amine
Specific Breakage Energy (J/g)				10			
Size (mm)				Weight(g)			
+9.53 mm	0	0	0	0	0	0	0
-9.53+6.35 mm	0	0	0	0	0	0	0
-6.35+4.7 mm	0	0	0	0	0	0.59	0
-4.7+3.35 mm	0.29	0.23	0	0.2	0.42	0.4	0.16
-3.35+2.36 mm	0.76	0.47	0.24	0.54	0.86	0.84	0.97
-2.36+1.7 mm	1.37	1.62	0.84	1.88	1.38	1.24	1.33
-1.7+1.18 mm	2.4	2.66	2.1	2.77	2.48	2.26	2.25
-1.18+0.85 mm	2.51	2.75	2.81	2.61	2.43	2.76	2.24
-0.85+0.60 mm	2.25	2.51	2.73	2.26	2.47	2.7	2.03
-0.60+0.425 mm	2.46	2.35	2.66	2.31	2.49	2.46	2.12
-0.425+0.300 mm	1.93	1.89	2.08	1.9	2.02	1.84	1.77
-0.300+0.212 mm	2.01	2	2.05	1.84	1.98	1.77	1.82
-0.212+0.150 mm	1.87	1.85	2.02	1.71	1.75	1.62	1.88
-0.150 mm	7.18	7.17	7.24	6.51	6.55	6.16	6.77
Total	25.03	25.5	24.77	24.53	24.83	24.64	23.34

Table C.5 Screening analyses of samples treated in acidic solutions of Fe-salts, Ca-salts, PEX, and then broken in drop weight tester

Treatment Environment	Acidic Salt or Surfactant Solutions						
Additive Type	$FeCl_3$	$Fe_2(SO4)_3$	$Fe(NO_3)_3$	$CaCl_2$	$CaSO_4$	$Ca(NO_3)_2$	PEX
Specific Breakage Energy (J/g)	10						
Size (mm)	Weight(g)						
+9.53 mm	0	0	0	0	0	0	0
-9.53+6.35 mm	0	0	0	0	0	0	0
-6.35+4.7 mm	0	0	0	0	0	0	0
-4.7+3.35 mm	0.09	0	0.17	0.23	0.2	0.2	0.12
-3.35+2.36 mm	0.28	0.83	0.42	1.18	0.57	0.96	0.39
-2.36+1.7 mm	1.45	1.44	0.92	1.69	1.22	1.45	1.55
-1.7+1.18 mm	2.75	2.53	2.38	2.19	2.27	2.39	2.99
-1.18+0.85 mm	3.04	2.67	2.91	2.33	2.35	2.55	2.81
-0.85+0.60 mm	2.67	2.37	2.36	2.26	2.37	2.6	2.42
-0.60+0.425 mm	2.47	2.42	2.55	2.22	2.55	2.42	2.52
-0.425+0.300 mm	1.91	2.05	2.01	1.79	2.06	1.92	2.03
-0.300+0.212 mm	1.91	1.99	1.96	1.91	1.96	1.96	2.02
-0.212+0.150 mm	1.72	1.79	1.91	1.75	1.83	1.83	1.78
-0.150 mm	6.49	7.66	7	6.84	6.57	6.74	6.34
Total	24.78	25.75	24.59	24.39	23.95	25.02	24.97

Table C.6 Screening analyses of samples treated in slightly-acidic solutions of Fe-salts, Ca-salts, PEX, and then broken in drop weight tester

Treatment Environment	Slightly-Acidic Salt or Surfactant Solutions						
Additive Type	$FeCl_3$	$Fe_2(SO4)_3$	$Fe(NO_3)_3$	$CaCl_2$	$CaSO_4$	$Ca(NO_3)_2$	PEX
Specific Breakage Energy (J/g)	10						
Size (mm)	Weight(g)						
+9.53 mm	0	0	0	0	0	0	0
-9.53+6.35 mm	0	0	0	0	0	0	0
-6.35+4.7 mm	0	0	0.22	0	0	0	0
-4.7+3.35 mm	0.19	0.27	0.12	0.16	0.15	0.23	0.31
-3.35+2.36 mm	0.07	0.82	0.91	0.71	1.65	1.07	1.12
-2.36+1.7 mm	0.86	1.43	1.38	1.7	1.7	1.25	1.81
-1.7+1.18 mm	2.12	2.29	2.36	2.85	2.28	2.32	2.82
-1.18+0.85 mm	2.8	2.52	2.52	2.73	2.34	2.44	2.39
-0.85+0.60 mm	2.77	2.52	2.09	2.32	2.32	2.16	2.27
-0.60+0.425 mm	2.76	2.56	2.21	2.34	2.31	2.33	2.35
-0.425+0.300 mm	2.11	1.97	1.92	1.85	1.84	1.9	1.86
-0.300+0.212 mm	2.07	1.89	1.94	1.84	1.87	1.92	1.81
-0.212+0.150 mm	1.87	1.71	1.84	1.71	1.67	1.82	1.65
-0.150 mm	6.92	6.77	6.66	6.58	6.68	6.83	6.47
Total	24.54	24.75	24.17	24.79	24.81	24.27	24.86

Table C.7 Screening analyses of samples treated in alkaline solutions of Fe-salts, Ca-salts, PEX, and then broken in drop weight tester

Treatment Environment	Slightly-Acidic Salt or Surfactant Solutions						
Additive Type	FeCl$_3$	Fe$_2$(SO4)$_3$	Fe(NO$_3$)$_3$	CaCl$_2$	CaSO$_4$	Ca(NO$_3$)$_2$	PEX
Specific Breakage Energy (J/g)	10						
Size (mm)	Weight(g)						
+9.53 mm	0	0	0	0	0	0	0
-9.53+6.35 mm	0	0	0	0	0	0	0
-6.35+4.7 mm	0	0	0	0.3	0	0	0
-4.7+3.35 mm	0.12	0.63	0.07	0.48	0	0.09	0
-3.35+2.36 mm	0.78	1.34	0.98	0.6	0.16	0.86	0.36
-2.36+1.7 mm	1	1.34	1.57	1.54	1.4	1.55	1.58
-1.7+1.18 mm	2.57	2.5	2.66	2.86	2.57	2.33	2.87
-1.18+0.85 mm	2.84	2.37	2.62	2.7	2.73	2.46	3.14
-0.85+0.60 mm	2.63	2.31	2.27	2.23	2.47	2.4	2.35
-0.60+0.425 mm	2.58	2.34	2.27	2.4	2.52	2.42	2.47
-0.425+0.300 mm	2	1.81	1.9	1.81	2.07	1.95	1.78
-0.300+0.212 mm	1.99	1.83	1.95	1.76	2.06	1.96	1.98
-0.212+0.150 mm	1.82	1.68	1.79	1.62	1.82	1.84	1.95
-0.150 mm	6.88	6.64	6.6	6.18	6.77	6.74	6.19
Total	25.21	24.79	24.68	24.48	24.57	24.6	24.67

APPENDIX D

EPMA ANALYSES
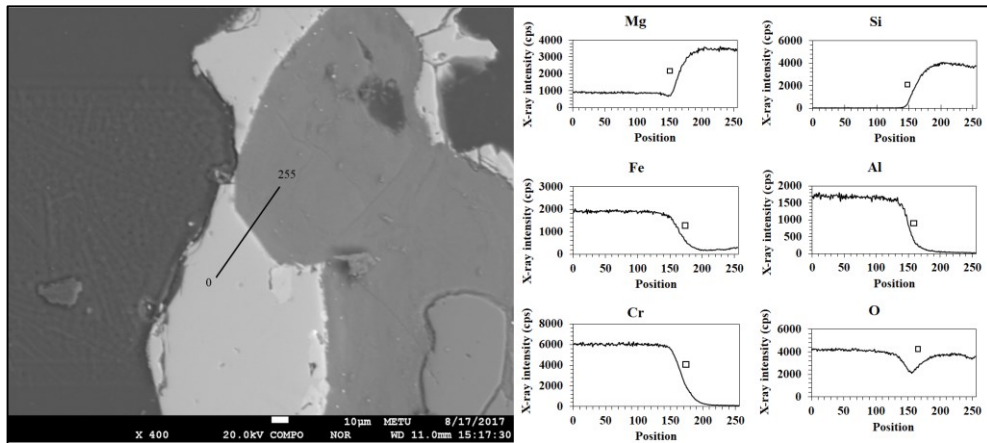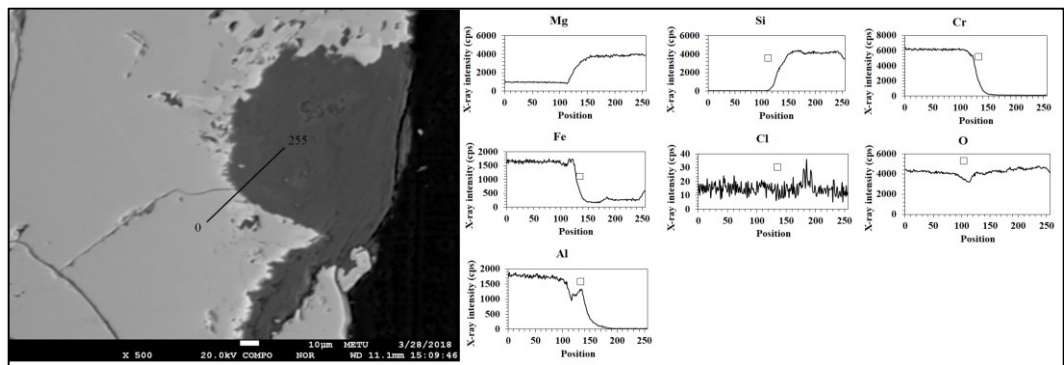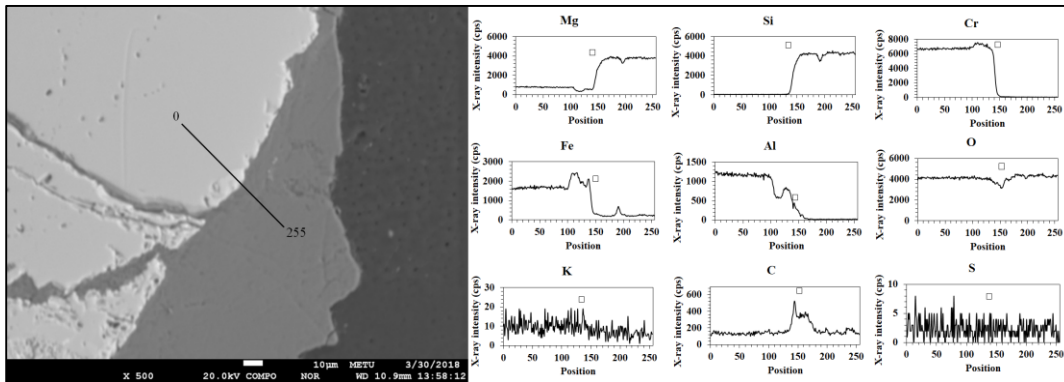

Figure D.1 The elemental map of a line segment (left) taken from a sample surface after treatment in acidic water at 50°C. (□ represents the grain-boundary region)
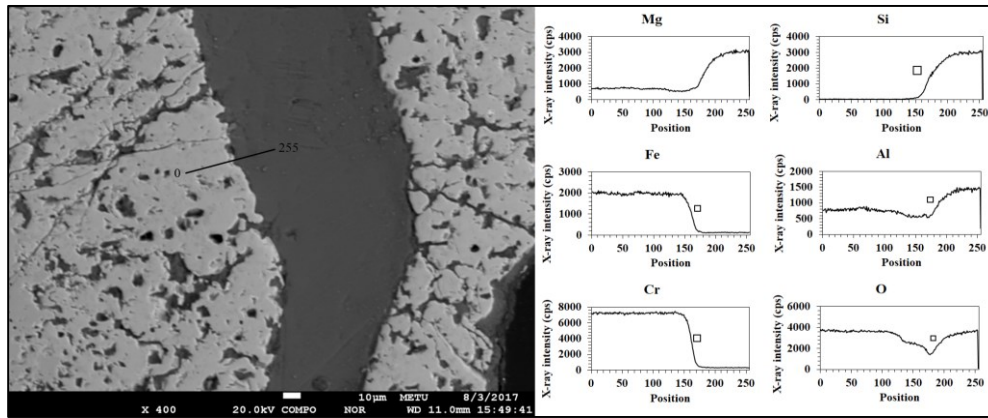
Figure D.2 The elemental map of a line segment (left) taken from a sample surface after treatment in acidic water at 90°C. (□ represents the grain-boundary region)
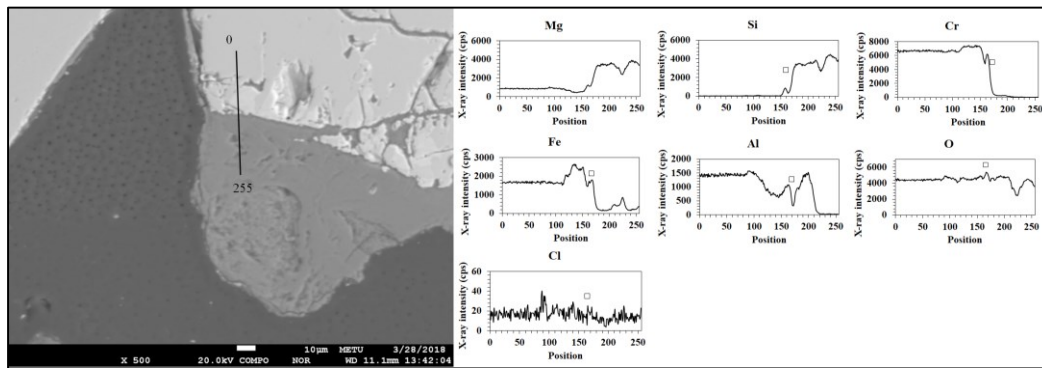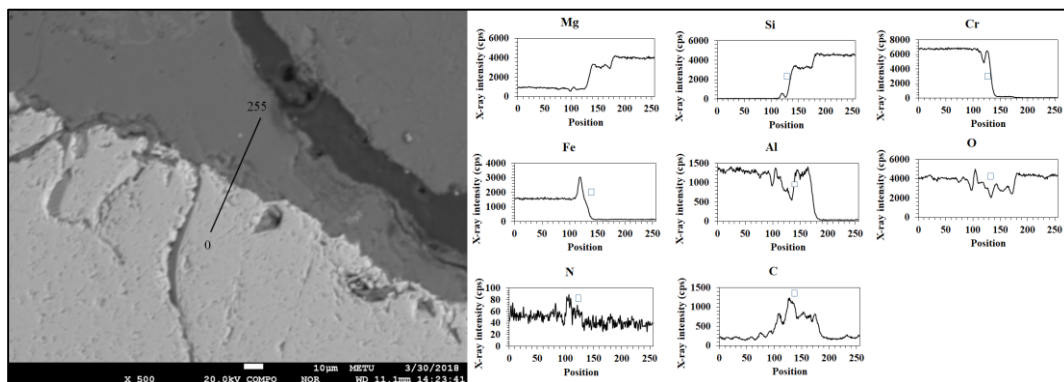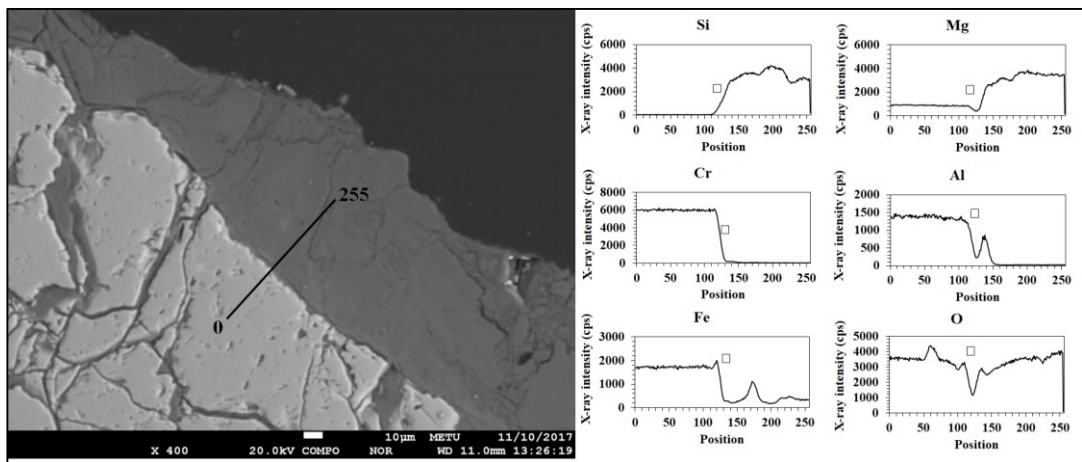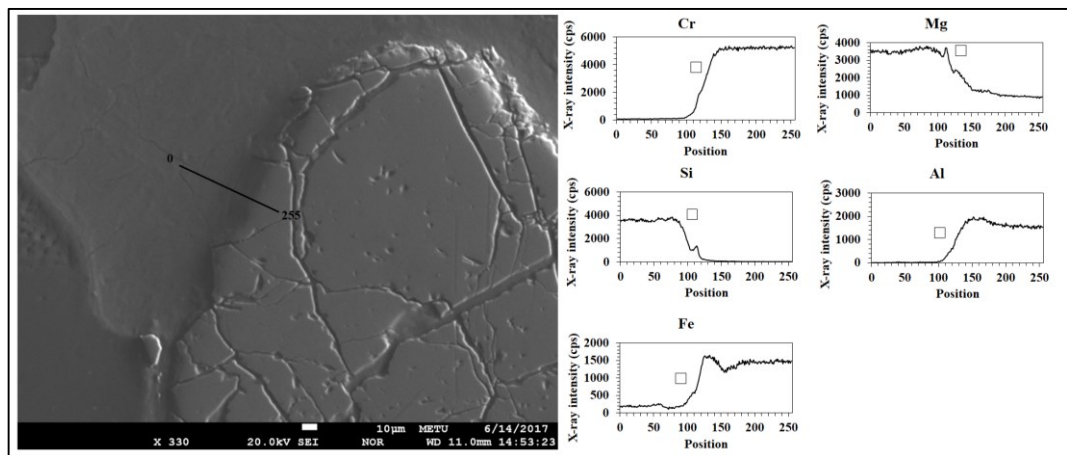

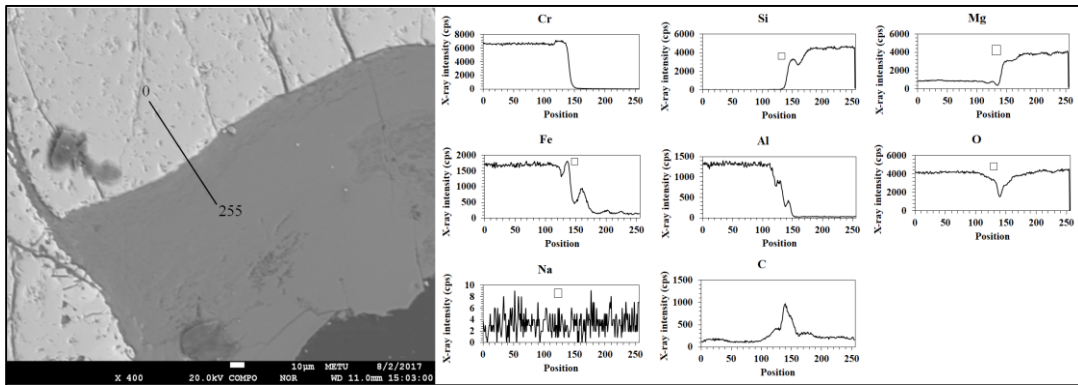Figure D.3 The elemental map of a line segment (left) taken from a sample surface after treatment in acidic FeCl$_3$ solution at 50°C. (□ represents the grain-boundary region)
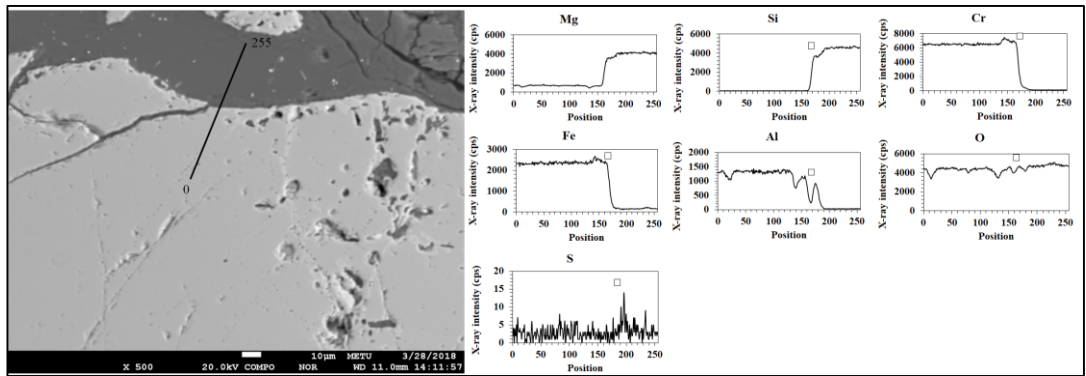
Figure D.4 The elemental map of a line segment (left) taken from a sample surface after treatment in acidic $FeSO_4$ solution at 50°C. (□ represents the grain-boundary region)
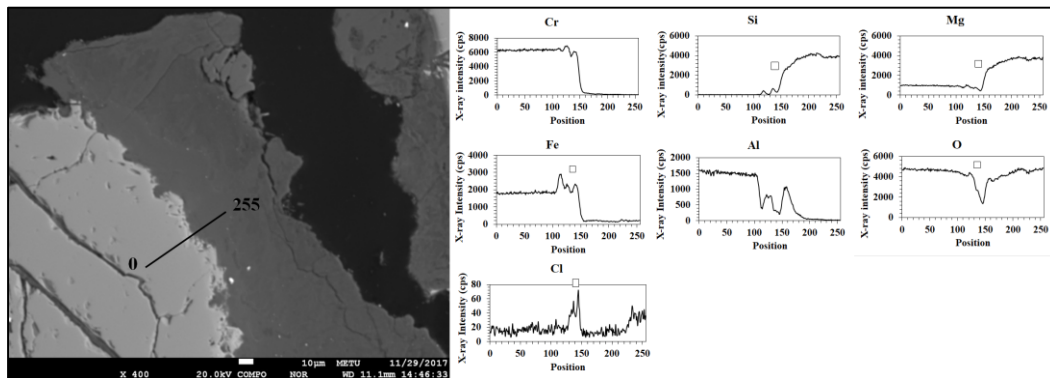

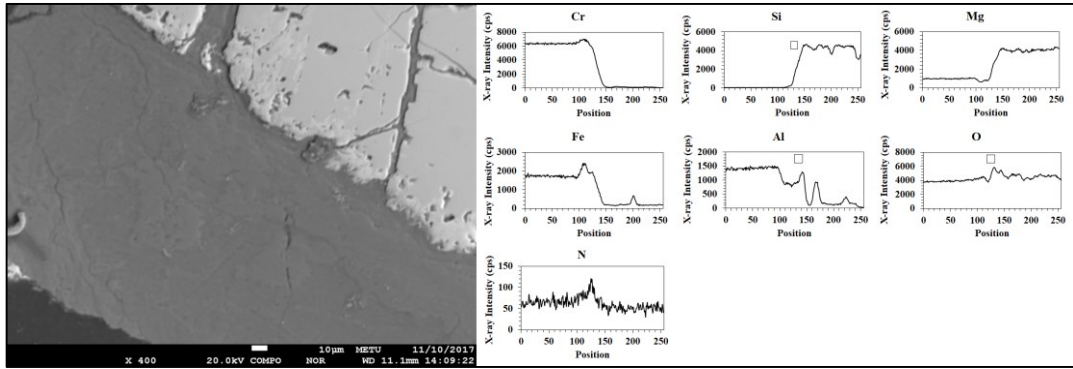Figure D.5 The elemental map of a line segment (left) taken from a sample surface after treatment in acidic $AlCl_3$ solution at 50°C. (□ represents the grain-boundary region)

Figure D.6 The elemental map of a line segment (left) taken from a sample surface after treatment in acidic PEX solution at 50°C. (□ represents the grain-boundary region)
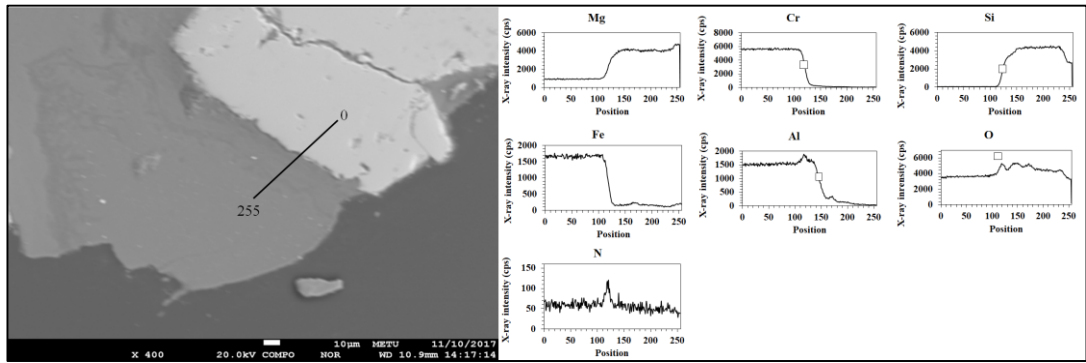

Figure D.7 The elemental map of a line segment (left) taken from a sample surface after treatment in acidic Amine solution at 50°C. (□ represents the grain-boundary region)

Figure D.8 The elemental map of a line segment (left) taken from a sample surface after treatment in slightly-acidic distilled water at 30°C. (□ represents the grain-boundary region)

Figure D.9 The elemental map of a line segment (left) taken from a sample surface after treatment in slightly-acidic distilled water at 50°C. (□ represents the grain-boundary region)
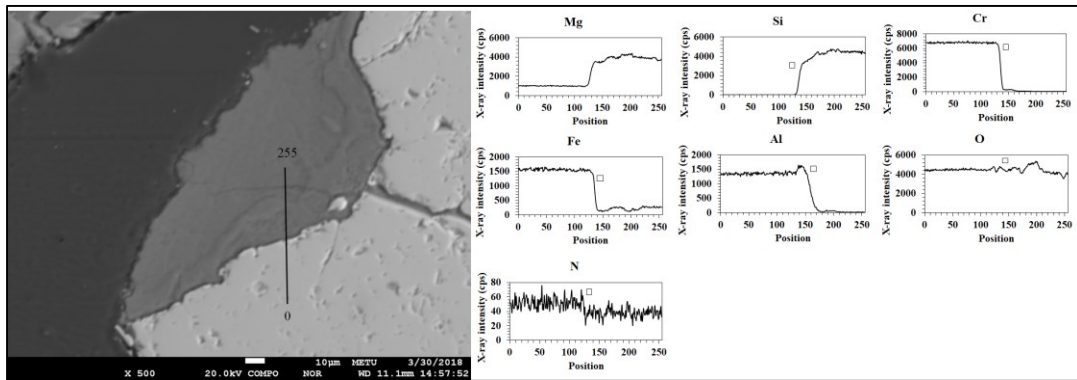
Figure D.10 The elemental map of a line segment (left) taken from a sample surface after treatment in slightly-acidic Na_2CO_3 solution at 50°C. (□ represents the grain-boundary region of the sample)
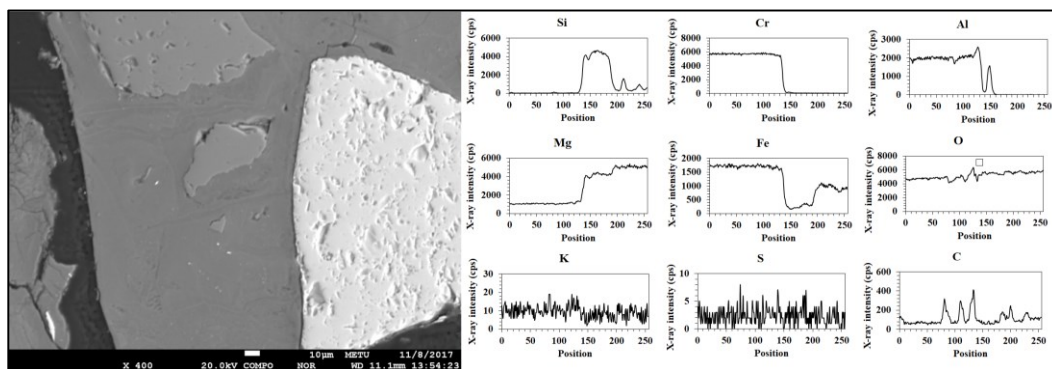

Figure D.11 The elemental map of a line segment (left) taken from a sample surface after treatment in slightly-acidic $FeCl_3$ solution at 50°C. (□ represents the grain-boundary region)

Figure D.12 The elemental map of a line segment (left) taken from a sample surface after treatment in slightly-acidic $Fe(NO_3)_3$ solution at 50°C. (□ represents the grain-boundary region)
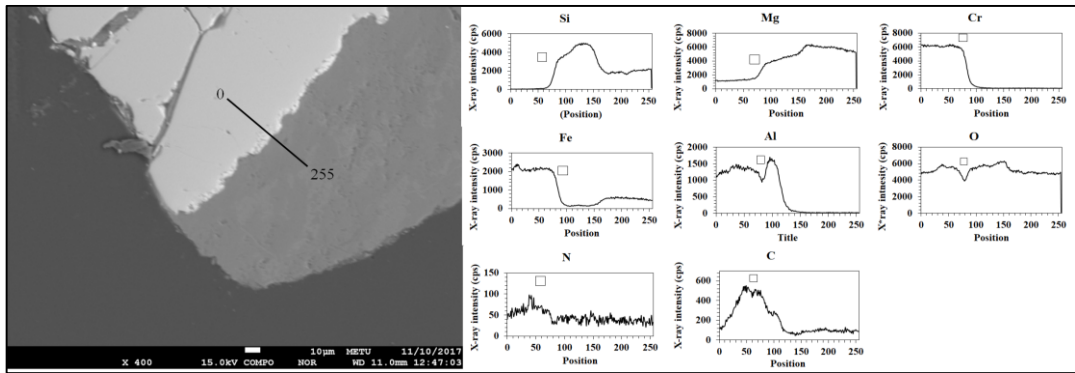

Figure D.13 The elemental map of a line segment (left) taken from a sample surface after treatment in slightly-acidic $AlNO_3$ solution at 50°C. (□ represents the grain-boundary region)
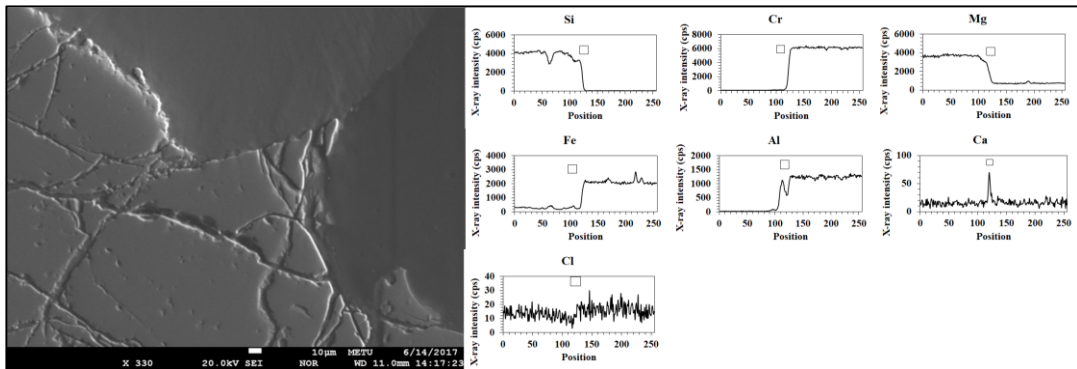
Figure D.14 The elemental map of a line segment (left) taken from a sample surface after treatment in slightly-acidic $Mg(NO_3)_2$ solution at 50°C. (□ represents the grain-boundary region)

Figure D.15 The elemental map of a line segment (left) taken from a sample surface after treatment in slightly-acidic PEX solution at 50°C. (□ represents the grain-boundary region)

Figure D.16 The elemental map of a line segment (left) taken from a sample surface after treatment in slightly-acidic Amine solution at 50°C. (□ represents the grain-boundary region)

Figure D.17 The elemental map of a line segment (left) taken from a sample surface after treatment in alkaline $CaCl_2$ solution at 50°C. (□ represents the grain-boundary region)
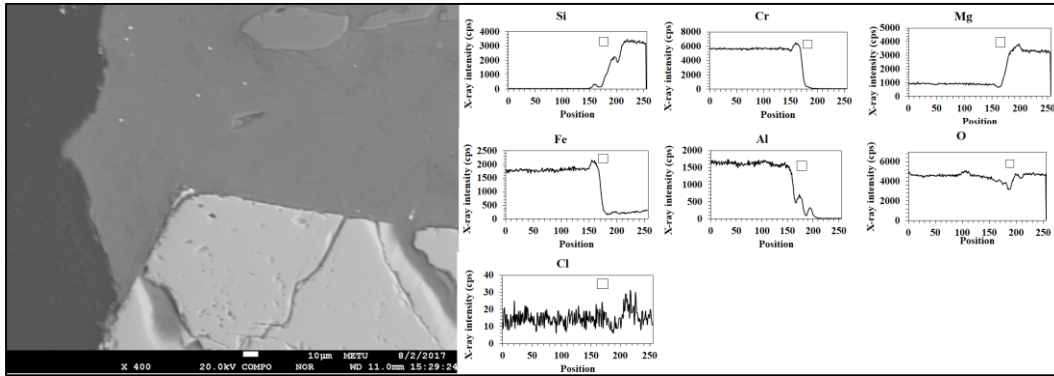
Figure D.18 The elemental map of a line segment (left) taken from a sample surface after treatment in alkaline FeCl$_3$ solution at 50°C. (□ represents the grain-boundary region)
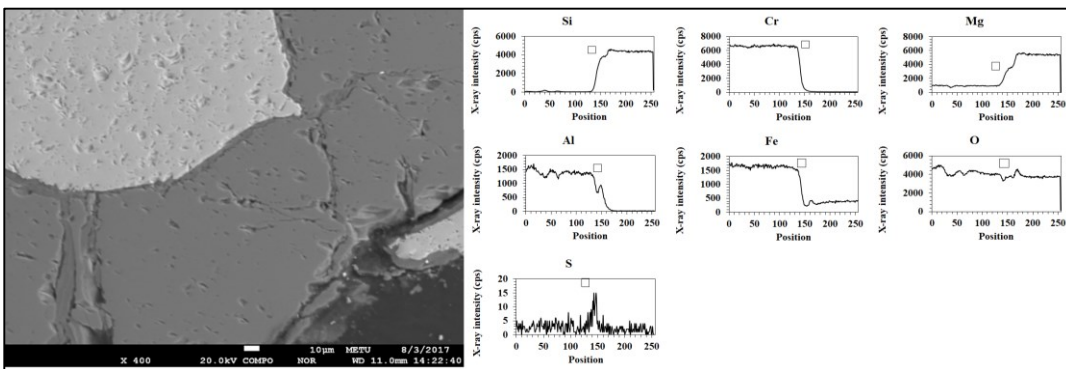

Figure D.19 The elemental map of a line segment (left) taken from a sample surface after treatment in alkaline FeSO$_4$ solution at 50°C. (□ represents the grain-boundary region)
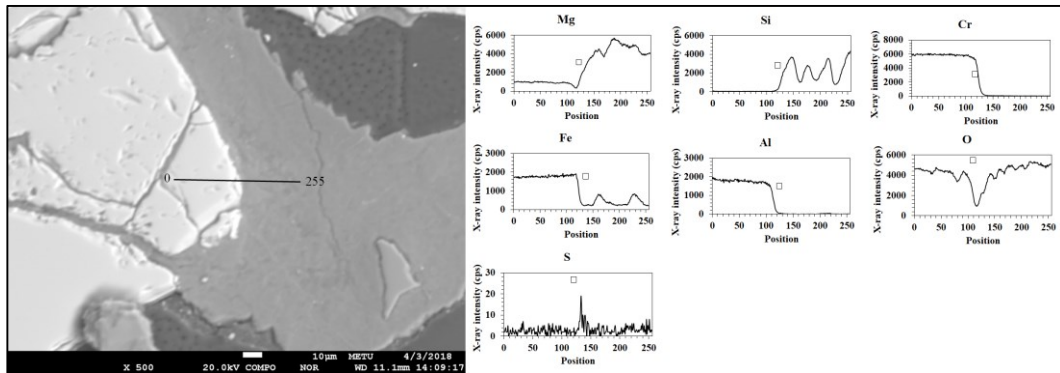
Figure D.20 The elemental map of a line segment (left) taken from a sample surface after treatment in alkaline $Al_2(SO_4)_3$ solution at 50°C. (□ represents the grain-boundary region)
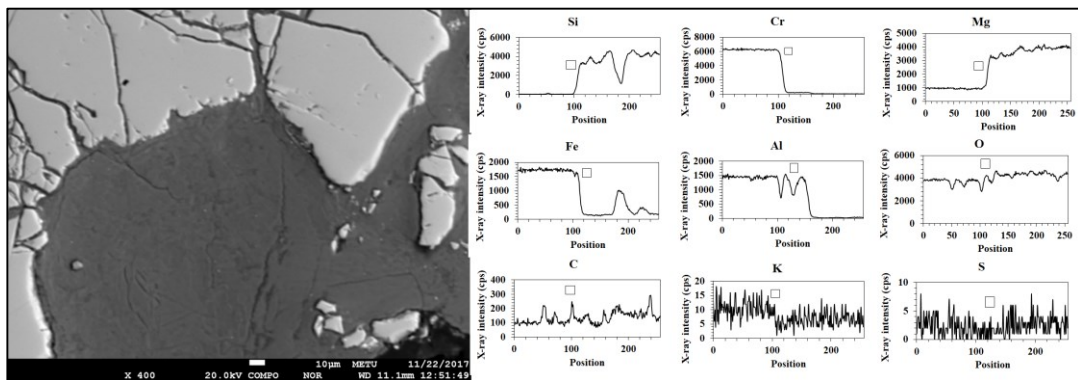

Figure D.21 The elemental map of a line segment (left) taken from a sample surface after treatment in alkaline PEX solution at 50°C. (□ represents the grain-boundary region)
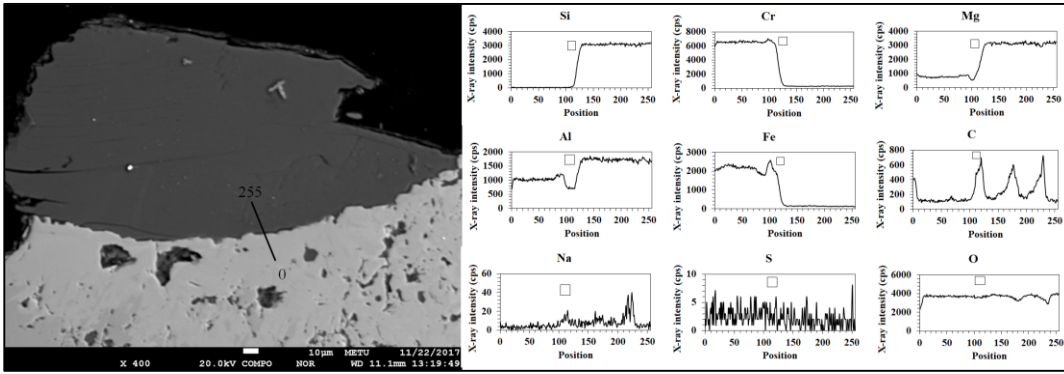
Figure D.22 The elemental map of a line segment (left) taken from a sample surface after treatment in alkaline SLS solution at 50°C. (□ represents the grain-boundary region)

APPENDIX E

SEM ANALYSES

Figure E.1 a) Secondary electron and b) corresponding Backscatter electron images of progeny particles of samples treated in (1) acidic (2) slightly-acidic and (3) alkaline $FeCl_3$ solutions
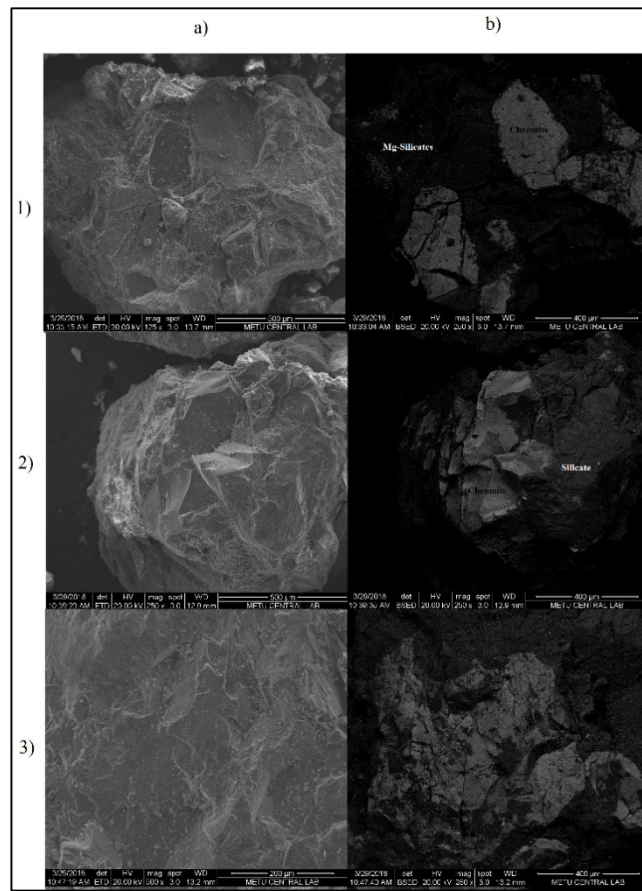
Figure E.2 a) Secondary electron and b) corresponding Backscatter electron images
of progeny particles of samples treated in (1) acidic (2) slightly-acidic and (3)
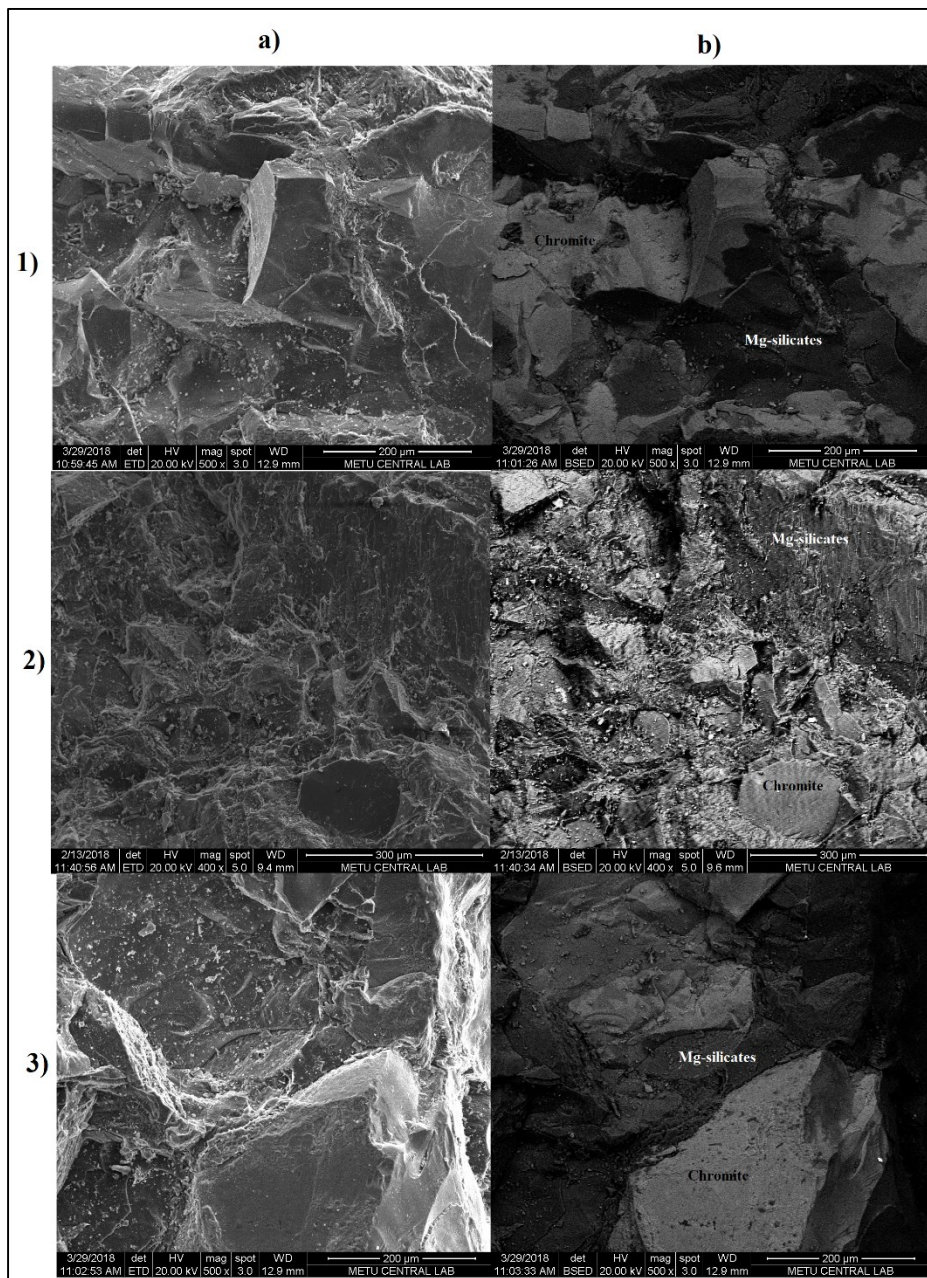alkaline $FeSO_4$ solutions

Figure E.3 a) Secondary electron and b) corresponding Backscatter electron images
of progeny particles of samples treated in (1) acidic (2) slightly-acidic and (3)
alkaline PEX solutions

Figure E.4 a) Secondary electron and b) corresponding Backscatter electron images of progeny particles of samples treated in (1) acidic (2) slightly-acidic and (3) alkaline $AlCl_3$ solutions
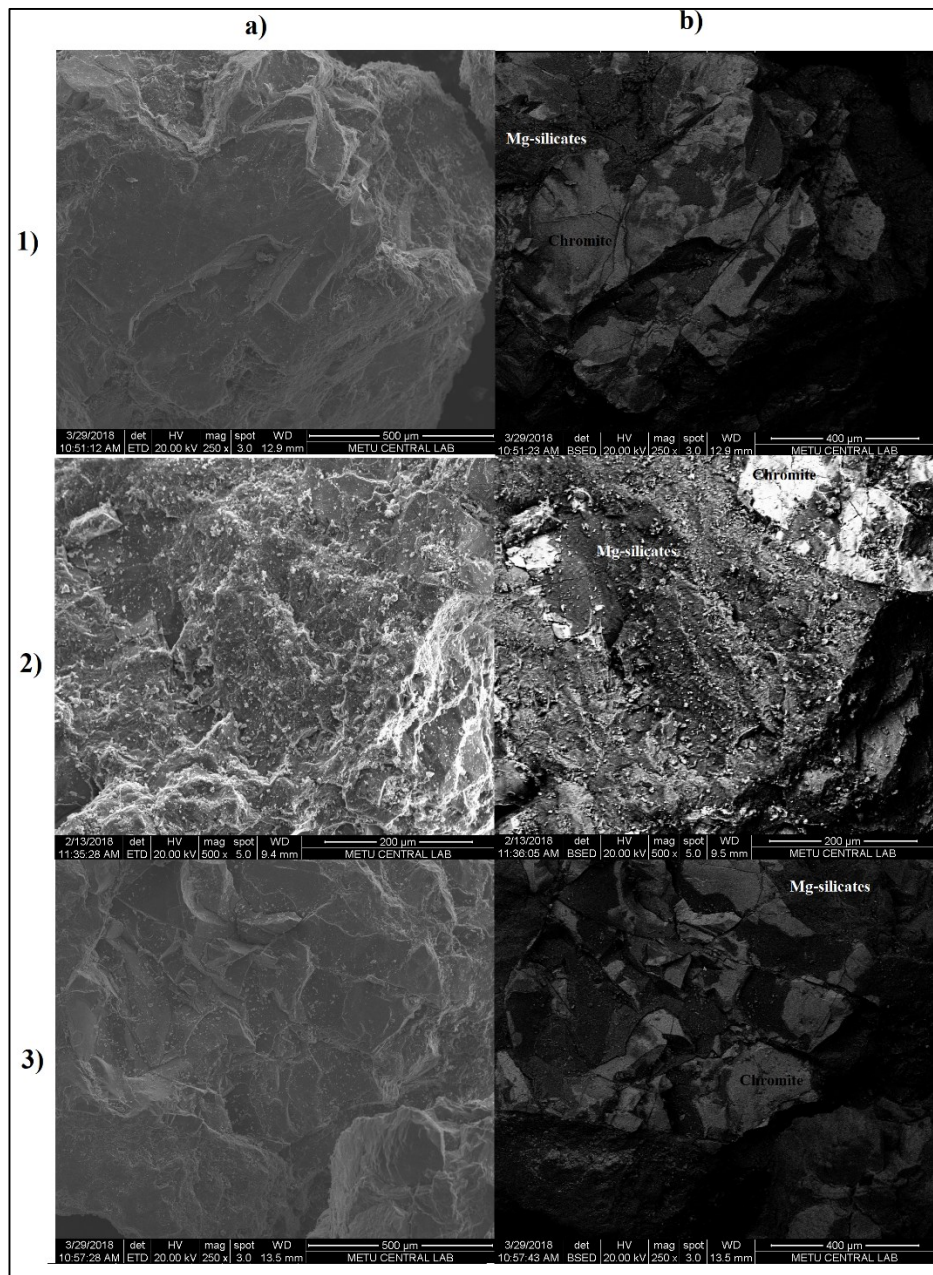
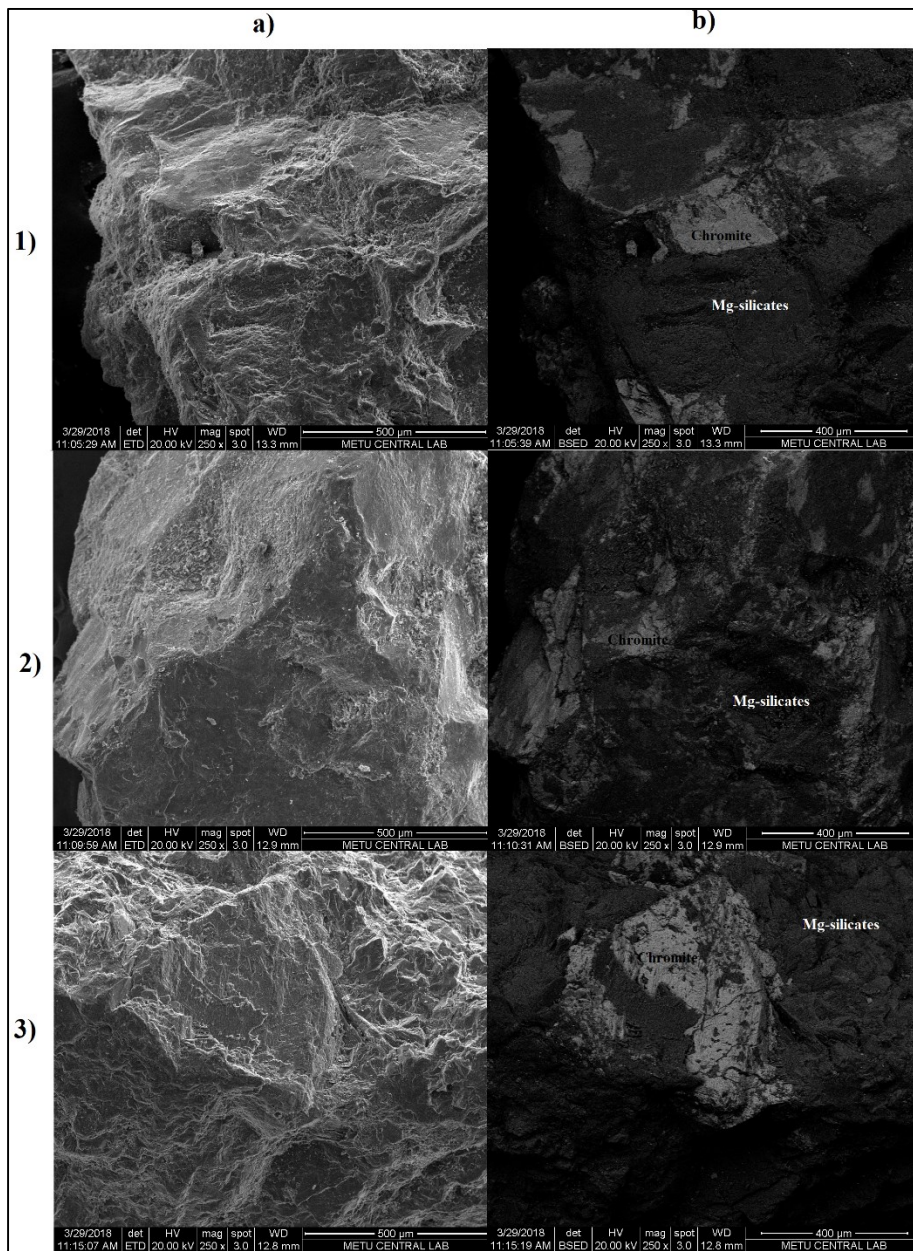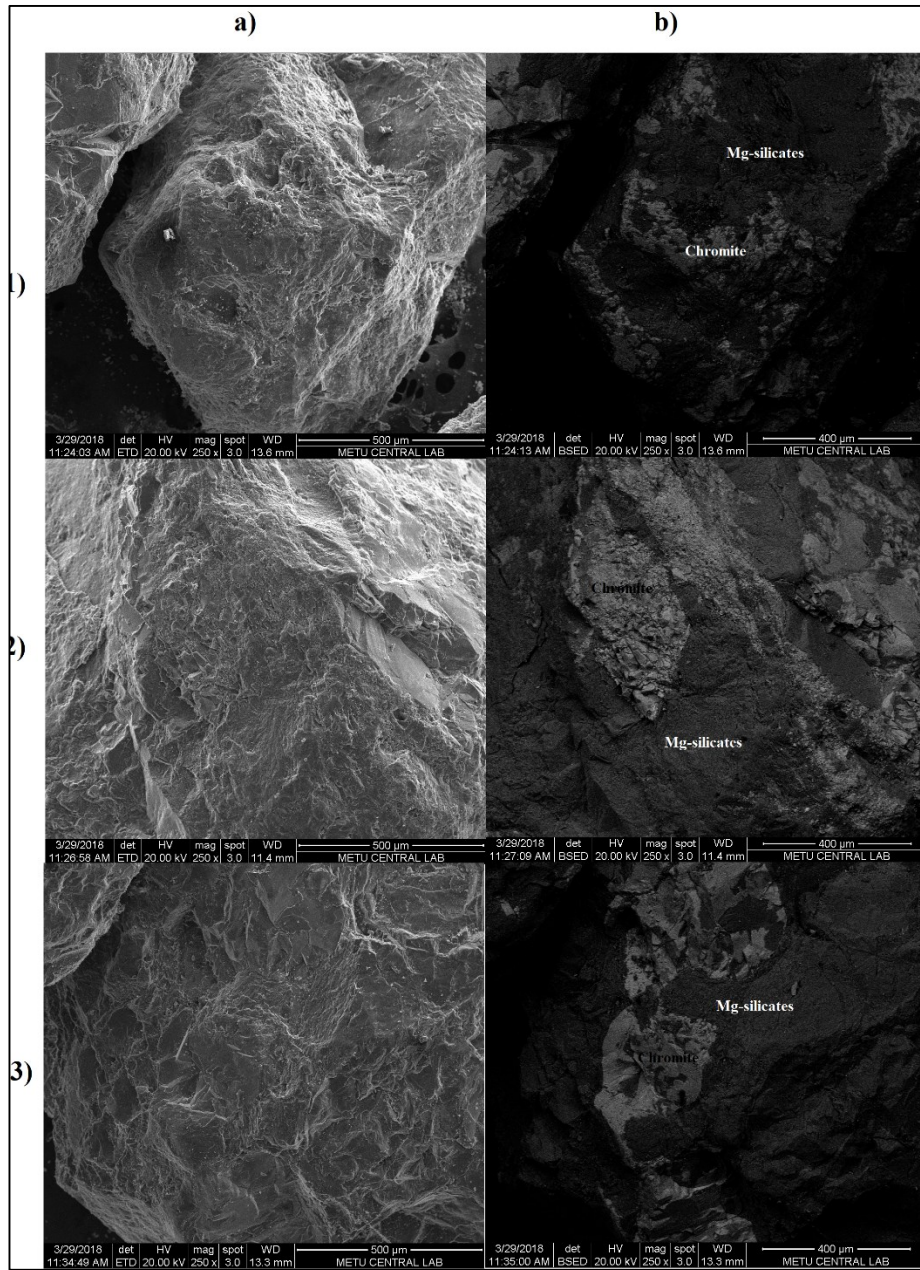Figure E.5 a) Secondary electron and b) corresponding Backscatter electron images
of progeny particles of samples treated in (1) acidic (2) slightly-acidic and (3)
alkaline Amine solutions

VITA

PERSONAL INFORMATION

Surname, Name: Camalan, Mahmut

Nationality: Turkish (TC)

Date and Place of Birth: 11 September 1985, Ankara

Marital Status: Single

Phone: +90 534 964 14 41

email: camalanmahmut@gmail.com

EDUCATION

Degree	Institution	Year of Graduation
MS	METU Mining Engineering	2012
BS	METU Mining Engineering	2009
High School	Kurtuluş High School, Ankara	2003

WORK EXPERIENCE

Year	Place	Enrollment
2009- Present	METU Mining Engineering	Research Assistant

FOREIGN LANGUAGES

Turkish (Native), English (Fluent), French (Proficient), Russian (Proficient), German (Beginner)

PUBLICATIONS

1. Camalan, M., Hoşten, Ç. (2013). An assessment of changes in the breakage parameters of cement clinker in High-Pressure Grinding Rolls. In I. Nishkov, I. Grigorova, D. Mochev (Eds.), Proceedings of XV. Balkan Mineral Processing Congress (p. 146). Sofia: St. Ivan Rilski.

2. Camalan, M., Hoşten, Ç. (2014). Investigating the physical changes of cement clinker particles broken in High-Pressure Grinding Rolls. In Ü. İpekoğlu, V. Arslan, S. Şen (Eds.), Proceedings of the 14th International Mineral Processing Symposium (pp. 51–55). Kuşadası: Turkish Mining Development Foundation.

3. Camalan, M., Hoşten, Ç. (2015). Ball-mill grinding kinetics of cement clinker comminuted in the High-Pressure Roll Mill. Mineral Processing and Extractive Metallurgy Review, 36(5), 310–316.

4. Camalan, M., Önal, M. A. R. (2016). Influence of high-pressure grinding rolls on physical properties and impact breakage behavior of coarsely sized cement clinker. Particulate Science and Technology, 34(3), 278–288.

5. Camalan, M., Hoşten, Ç. (2016). Linking impact-related progeny sizes of cement clinker to modes of single-particle breakage. E3S Web of Conferences, 1010, 1–7.

6. Camalan, M., Hoşten, Ç. (2016). The effect of microwave heating on the breakage behavior of a chromite ore. In M. S. Çelik, G. Bulut, F. Karakaş, O. Güven, H. Baştürkçü, Z. Tarsus (Eds.), Proceedings of the 15th International Mineral Processing Symposium (pp. 247–253). İstanbul.

7. Camalan, M., Çavur, M., Hoşten, Ç. (2017). Assessment of chromite liberation spectrum on microscopic images by means of a supervised image classification. Powder Technology, 322, 214–225.

HOBBIES

Language Learning, World History